Methods[1]

Expedition 322 Scientists[2]

Chapter contents

Introduction

This chapter documents the methods used for shipboard scientific analyses, including sample collection, preparation, and preservation for either shipboard or shore-based analysis. This information can be used to understand the means by which we arrived at preliminary conclusions and interpretations. It also provides information for those interested in ancillary analyses, shore-based sampling, or integrative investigations.

This chapter explains coring techniques, core handling, and the numbering of sites, holes, cores, sections, and samples. In most cases, this information mirrors the details described in previous volumes of the *Proceedings of the Integrated Ocean Drilling Program*. However, because of the relationship between this expedition and the other expeditions that comprise the Nankai Trough Seismogenic Zone Experiment (NanTroSEIZE) and the large number and volume of sample requests, there are significant differences that will be explained below.

Site locations

Integrated Ocean Drilling Program (IODP) Expedition 322 site locations were selected based on precruise surveys and the overall goals of NanTroSEIZE. Onboard Global Positioning System satellite navigation was used to position the vessel using dynamic positioning, and acoustic beacons deployed on the seafloor provided additional means of acquiring and keeping vessel position during operations. Because the remotely operated vehicle was not deployed in the >3000 m water depth, a precise fix on the location of the borehole was not obtained upon spud-in. The ship's position was used as the borehole position.

Drilling operations

Expedition 322 used only one type of coring operation: rotary core barrel (RCB).

Drilled intervals are initially referred to in drilling depth below rig floor (DRF), which is measured from the kelly bushing on the rig floor to the bottom of the drill pipe, and is later converted to core depth below seafloor (CSF). At IODP Hole C0011B, the DRF depth of the seafloor was determined as that of IODP Hole C0011A drilled during IODP Expedition 319. The DRF depth of the seafloor for Hole C0011A was determined from the length of the drill

[1] Expedition 322 Scientists, 2010. Methods. *In* Saito, S., Underwood, M.B., Kubo, Y., and the Expedition 322 Scientists, *Proc. IODP,* 322: Tokyo (Integrated Ocean Drilling Program Management International, Inc.). doi:10.2204/iodp.proc.322.102.2010
[2] **Expedition 322 Scientists' addresses.**

doi:10.2204/iodp.proc.322.102.2010

string, combined with the interpretation of the mudline depth from logging-while-drilling (LWD) gamma ray and resistivity data. The rig floor is 28.3 m above the mean sea level for Holes C0011A and C0011B.

Drilling-induced core deformation

X-ray computed tomography (CT) imagery and direct inspection of split cores often reveal significant evidence for disturbance of recovered materials. For example, during RCB coring deformation results from rotation and "spiraling" of sections of cores, "biscuiting" of small sections of core and injection of either drilling mud or finely ground material produced at the drill bit into spaces between individual biscuits, or brecciation or grinding of material before collection into the core liner/core barrel. Core deformation may also result from depressurization, expansion, and thermal equilibration of the core as it travels up the drill string, during handling on deck, and during core cutting and splitting. Where possible, such core disturbance was noted in core descriptions.

Numbering of sites, holes, cores, sections, and samples

Sites drilled by the D/V *Chikyu* are numbered consecutively from the first site with a prefix "C." A site refers to one or more holes drilled while the ship is positioned within 300 m of the first hole. The first hole drilled at a given site is assigned the site number modified by the suffix "A," the second hole takes the site number and suffix "B," and so forth. These suffixes are assigned regardless of recovery, as long as penetration takes place. During Expedition 322, we drilled at Sites C0011 (proposed Site NT1-7A) and C0012 (proposed Site NT1-01A). During Expedition 322, the *Chikyu* occupied Hole C0011B at Site C0011 and IODP Holes C0012A and C0012B at Site C0012. Hole C0011A was drilled during Expedition 319.

Cored intervals are calculated based on an initial 9.5 m length, which is the standard core barrel length for each coring system. In addition, we specified the collection of shorter coring intervals in areas of poor recovery or slow rate of penetration (ROP). Expansion of cores in the upper sections (and sucked-in material) and gaps related to unrecovered material result in recovery percentages greater or less than 100%, respectively. Depth intervals are assigned starting from the depth below seafloor at which coring started (IODP coring depth scale calculated using Method A [CSF]; see IODP Depth Scales Terminology at **www.iodp.org/program-policies/**). Short cores (incomplete recovery) are all assumed to start from that initial depth by convention. Core expansion is corrected during final processing of core measurements by subtracting void spaces, subtracting exotic material, and accounting for expansion (IODP coring depth scale calculated using Method B [CSF-B]).

A recovered core is typically divided into 1.4 m long sections that are numbered serially from 1 beginning at the top. During Expedition 322, whole-round core samples were removed for time-sensitive interstitial water sampling and assigned their own section number in order to allow for rapid X-ray CT scanning of time-sensitive samples. Material recovered from the core catcher was assigned to a separate section, labeled core catcher (CC), and placed at the bottom of the lowermost section of the recovered core.

A full identification number for a sample consists of the following information: expedition, site, hole, core number, core type, section number, and top to bottom interval in centimeters measured from the top of the section. For example, a sample identification of "322-C0011B-2R-1, 80–85 cm," represents a sample removed from the interval between 80 and 85 cm below the top of Section 1 of the second RCB core from Hole C0011B, during Expedition 322 (Fig. **F1**).

Core handling

The following sections describe in detail the flow of core from the drill floor through the laboratory. See Figure **F2** for a step-by-step flow chart of the entire process.

Core cutting area

As soon as a core is retrieved on deck, the core catcher is delivered to the core cutting area. A sample is taken for paleontological analysis, and the remainder of the core catcher sample is packed into the core liner and curated. The whole core is delivered to the core cutting area and curated for recovery length. Sections for time-sensitive whole-round samples are immediately cut out of the core, curated, and delivered to the X-ray CT laboratory for CT scanning. The time-sensitive whole-round samples include those for interstitial water and/or deep biosphere analysis. Oversight by a structural geologist in the X-ray CT laboratory acting as a "watchdog" (see below) is required before the time-sensitive whole round is processed. If the watchdog finds a potentially high interest feature, Co-Chief Scientists make a decision whether or not the section may be processed. If rejected, the section is brought back to the regular core flow.

Remaining core is cut into sequentially numbered 1.4 m long sections in the core cutting area. If cores contain gas in void spaces, void gas samples are collected at this time. Small (5 cm^3) plugs of sediment are removed from the bottom of appropriate core

sections, typically adjacent to a whole-round sample for interstitial water squeezing, for headspace gas analysis.

The recovered core length and the total length of void space are measured, and core identification, length, drilling advance, and depth information are entered into the J-CORES database. Each section is then sealed at the top (blue cap, blue tape) and bottom (clear cap, white tape); yellow caps indicate removed whole-round core samples (with sample code marked on the end cap). All sections are marked and labeled, data are entered into the J-CORES database, and sections are moved to the core processing deck.

Core processing deck

All sections are scanned using X-ray CT, and each shift has a structural geologist acting as a watchdog to oversee the collection and selection of whole-round core samples, to identify sections or intervals of special interest or unique character, and to prevent destruction of any critical samples.

Following X-ray CT scanning and time-sensitive whole-round core sampling, core sections are allowed to equilibrate to ambient laboratory temperature (2–3 h, ~20°C), after which they are run through the whole-round multisensor core logger (MSCL-W). During Expedition 322, measurements of gamma ray attenuation (GRA) bulk density, *P*-wave velocity, resistivity, magnetic susceptibility, and natural gamma radiation were collected using the MSCL-W. Thermal conductivity measurements were also made on whole-round core sections for soft-sediment cores.

Following MSCL-W and thermal conductivity measurement, if conducted on whole-round cores, a second round of whole-round core sampling for shore-based geotechnical and hydrogeologic analyses is conducted. The number of whole-round samples collected and their locations were based on length of core recovered and extent of intact undeformed pieces from examination of the X-ray CT data.

Following completion of whole-round core sampling, sections are split axially into working and archive halves. The archive half is subjected to nondestructive color spectroscopy, digital photo image scanning, and visual core description (VCD), after which it is covered in plastic film, shrink-wrapped in plastic, and stored in either the cold-store refrigerator or the refrigerated containers at 4°C. The working half is subjected to structural analysis and sampling and measurement for physical properties (e.g., moisture and density [MAD] and velocity) and is then sampled for postcruise analyses. Following completion of sampling, these sections are also wrapped, sealed, and stored at 4°C in preparation for shipping to the core repository. All samples collected are labeled, packaged, stored, and shipped to their final destinations according to standard practice or special instructions.

Community whole-round samples

Through NanTroSEIZE expeditions, we collect substantial numbers of "community" archive samples, especially whole rounds. In some cases, these community samples will augment and/or provide redundancy for those requested by shipboard scientists. The goal is to preserve samples for a wide range of overall science objectives over the duration of the NanTroSEIZE project. This strategy, for example, will enable additional analyses of critical intervals once those zones are identified from initial shore-based laboratory tests.

During Expedition 322, each community whole-round sample was a total of 23 cm long. A community whole round was taken from each core that had sufficient recovery. The sample was cut into two pieces; one is 15 cm long, and the other is 8 cm long. These samples were shipped to Kochi Core Center (KCC) and will be made available to the NanTroSEIZE community. A "cluster" sample was associated with each community whole round.

Sample clusters

To ensure achievement of overall NanTroSEIZE scientific objectives, it is essential to collocate suites of complementary data types for integration and analysis. This must be done with appropriate and consistent sample spacing throughout each hole. During Expedition 322, sample clusters were located immediately adjacent to all whole-round intervals extracted for interstitial water geochemistry and frictional/geotechnical/hydrogeology tests, including community whole rounds. The cluster samples were taken immediately after cutting the whole-round sample. This group of samples consists of material for shipboard X-ray diffraction (XRD), MAD, carbonate analyses, X-ray fluorescence (XRF), and personal samples (e.g., grain size, fabric, and clay mineral XRD).

Routine microbiological sampling

During Expedition 322, routine microbiological sampling was conducted as per Science and Technology Panel (STP) Recommendation 0908-09 (**www.iodp.org/stp/**). Although this has not been officially implemented, Expedition 322 agreed that these samples would be handled as test implementation of routine microbiological sampling. Whole-round samples were taken when recovery was good from an interval adjacent to a whole-round sample for interstitial

water and was immediately frozen at –80°C (see "Microbiology").

Authorship of chapters

The separate sections of the site chapters and methods chapter were written by the following shipboard scientists (authors are listed in alphabetical order; no seniority is implied):

Introduction: Shipboard Science Party
X-ray computed tomography: Kitamura, Yamamoto
Lithology: Kutterolf, Labanieh, Naruse, Pickering, Scudder, Wu
Structural geology: Kitamura, Yamamoto
Biostratigraphy: Chiyonobu, Govil
Paleomagnetism: Oda, Zhao
Physical properties: Dugan, Hamada, Hüpers, Ikari, Spinelli
Inorganic geochemistry: Destrigneville, Moreau, Torres
Organic geochemistry: Heuer
Microbiology: Moreau
Downhole measurements: Dugan, Sanada
Logging and core-log-seismic integration: Park, Sanada, Slagle, Tudge

X-ray computed tomography

X-ray CT imaging provided information about structures and sedimentological features in the core and helped to assess sample locations and quality for whole-round samples. Our methods followed those in the measurement manual prepared by the Center for Deep Earth Exploration (CDEX) (X-ray CT Scanning, version 1.00, 26 Dec 2008) and used on previous expeditions (e.g., IODP Expeditions 315 and 316). The manual is based on GE Healthcare (2006), Mees et al. (2003), and Nakano et al. (2000).

The X-ray CT scanner on the *Chikyu* is a GE Yokogawa Medical Systems LightSpeed Ultra 16 capable of generating sixteen 0.625 mm thick slice images every 0.5 s, the time for one revolution of the X-ray source around the sample. Data generated for each core consist of core-axis-normal planes of X-ray attenuation values with dimensions of 512 × 512 pixels. Data were stored as Digital Imaging and Communication in Medicine (DICOM) formatted files.

Background

The theory behind X-ray CT has been well established through medical research and is very briefly outlined here. X-ray intensity varies as a function of X-ray path length and the linear attenuation coefficient (LAC) of the target material as

$$I = I_0 \times e^{-\mu L}, \quad (1)$$

where

I = transmitted X-ray intensity,
I_0 = initial X-ray intensity,
μ = LAC of the target material, and
L = X-ray path length through the material.

LAC is a function of the chemical composition and density of the target material. The basic measure of attenuation, or radiodensity, is the CT number given in Hounsfield units (HU) and is defined as

$$\text{CT number} = [(\mu_t - \mu_w)/\mu_w] \times 1000, \quad (2)$$

where

μ_t = LAC for the target material, and
μ_w = LAC for water.

The distribution of attenuation values mapped to an individual slice comprises the raw data that are used for subsequent image processing. Successive two-dimensional (2-D) slices yield a representation of attenuation values in three-dimensional (3-D) voxels.

Analytical standards used during Expedition 322 were air (CT number = –1000), water (CT number = 0), and aluminum (2477 < CT number < 2487) in an acrylic core mock-up. All three standards were run once daily after air calibration. For each standard analysis, the CT number was determined for a 24.85 mm^2 area at fixed coordinates near the center of the cylinder.

X-ray CT scan data usage

X-ray CT scans were used during Expedition 322 to

- Examine 3-D features of deformation structures, bioturbation, and so on;
- Distinguish "natural" fracture/faults and drilling-induced fractures;
- Measure dip angles of faults, bedding, veins, and so on;
- Provide an assessment of core and core liner integrity;
- Determine locations for whole-round samples; and
- Identify important structural and sedimentological features to be avoided by whole-round sampling.

X-ray CT scanning was done immediately after core cutting for time-sensitive (interstitial water, microbiology, organic geochemistry, and anelastic strain recovery) whole-round samples to finalize their selection (Table T1). All whole-round core sections were screened to avoid destructive testing on intervals that may contain interesting structural or sedimentological features. This also facilitated identifying intervals with minimal drilling disturbance

for whole-round sampling and for assessing heterogeneity (essential for postexpedition studies of frictional, geotechnical, and hydrogeological properties).

Lithology

Visual core descriptions

We followed conventional Ocean Drilling Program (ODP) and IODP procedures for recording sedimentologic information on VCD forms on a section-by-section basis (Mazzullo and Graham, 1988). Core descriptions were transferred to section-scale templates using J-CORES software and then converted to core-scale depictions using Strater software. Texture (defined by the relative proportions of sand, silt, and clay) follows the classification of Shepard (1954). The classification scheme for siliciclastic lithologies follows Mazzullo et al. (1988).

The Graphic Lithology column on each VCD plots to scale all beds that are at least 2 cm thick. Graphic patterns do not show persistent interlayers <2 cm thick, but such intervals are identified as laminae in the Sedimentary Structures column. It is difficult to discriminate between the dominant lithologies of silty claystone and clayey siltstone without quantitative grain size analysis. However, we tried to make a qualitative visual distinction between silty claystone and clayey siltstone on the basis that clay contains <25% silt (Shepard, 1954). We did not use separate patterns for more heavily indurated examples of the same lithologies (e.g., silty clay versus silty claystone) because the dividing line is arbitrary. In practice, we used terms for lithified rock because we only obtained RCB cores. Figure **F3** displays graphic patterns for all sedimentary lithologies encountered during Expedition 322. Also shown are symbols for internal sedimentary structures, soft-sediment deformation structures, and severity of core disturbance in sedimentary rock.

Where calcareous sediments occur, we used the term "calcareous claystone" for clay-rich deposits that contain 10%–50% calcite (following the classification Mizutani et al., 1987) and "lime mudstone" where there is a mud-supported fabric with >90% carbonate component (Dunham, 1962; expanded by Embry and Klovan, 1972).

To emphasize the differences in the composition of volcanic sandstones, we modified the classification scheme of Fisher and Schmincke (1984). In general, coarser grained sedimentary rocks (63 µm to 2 mm average grain size) are named "sandstone" where volcaniclastic components are <25% of the total clasts. Volaniclastic grains can be (1) reworked and commonly altered heterogeneous fragments of preexisting volcanic rock, tuff, or tephra or (2) fresh, or less altered, compositionally homogeneous pyroclasts. Pyroclasts are produced by many types of processes associated with volcanic eruptions, without reference to the causes of the eruption or origin of the particles. Pyroclasts can includes crystals, glass shards, and rock fragments.

If the sedimentary rock contains >25% but <75% volcaniclasts, it is designated a "volcaniclastic sandstone." As a subset if volcaniclastic sandstone, if >25% but <75% of the volcaniclasts are vitric pyroclasts, then we used the term "tuffaceous sandstone." If the total clast composition is >75% pyroclasts, then the sediment is classified as "ash" or, if lithified, as "tuff." Depending on the grain size and degree of compaction, the nomenclature is adjusted accordingly (e.g., tuff versus ash), as shown in Table **T2.** Because of problems with accuracy, compositions close to the dividing lines of the classification scheme are problematic. In addition, with the exception of fresh glass shards in the population of pyroclasts, it is difficult to use smear slides to discriminate unequivocally between primary eruptive products and crystals or rock fragments created by erosion of fresh volcanic materials.

Bioturbation intensity in deposits was estimated using the semiquantitative ichnofabric index as described by Droser and Bottjer (1986, 1991). The indexes refer to the degree of biogenic disruption of primary fabric such as lamination and range from 1 for nonbioturbated sediment to 6 for total homogenization:

1 = No bioturbation recorded; all original sedimentary structures preserved.
2 = Discrete, isolated trace fossils; <10% of original bedding disturbed.
3 = Approximately 10%–40% of original bedding disturbed. Burrows are generally isolated but locally overlap.
4 = Last vestiges of bedding discernable, ~40%–60% disturbed. Burrows overlap and are not always well defined.
5 = Bedding is completely disturbed, but burrows are still discrete in places and the fabric is not mixed.
6 = Bedding is nearly or totally homogenized.

The ichnofabric index in cores was identified with the help of visual comparative charts (Heard and Pickering, 2008). Distinct burrows that could be identified as particular ichnotaxa were also recorded.

Smear slides and thin sections

Smear slides and thin sections are useful for identifying and reporting basic sediment attributes (texture

and composition), but the results are only semiquantitative. We estimated the texture of the sediments with the help of a visual comparison chart (Rothwell, 1989). Errors can be large, however, especially for textural estimates of the fine silt and clay-size fractions. Smear slide analysis also tends to underestimate the amount of sand-size grains because they are difficult to incorporate evenly onto the slide. As during Expedition 315, we suspect that the counting errors can be considerable (e.g., "Lithology" in Expedition 315 Scientists, 2009) and easily up to ~20%. Nevertheless, in order to define lithologies, smear slides are one way to compare textures and composition by point counting.

Point counting on smear slides was made over at least four defined areas using 100× to 200× magnification. This method works well for sandstones and sandy siltstones in thin sections, and the theoretical 2σ error for a total of 200 counted particles in a thin section is between 3% and 7%, depending on the portion of the total inventory (van der Plas and Tobi, 1965). As mentioned above, errors are larger using smear slides because of uneven grain distributions, which makes reliable classification of some volcanic-rich sandstones difficult. This is particularly true if compositions are close to a boundary of the classification scheme. The various components were binned into several categories (e.g., feldspar, pyroxene, metamorphic lithics, sedimentary lithics, etc.) to facilitate the optimum reproducibility among different scientists (Table **T3**).

For fine-grained sediments (silt/siltstone and silty clay/claystone), rough estimations were made regarding the matrix, using the visual comparison chart after Rothwell (1989). Point counting of the coarser fraction was then added, and together they were normalized to 100% of the total component inventory. Because most of the point counting is based on estimations, 2σ error for the finer grained sediments is much higher and must be considered when interpreting the results. To reduce errors, we normalized the data for the finer grained sediments against three principal classes: for example, quartz or feldspar, as well as volcanic clastic or sedimentary lithic content were normalized to total mineral and total lithic contents, respectively. Additionally, the inventory of ash layers, ash pods, and dispersed ash layers was documented separately to account for the presence of glass shard textures, juvenile components, and other minerals. This method was not applied to lithified tuffs because of the crushing of many glass shards during slide preparation. Detailed results are given in the Tephra logs (see TEPHRA in **"Supplementary material"**) and summarized in the smear slides (see **"Core descriptions"**). The relative major component abundance was also validated by bulk powder XRD (see **"X-ray diffraction"**), and the absolute weight percent of carbonate was verified by chemical analysis (see **"Organic geochemistry"**).

The sample location for each smear slide was entered into J-CORES with a sample code of "SS," using the Samples application. The position of each specimen is shown on the VCD slide editor column of the VCD application.

X-ray diffraction

We completed routine XRD analyses of bulk powders using a PANalytical CubiX PRO (PW3800) diffractometer. Our principal goal was to estimate relative weight percentages of total clay minerals, quartz, plagioclase, and calcite using diagnostic peak areas. Most of the samples were selected from intervals adjacent to whole-round samples, and most are part of sampling clusters that included samples for physical properties, carbonate, and XRF. A few additional samples were collected periodically from unusual lithologies such as carbonate-cemented claystone and volcanic ash. Samples were freeze-dried, crushed with a ball mill (along with powder for XRF and carbonate), and mounted as random bulk powders. The instrument settings were as follows:

Generator = 45 kV and 40 mA.
Tube anode = Cu.
Wavelength = 1.54060 Å ($K_{\alpha1}$) and 1.54443 Å ($K_{\alpha2}$).
Step spacing = 0.005°2θ.
Scan step time = 0.648 s.
Divergent slit = automatic.
Irradiated length = 10 mm.
Scanning range = 2°–60°2θ.
Spinning = yes.

In order for our results to match those of ODP Leg 190 and NanTroSEIZE Stage 1 as closely as possible, the choice was made to use MacDiff 4.2.5 software (**www.ccp14.ac.uk/ccp/ccp14/ftp-mirror/krumm/Software/macintosh/macdiff/MacDiff.html**) for data processing. Each peak's upper and lower limits were adjusted manually following the guidelines shown in Table **T4.** Calculations of relative mineral abundance utilized a matrix of normalization factors derived from integrated peak areas and singular value decomposition (SVD) (Table **T5**). As described by Fisher and Underwood (1995), calibration of SVD factors depends on the analysis of known weight-percent mixtures of mineral standards that are appropriate matches for natural sediments. SVD normalization factors were recalculated during Expedition 315 after the diffractometer's high-voltage power supply was replaced. Bulk powder mixtures for the Nankai Trough are the same as those reported by Underwood et al. (2003): quartz (Saint Peter sand-

stone), feldspar (Ca-rich albite), calcite (Cyprus chalk), smectite (Ca-montmorillonite), illite (Clay Mineral Society IMt-2, 2M1 polytype), and chlorite (Clay Mineral Society CCa-2). Examples of diffractograms for standard mixtures are shown in Figure F4.

In order to calculate average errors (SVD-derived estimates versus true weight percent), immediately prior to Expedition 322, 14 standard mineral mixtures were run three times each. The average precision (reproducibility) is total clay minerals = 1.7%, quartz = 1.1%, plagioclase = 1.3%, and calcite = 1.0%. The average accuracy (true% – calculated%) is total clay minerals = 4.0%, quartz = 2.0%, plagioclase = 1.8%, and calcite = 1.9%. In spite of its precision with standard mixtures, the SVD method is only semiquantitative, and results for natural specimens should be interpreted with some caution. One of the fundamental problems with any bulk powder XRD method is the difference in peak response between poorly crystalline minerals at low diffraction angles (e.g., clay minerals) and highly crystalline minerals at higher diffraction angles (e.g., quartz and plagioclase). Contents of clay minerals are best characterized by measuring the peak area, whereas peak intensity may be easier and more accurate to quantify quartz, feldspar, and calcite. Analyzing oriented aggregates rather than random orientations enhances basal reflections of the clay minerals, but this step is time consuming and requires isolation of the clay-size fraction to be effective. Errors also propagate as more minerals and peaks are added to the procedure. Counts for "plagioclase" may also include K-feldspar, so we refer to that value in natural specimens as "feldspar." For clay mineral assemblages, the two options are to individually measure one peak for each mineral and add the estimates together (thereby propagating the error) or to measure a single composite peak at 19.4°–20.4°2θ. Chlorite does not contribute to this composite peak. Another source of error is contamination of mineral standards by impurities such as quartz (e.g., the illite standard contains ~20% quartz). For trace quantities of a mineral and peaks with low intensity, use of negative SVD normalization factors may result in negative values of absolute weight percent. In such cases, we inserted the numerical value of 0.1% as a proxy for "trace."

In the final assessment, calculated values of a mineral's weight percent should only be regarded as relative percentages within a four-component system where clay minerals + quartz + feldspar + calcite = 100%. How close those estimates are to their absolute percentages within the mass of total solids will depend on the abundance of amorphous solids (e.g., biogenic opal and volcanic glass), as well as the total of all other minerals that occur in minor or trace quantities. For most natural samples, the absolute errors are probably between 5% and 10%. Thus, the primary value of bulk powder XRD data should be to identify spatial and temporal trends in sediment composition and to assist with core-log integration.

X-ray fluorescence

Whole-rock quantitative XRF spectrometry analysis was undertaken on core samples for the major elements. Samples of 10 cm^3 were taken from every interstitial water cluster sample. Additional samples were collected from the working half of the core next to samples for XRD and carbonate analysis. Samples were freeze-dried, crushed with a tungsten-ball mill, and fused with 4.5 g of SmeltA12 flux for 7 min at 1150°C to create glass beads. Loss on ignition was measured using weight changes on heating at 1000°C for 3 h. Analyses were performed on the wavelength dispersive XRF spectrometer Supermini (Rigaku) equipped with a 200 W Pd anode X-ray tube at 50 kV and 4 mA.

Major elements were measured using the fused glass bead method and are presented as weight percent oxide proportions (Na_2O, MgO, Al_2O_3, SiO_2, P_2O_5, K_2O, CaO, TiO_2, MnO, and Fe_2O_3) (Table T6). Rock standards of the National Institute of Advanced Industrial Science and Technology (Geological Survey of Japan [GSJ]) were used as the reference materials for quantitative analysis. Table T7 lists the results and standard deviations for standard samples. Processed data were uploaded into J-CORES as a comma-delimited data file. Data are reported as total counts on the peak and also as semiquantitative oxide weight percents.

X-ray fluorescence scanning

We undertook whole-rock semiquantitative XRF spectrometry analysis for major elements and trace elements on core material (Na, Mg, Al, Si, P, S, K, Ca, Ti, V, Cr, Mn, Fe, Cu, Ni, Zn, and Zr). Semiquantitative element scanning of core sections was undertaken using the onboard JEOL TATSCAN-F2 energy dispersive spectrometry (EDS)-based split-core scanner, equipped with a cryogenic Si semiconductor and a 76 mm berylium window (Sakamoto et al., 2006). The target for the X-ray generation is rhodium (Rh) that can generate X-rays with five times higher intensity compared to the standard EDS-based scanner. The diameter of the collimeter that detects the incident X-ray beam is 0.8 mm, and the space for irradiation on the sample is ~1.1 mm. Although the distance between the sample surface and detector critically affects the intensity of X-rays, the

TATSCAN-F2 has a function that moves the X-ray unit automatically to maintain a 1 mm distance between the core surface and measurement window, thereby reducing the problem. Data are reported as total counts on the peak. Semiquantitative oxide weight percents for some elements were calculated from background-corrected integrated peak intensities using software provided by the vendor (JEOL) for the TATSCAN. Further theoretical details and operational procedures are outlined in Richter et al. (2006).

Prior to scanning, the core surface was carefully cleaned with a brush between each scanned section. The core sections were scanned with 3.0 mm spacing at 30 kV (1000 µA), with a 150 s sampling time. After measurement, the XRF spectral data were saved and converted into a CSV file using the ElementStation2 software. The results were uploaded to J-CORES and displayed at the corresponding depth on the Composite Log Viewer program. All raw data were also saved to the onboard share server.

Basement description

The methods used for volcanic basement description were based on VCD and thin section analyses. Lava morphology was identified by visual description of the core, initially from whole-round core sections. Visual description (using a binocular microscope) also helped distinguish between the different types of volcanic/igneous rock. Thin sections were produced for each volcanic/igneous rock unit. Rock texture, grain size, and phenocryst mineralogy together with abundance were determined using thin section analysis. Massive lava units were divided into individual cooling units based on the presence of chilled margins.

All basement core descriptions and associated shipboard analyses were archived electronically in J-CORES. Figure F5 displays graphic patterns for all basement lithologies encountered during Expedition 322. When describing and assigning a name to a rock interval, cores were divided based on changes in mineralogy, texture, grain size, composition, and the occurrence of chilled margins. For igneous petrology, all rocks were assigned to porphyritic, aphanitic, or phaneritic groups. Aphanitic rocks were divided into glassy, aphyric, and phyric groups based on their phenocryst abundance, whereas phaneritic rocks were defined as fine, medium, and coarse grained (Table T8). At the microscopic scale, rock texture was defined according to the degree of crystallinity (Table T8), with all other textural terms used being based on the definitions in McKenzie et al. (1982). Textural features within glass-rich zones were described using definitions in ODP Leg 147 *Initial Reports* volume (Shipboard Scientific Party, 1993). All classification and textural data were recorded in J-CORES.

Structural geology

Our methods for documenting the structural geology of Expedition 322 cores largely followed those given by the Expeditions 315, 316, and 319 structural geologists (see "Structural geology" in Expedition 315 Scientists [2009], Expedition 316 Scientists [2009], and Expedition 319 Scientists [2010]). We documented the deformation observed in the split cores by classifying structures, determining the depth extent, measuring orientation data, and recording kinematic information. The data were hand-logged onto a printed form at the core table and then typed into both a spreadsheet and J-CORES. Where possible, the orientation data were also corrected for rotation related to drilling on the basis of paleomagnetic declination and inclination information.

Core description and orientation data collection

Each structure was recorded manually on a structural description sheet modified from that used during Expedition 316 (Fig. F6). We found that this modified sheet is particularly useful to record orientation data for linear structures (e.g., striation on the fault plane). Core measurements followed Expeditions 315 and 316, which in turn were based on previous ODP procedures developed at the Nankai accretionary margin (i.e., ODP Legs 131 and 190). We used a plastic protractor for orientation measurements (Fig. F7). During Expedition 322, we downloaded the X-ray CT images of unsplit cores to identify structures and recognize 3-D geometry and distribution of structures. Using the working half of the split core provided greater flexibility in removing (and cutting, if necessary) pieces of the core for more careful observation and measurement.

Orientations of planar and linear features in cored sediments were determined in the framework of the core coordinate system, which consists of *x*-axis to the "double line" marked on the working half, *z*-axis parallel to the core longitudinal axis to the bottom, and accordingly determined *y*-axis with the right-handed system (Fig. F8). To determine the orientation of a plane, two apparent dips of the planar feature were measured in the core coordinate system and converted to a plane represented by either a strike and dip or a dip and dip direction. This conversion was accomplished using a spreadsheet (Fig. F9). This approach had the advantage of increasing the data processing efficiency and reducing errors in transferring

and retyping data (e.g., by using both R. Allmendinger's Stereonet program [www.geo.cornell.edu/geology/faculty/RWA/programs.html] and a spreadsheet). One apparent dip was typically represented by the intersection of the planar feature with the split face of the core and was quantified by measuring the dip direction and angle in the core coordinate system. Typical apparent dip measurements had a trend of 090° or 270° and ranged in plunge from 0° to 90°. The second apparent dip was usually represented by the intersection of the planar feature and a cut or fractured surface at a high angle to the split face of the core axis. In many cases, this was a surface either parallel or perpendicular to the core axis. In the former cases, the apparent dip lineation would trend 000° or 180° and plunge from 0° to 90°; in the latter cases, the trend would range from 000° to 360° and plunge 0°. Linear features observed in the cores were always associated with planar structures (typically faults or shear zones), and their orientations were determined by measuring either the trend and plunge in the core coordinate system or the rake (or pitch) on the associated plane. All data were recorded on the log sheet with appropriate depths and descriptive information.

Paleomagnetic data were used during NanTroSEIZE to correct drilling-induced rotation of cored sediments. Rotation was induced during RCB coring at Holes C0011B and C0012A, as is common in ocean drilling. However, the long-core cyrogenic magnetometer on the *Chikyu* was malfunctioning because of liquid helium leaking and was out of use during the entire Expedition 322. The paleomagnetic data on board were therefore limited (mostly two discrete shipboard samples per section), and most magnetic corrections could not be performed.

Orientation data analysis based on the spreadsheet

During Expedition 322, we adopted the Expedition 315/316 spreadsheet template for orientation data calculation in the core coordinate system, as well as in the geographic coordinate system from those data measured on cores (e.g., Fig. F9). A minor error in the spreadsheet was corrected by an Expedition 315 scientist just before Expedition 322 started, and we made small modifications such as adding a "depth (mbsf)" column and changing the order of columns for better handling.

Calculation of plane orientation

For planar structures (e.g., bedding or faults), two apparent dips on two different surfaces (e.g., one being the split core surface and the other being the horizontal surface) were measured in the core coordinate system as azimuths (measured clockwise around the *z*-axis from the *x*-axis, looking down) and plunges (Fig. F10). If the azimuths and plunges of the two apparent dips are given as (α_1, β_1) and (α_2, β_2), respectively, as in Figure F10, then the unit vectors representing these two lines, v_1 and v_2, are

$$v_1 = \begin{pmatrix} l_1 \\ m_1 \\ n_1 \end{pmatrix} = \begin{pmatrix} \cos\alpha_1 \cos\beta_1 \\ \sin\alpha_1 \cos\beta_1 \\ \sin\beta_1 \end{pmatrix} \quad (3)$$

and

$$v_2 = \begin{pmatrix} l_2 \\ m_2 \\ n_2 \end{pmatrix} = \begin{pmatrix} \cos\alpha_2 \cos\beta_2 \\ \sin\alpha_2 \cos\beta_2 \\ \sin\beta_2 \end{pmatrix}, \quad (4)$$

where *l*, *m*, and *n* represent the *x*-, *y*-, and *z*-components of the vectors.

The unit vector normal to this plane (v_n) (Fig. F10) is then defined as follows:

$$v_n = \begin{pmatrix} l_n \\ m_n \\ n_n \end{pmatrix} = \frac{v_1 \times v_2}{|v_1 \times v_2|}, \quad (5)$$

where

$$v_1 \times v_2 = \begin{pmatrix} \begin{vmatrix} m_1 & m_2 \\ n_1 & n_2 \end{vmatrix} \\ \begin{vmatrix} n_1 & n_2 \\ l_1 & l_2 \end{vmatrix} \\ \begin{vmatrix} l_1 & l_2 \\ m_1 & m_2 \end{vmatrix} \end{pmatrix} = \begin{pmatrix} m_1 n_2 - m_2 n_1 \\ n_1 l_2 - n_2 l_1 \\ l_1 m_2 - l_2 m_1 \end{pmatrix}. \quad (6)$$

The azimuth (α_n) and plunge (β_n) of v_n are given by

$$\alpha_n = \tan^{-1}\left(\frac{m_n}{l_n}\right), \beta_n = \sin^{-1} n_n. \quad (7)$$

The dip direction (α_d) and dip angle (β) of this plane are α_n and 90° + β_n, respectively, when β_n is <0° (Fig. F11A). They are α_n ± 180° and 90° – β_n, respectively, when β_n is ≥0° (Fig. F11B). The right-hand rule strike of this plane (α_s) is then given by α_d – 90° (Fig. F11).

Calculation of slickenline rake

For a fault with slickenlines, the apparent rake angle of the slickenline (ϕ_a) was measured on the fault surface from either the 090° or 270° direction of the split-core surface trace (Fig. F12). Fault orientation was measured as described above. Provided that v_n and v_c are unit vectors normal to the fault and split

core surfaces, respectively, the unit vector of this intersection line (v_i) is perpendicular to both v_n and v_c (Fig. F12) and is therefore defined as follows:

$$v_i = \begin{pmatrix} l_i \\ m_i \\ n_i \end{pmatrix} = \frac{v_n \times v_c}{|v_n \times v_c|}, \quad (8)$$

where

$$v_c = \begin{pmatrix} 1 \\ 0 \\ 0 \end{pmatrix}, \quad (9)$$

and

$$v_n \times v_c = \begin{pmatrix} \begin{vmatrix} m_n & 0 \\ n_n & 0 \end{vmatrix} \\ \begin{vmatrix} n_n & 0 \\ l_n & 1 \end{vmatrix} \\ \begin{vmatrix} l_n & 1 \\ m_n & 0 \end{vmatrix} \end{pmatrix} = \begin{pmatrix} 0 \\ n_n \\ -m_n \end{pmatrix}. \quad (10)$$

Knowing the right-hand rule strike of the fault plane (α_s), the unit vector (v_s) toward this direction is then

$$v_s = \begin{pmatrix} \cos\alpha_s \\ \sin\alpha_s \\ 0 \end{pmatrix}. \quad (11)$$

The rake angle of the intersection line (ϕ_i) measured from the strike direction is given by

$$\phi_i = \cos^{-1}(v_x \times v_i) \quad (12)$$

because

$$v_s \times v_i = |v_s||v_i|\cos\phi_i = \cos\phi_i, \ \therefore |v_s| = |v_i| = 1. \quad (13)$$

The rake angle of the slickenline (ϕ) from the strike direction is $\phi_i \pm \phi_a$, depending on which direction the apparent rake was measured from and which direction the fault plane dips toward. ϕ_a should be subtracted from ϕ_i when the fault plane dips toward the west and ϕ_a was measured from either the top or 090° direction (Fig. F13A) or when the fault plane dips toward the east and ϕ_a was measured from either the bottom or 090° direction (Fig. F13B). However, ϕ_a should be added to ϕ_i when the fault plane dips toward the east and ϕ_a was measured from either the top or 270° direction (Fig. F13C) or when the fault plane dips toward the west and ϕ_a was measured from either the bottom or 270° direction (Fig. F13D).

Azimuth correction using paleomagnetic data

Provided that a core is vertical, its magnetization is primary, and its bedding is horizontal, its paleomagnetic declination (α_p) indicates magnetic north where the inclination (β_p) is ≥0° (Fig. F14A), whereas it indicates magnetic south where β_p is <0° (Fig. F14B). The dip direction and strike of a plane in the geographic coordinate system (α_d* and α_s*) are therefore

$$\alpha_d^* = \alpha_d - \alpha_p, \quad (14)$$

and

$$\alpha_s^* = \alpha_s - \alpha_p, \quad (15)$$

where

$$\beta_p \geq 0° \quad (16)$$

and are

$$\alpha_d^* = 180° + \alpha_d - \alpha_p, \quad (17)$$

and

$$\alpha_s^* = 180° + \alpha_s - \alpha_p, \quad (18)$$

where

$$\beta_p < 0°. \quad (19)$$

J-CORES structural database

J-CORES database has a VCD program to store a visual (macroscopic and/or microscopic) description of core structures at a given section index and a record of planar structures in the core coordinate system. The orientations of such features are saved as commentary notes but do not appear on the plots of Composite Log Viewer. During Expedition 322, only the locations of structural features are entered in J-CORES by sedimentologists, and orientation data management and planar fabric analysis are done with an Excel spreadsheet as mentioned above.

Description and classification of structures

In general, we described and classified the structures observed using the terminology of J-CORES and Expedition 315/316, which in turn is based on the J-DESC VCD scheme and ODP Legs 131 (Taira, Hill, Firth, et al., 1991), 156 (Shipley, Ogawa, Blum, et al., 1995), 170 (Kimura, Silver, Blum, et al., 1997), and 190 (Moore, Taira, Klaus, et al., 2001). For clarity, however, we define the terminology used to describe fault-related rocks, as well as the basis for differenti-

ating natural and drilling-induced features. The key to the symbols used in J-CORES is given in Figure F3.

It may be difficult to distinguish natural faults from drilling-induced faults. Helicoidal striated surfaces or polished surfaces showing striations that diverge outward most likely indicate drilling-induced fracturing resulting from the torque exerted by the bit on sediments. In contrast, faults that display more planar geometries, parallel lineations, and orientations compatible with preferred orientations displayed by multiple faults nearby are likely natural features. Lastly, when multiple orientation measurements are plotted in stereographic projection, natural minor faults are expected to display preferred orientations that may define coherent strain axes, whereas drilling-induced faults are expected to yield random orientation distribution.

Biostratigraphy

Preliminary ages were assigned to sedimentary strata primarily based on core catcher samples. Samples from within the cores were examined when a more refined age determination was necessary. Ages for calcareous nannofossil and foraminiferal events from the early Miocene through the Quaternary were estimated by correlation to the geomagnetic polarity timescale (GPTS) of Lourens et al. (2004). The biostratigraphic events, zones, and subzones for nannofossils and planktonic foraminifers are summarized in Figure F15. The Pliocene/Pleistocene boundary has been formally located just above the top of the Olduvai (C2n) magnetic polarity subchronozone (Aguirre and Pasini, 1985) and just below the lowest occurrence of medium *Gephyrocapsa caribbeanica* (≥3.5 but <5.5 µm) (Takayama and Sato, 1993–1995; Raffi et al., 2006). We used the lowest occurrence of medium *G. caribbeanica* (≥3.5 but <5.5 µm) to mark the Pliocene/Pleistocene boundary. The Miocene/Pliocene boundary has not been formally defined yet. We tentatively used the last occurrence (LO) horizon of *Discoaster quinqueramus* for the boundary. The first occurrence (FO) of *Globorotalia tumida* (planktonic foraminifer) also marks the approximate position of the stage boundary. Details of the shipboard methods are described below for each microfossil group.

Calcareous nannofossils

The calcareous nannofossil zonal scheme established by Martini (1971) and Okada and Bukry (1980) and modified by Young (1998) was used for lower Miocene–Quaternary sequences during Expedition 322. The calcareous nannofossil biostratigraphic classification of sedimentary sequences follows the recent review by Raffi et al. (2006). In addition, the upper Pliocene–Quaternary biohorizons originally defined by Sato and Takayama (1992) and modified by Raffi et al. (2006) were used for more detailed correlations. Astronomically tuned age estimates for the lower Miocene–Quaternary rely on the geological timescale developed by the International Commission on Stratigraphy (ICS) in 2004 (Lourens et al., 2004). A size-defined species of the genera *Reticulofenestra* was placed into size categories as proposed by Young (1998). For the gephyrocapsids, we adopted the concept of Raffi et al. (2006), and morphological terminology used here is summarized in Perch-Nielsen (1985) and Takayama and Sato (1987). Accordingly, *Gephyrocapsa* is divided into four major groups by maximum coccolith length: small *Gephyrocapsa* (<3.5 µm), medium *Gephyrocapsa* (*G. caribbeanica* and *Gephyrocapsa oceanica*; ≥3.5 but <5.5 µm), *Gephyrocapsa* sp. 3 (*Gephyrocapsa parallela*; ≥4 but <5.5 µm), and large *Gephyrocapsa* (*G. caribbeanica* and *G. oceanica*; ≥5.5 µm). The zonal scheme and nannofossil biohorizons are shown in Figure F15 and Table T9.

Method

For nannofossil analyses, the core catcher sections of each core were sampled. Samples from other sections were sometimes included where nannofossils were not abundant in core catcher material, and many such samples were targeted specifically in burrows. Standard smear slide methods were utilized for all samples using optical adhesive as a mounting medium. Calcareous nannofossils were examined under a light polarizing microscope at 1250× magnification. Abundance, preservation, and zonal data for each sample investigated were recorded in the J-CORES database.

We followed the taxonomic concepts summarized in Takayama and Sato (1987) (Deep Sea Drilling Project Leg 94). Calcareous nannofossil preservation was based on the following:

G = good (little or no evidence of dissolution and/or overgrowth).
M = moderate (minor dissolution or crystal overgrowth observed).
P = poor (strong dissolution or crystal overgrowth, many specimens unidentifiable).

Total abundance of calcareous nannofossils for each sample was estimated as

A = very abundant (>50 specimens per field of view [FOV]).
C = common (>10–50 specimens per FOV).
F = few (>1–10 specimens per FOV).
R = rare (1 specimen per 2 or more FOVs).

Nannofossil abundances of individual species were recorded as

A = abundant (1–10 specimens per FOV),
C = common (1 specimen per 2–10 FOVs), and
R = rare (1 specimen per >10 FOVs).

As a way to check these abundances, we compared these abundances with carbonate content and relative percentages of calcite from bulk XRD.

Planktonic foraminifers

The planktonic foraminifer zonation of Blow (1969) and astronomically calibrated biohorizons of Neogene planktonic foraminifers compiled by the ICS in 2004 (Lourens et al., 2004) were applied for this expedition. The LO of *Globigerinoides ruber rosa* has been located at 0.12 Ma in the Indian and Pacific Oceans (Thompson et al., 1979) and confirmed by others (i.e., Li et al., 2005, at ODP Site 1143, South China Sea). The LOs of *Neogloboquadrina asanoi* and *Globoquadrina dehiscens* and the FO of *Globoconella inflata* modern form were correlated to geomagnetic polarities at ODP Sites 1150 and 1151 off northeast Japan (Motoyama et al., 2004). These foraminifer zonations and biohorizons are shown in Figure **F15** and Table **T10.**

Method

About 10 cm^3 of sediment from core catcher sections was collected for foraminifer analyses. Soft-sediment samples were disaggregated using a hydrogen peroxide solution. Firm mudstone or hard rock samples were treated by the sodium tetraphenylborate method (Hanken, 1979). After samples became macerated, each sample was wet-sieved through a screen (63 µm opening). Planktonic foraminifer specimens >125 µm were taken from the dried residues. Semiquantitative estimates of the relative abundance of species were made as follows:

+ = present (<4% or species from samples yielding <100 total individuals).
R = rare (4% to <8%).
C = common (8% to <16%).
A = abundant (>16%).

Preservation of each sample was recorded by the following criteria:

G = good (there is no dissolution; fragmentation of individuals has slightly occurred).
M = moderate (dissolution and fragmentation are commonly evident, and some of individuals are hard to identify).
P = poor (dissolution of surface structure and fragmentation are observed, and most of the individuals cannot be identified at the species level).

Paleomagnetism

Paleomagnetic and rock magnetic investigations on board the *Chikyu* during Expedition 322 were primarily designed to determine the characteristic remanence directions for use in magnetostratigraphic and tectonic studies. Routine measurements on archive halves could not be conduced with the superconducting rock magnetometer (SRM) because of the reason described in **"Superconducting rock magnetometer,"** so paleomagnetic measurements were performed only on discrete minicores and cube samples taken from the working halves.

Laboratory instruments

The paleomagnetism laboratory on board the *Chikyu* houses a large (7.3 m × 2.8 m × 1.9 m) magnetically shielded room, with its long axis parallel to the ship transverse. The total magnetic field inside the room is ~1% of Earth's magnetic field. The room is large enough to comfortably handle standard IODP core sections (~150 cm). The shielded room houses the equipment and instruments described in this section.

Superconducting rock magnetometer

The long-core SRM (2G Enterprises, model 760) unit is ~6 m long with an 8.1 cm diameter access bore. A 1.5 m split core liner can pass through a magnetometer, an alternating-field (AF) demagnetizer, and an anhysteretic remanent magnetizer. The system includes three sets of superconducting pickup coils, two for transverse moment measurement (*x*- and *y*-axes) and one for axial moment measurement (*z*-axis). The noise level of the magnetometer is $<10^{-7}$ A/m for a 10 cm^3 volume rock. The magnetometer includes an automated sample handler system (2G804) consisting of aluminum and fiberglass channels designated to support and guide long core movement. The core itself is positioned in a nonmagnetic fiberglass carriage that is pulled through the channels by a rope attached to a geared high-torque stepper motor. A 2G600 sample degaussing system is coupled to the SRM to allow automatic demagnetization of samples up to 100 mT. The system is controlled by an external computer and enables programming of a complete sequence of measurements and degauss cycles without removing the long core from the holder.

During the repair work of thrusters on the *Chikyu,* the SRM was warmed up to room temperature. In February 2009, the SRM was cooled down to liquid helium (He) temperature to prepare for Expeditions 319 and 322, and it was found that the *y*-axis superconducting quantum interference device (SQUID) was malfunctioning. Before the beginning of Expedi-

tion 319, the SRM was warmed up to room temperature and sent back to the manufacturer. The *y*-axis SQUID was replaced with a new one in the factory during Expedition 319, and the SRM was transported from the manufacturer, set up, refilled with liquid He, and cooled down to liquid He temperature during the port call at Yokkaichi before Expedition 322. During the port call, a leakage of He was found in the high vacuum surrounding the helium dewar, and liquid He evaporated more quickly than usual. Before starting the measurement of Expedition 322 archive halves, liquid He in the dewar of the SRM was almost empty and the SQUID stopped working. Thus, for the paleomagnetic study of Expedition 322, we could only measure remanent magnetization of discrete samples with the spinner magnetometer (see below). It is worthy to point out that the helium gauge in the reservoir reads 15% when it actually is empty. This nonzero gauge problem should be fixed before the next IODP expedition in addition to the problem of He leakage.

Spinner magnetometer

A spinner magnetometer, model SMD-88 (Natsuhara Giken Co., Ltd.) was utilized during Expedition 322 for remanent magnetization measurement. The noise level is ~5×10^{-7} mAm^2, and the measurable range is from 5×10^{-6} to 3×10^{-1} mAm^2. Two holders are prepared for the measurements, one (small or short) for the weak samples and the other (large or tall) for the strong samples. Five standard samples with different intensities are prepared to calibrate the magnetometer. Standard 2.5 cm diameter × 2.2 cm long samples taken with a minicore drill or 7 cm^3 Natsuhara cubes can be measured in three or six positions with a typical stacking of 10 spins. The whole sequence takes ~1 and 2 min, respectively. Sedimentary rocks recovered from Expedition 322 all have natural remanent magnetization well above the spinner's minimum limit, making the spinner a unique workhorse during Expedition 322. Basaltic rocks were measured with the large holder; however, one of the basaltic rocks could not be measured with an error "Too strong specimen" after demagnetization at ~5 mT. Because the spinner could not give stable readings after this measurement, the actual reason for the error cannot be determined.

Alternating-field demagnetizer

The AF demagnetizer DEM-95 (Natsuhara Giken Co., Ltd.) is set for demagnetization of standard discrete samples of rock or sediment. The unit is equipped with a sample tumbling system to uniformly demagnetize up to a peak AF of 180 mT. Most of the paleomagnetic samples from Expedition 322 sites were progressivly demagnetized with this instrument to isolate various magnetic components of the samples. Whenever possible, demagnetization was continued up to 180 mT until an unambiguous and reliable determination of polarity of the stable component of magnetization had been achieved.

Thermal demagnetizer

The thermal demagnetizer TDS-1 (Natsuhara Giken Co., Ltd.) has a single chamber for thermal demagnetization of dry samples over a temperature range from room temperature to 800°C. The chamber holds up to 8 or 10 cubic or cylindrical samples, depending on the exact size. The oven requires a closed system of cooling water, which is conveniently placed next to the shielded room. A fan next to the µ-metal cylinder that houses the heating system is used to cool samples to room temperature. The measured magnetic field inside the chamber is <20 nT. Representative sister samples in relation to the AF demagnetized samples were stepwisely heated to determine magnetic components and their unblocking temperatures.

Pulse magnetizer

The pulse magnetizer MMPM 10 (Magnetic Measurement, Ltd., UK; **www.magnetic-measurements.com**) can produce a high magnetic field pulse in a sample. The magnetic field pulse is generated by discharging a bank of capacitors through a coil. A maximum field of 9 T with a 7 ms pulse duration can be produced by the 1.25 cm diameter coil. The other coil (3.8 cm diameter) generates a maximum field of 2.9 T. We used this apparatus with the larger diameter coil during Expedition 322 to impart magnetic fields to three axes of a sample before progressive thermal demagnetization.

Anisotropy of magnetic susceptibility

The Kappabridge KLY 3S (AGICO, Inc.), designed for anisotropy of magnetic susceptibility (AMS) measurement, is also available on the *Chikyu*. Data are acquired from spinning measurements around three axes perpendicular to each other. Deviatoric susceptibility tensor can then be computed. An additional measurement for bulk susceptibility completes the sequence. Sensitivity for AMS measurement is 2×10^{-8} (SI). Intensity and frequency of field applied are 300 mA/m and 875 Hz, respectively. This system also includes the temperature control unit (CS-3/CS-L) for temperature variation of low-field magnetic susceptibility of samples. During Expedition 322, only a limited number of samples were subjected to AMS measurements because the science party needed to concentrate on the nonautomatic measurements of

remanent magnetization for shipboard magnetostratigraphy with the spinner magnetometer at many demagnetization steps. For the samples without AMS measurements, only bulk susceptibility was measured on discrete paleomagnetic samples.

Discrete samples and sampling coordinates

Discrete cubic samples (~7 cm^3) or minicores (~11 cm^3) were taken two per section from the working halves in order to determine paleomagnetic direction primarily for magnetostratigraphy. The actual spacing depended on the properties of the core material (e.g., to avoid flow-in, coring disturbances, etc.) and the distribution of interbedded lithologies. For the most part, paleomagnetic sampling concentrated on hemipelagic mud(stone) as the dominant lithology. The orientation of discrete samples is shown in Figure **F16.**

Measurements

Stepwise demagnetization experiments were conducted on discrete paleomagnetic samples using the AF demagnetizer. For a limited number of samples, stepwise thermal demagnetization was conducted. Acquisition of isothermal remanent magnetization and its thermal demagnetization was conducted on several samples after AF demagnetizaion. In addition to standard paleomagnetic measurements, the AMS was measured on a limited number of discrete samples. For the rest of the samples, only bulk magnetic susceptibility was measured using the Kappabridge KLY 3S magnetic susceptibility meter.

Orientation of discrete samples

We planned for orientation of discrete samples relative to the geographic frame by matching the characteristic features such as fractures or bedding between X-ray CT images and oriented borehole images. However, it was not possible because of the termination of the operation without taking any borehole images at the sites during Expedition 322.

Paleomagnetic reorientation of cores

Azimuthal orientation of drilled core material is of prime importance when modeling directional properties of rock formations. Paleomagnetic core reorientation has been successfully used for a number of years (e.g., Fuller, 1969; Kodama, 1984; Shibuya et al., 1991). The procedure is based on determining the direction of stable remanent magnetization (either viscous remanent magnetization [VRM] or primary magnetization) with respect to a common reference line that is marked lengthwise along the core. Assuming a moderate sedimentation rate of ~5 cm/k.y. and a magnetization lock-in depth of ~10 cm, a typical sample depth interval of 2.5 cm might be enough to average the secular variation of the geomagnetic field, and the paleomagnetic direction roughly points in the direction of geographic north. During Expedition 322, the VRM or primary magnetization after removal of drilling-induced remanent magnetization above 10 mT was used to reorient the blocks with important directional structural features (see **"Structural geology"**).

Magnetic reversal stratigraphy

Magnetic polarity was determined based on the sign of inclination. Sites C0011 and C0012 have a latitude of 32°50′N (32°45′N), which translates into an expected inclination of ±52.2° (±52.1°). This inclination is steep enough to distinguish the magnetic polarity (normal or reversed) on the sign of the magnetic inclination (positive or negative) for at least Neogene and Quaternary sediments even with the expected tectonic latitudinal migration. The demagnetization behavior of remanent magnetization was inspected visually on the demagnetization plots (e.g., Zijderveld plots). Stable (primary) remanent magnetization directions of discrete samples were fit using principal component analysis (Kirschvink, 1980), and the obtained inclination was used for the determination of paleomagnetic field polarity.

Geomagnetic polarity changes are the most frequent, best-dated, and globally synchronous geophysical phenomena. Magnetostratigraphy is a tool of great promise for precise temporal correlation and accurate dating in sediments. It is based on the facts that Earth's magnetic field has occasionally reversed its polarity and that many sedimentary rocks retain a magnetic imprint of the field at the time they were deposited. Because the length of time for the geomagnetic field to flip from one polarity state to the other is only a few thousand years, the boundaries between magnetozones (stratigraphic zones of single polarity) in sections of magnetized rocks are extremely sharp, much sharper than between typical biostratigraphic zones. During Expedition 322, magnetozones were recognized on the basis of distinct intervals of magnetic reversal zones and biostratigraphic datum events. Specifically, if the approximate age of the sediment is known from biostratigraphic information, it should serve as an anchor point to allow us to focus on a particular part of the established polarity timescale, and thus to identify specific reversals in the sedimentary sequence. Normal polarity subchrons are referred to by adding suffixes (n1, n2) that increase with age. For the younger part of the timescale (Pliocene–Pleistocene) we use traditional names to refer to the various chrons and

subchrons (e.g., Brunhes, Jaramillo, Olduvai, etc.). In general, polarity reversals occurring at core ends have been treated with caution. The ages of the polarity intervals used during Expedition 322 are the same as those for Expeditions 315 and 316, which is the magnetostratigraphic timescale for Neogene by Lourens et al. (2004) (Table T11).

For calcareous nannofossil zonations, Raffi et al. (2006) was used as a standard timescale for the entire NanTroSEIZE, including this expedition (see "Biostratigraphy"). They rely on ATNTS2004 (Lourens et al., 2004). Although the magnetostratigraphic timescale on their figures incorporated slight modifications to ATNTS2004, there is no clear explanation with an appropriate table for these modifications. Because of this and the fact that there is no significant change affecting the main chron boundaries, we used ATNTS2004 (Lourens et al., 2004) for consistency within NanTroSEIZE expeditions. We used corrected boundary ages for Chron C5ABn listed as "13.252 13.466 C5ABn" in the GPTS table used for Expeditions 315 (Expedition 315 Scientists, 2009, table T7) and 316 (Expedition 316 Scientists, 2009, table T10) with the values of 13.369 (top) and 13.605 (bottom) according to Lourens et al. (2004). For the up-to-date Neogene GPTS for reference, we need to consider the discussion by Hilgen (2008), especially for Chrons C7n through C5Cn.1n between 24.1 and 15.9 Ma and chron boundaries in the interval between 12.5 and 8.5 Ma. These might be included in the shore-based study and for future NanTroSEIZE expeditions.

Data reduction and software

Data reduction (Zijderveld demagnetization plots and equal area projections) was conducted by using a visualization software called Progress installed on the PC controlling the spinner magnetometer described above. Principal component analysis (Kirschvink, 1980) was also performed by using Progress software to determine characteristic remanent magnetization directions. In addition, Igor Pro software (Wavemetrics Co., Inc.) was used for data analysis and plotting in combination with Microsoft Excel.

Physical properties

Physical property measurements provide valuable constraints on bulk physical character to augment lithologic unit characterization and to facilitate correlation of downhole logging data with discrete core measurements and core descriptions. Thus, these data provide information necessary for reliable core-log-seismic integration. Expedition 322 employed multiple approaches and methods to characterize the physical properties of cores. Prior to core physical property measurements, X-ray CT images were collected for all cores, and cores were equilibrated with room temperature (~20°C). After temperature equilibration, whole-round core sections were processed in the MSCL-W to measure GRA density, magnetic susceptibility, natural gamma radiation, *P*-wave (compressional) velocity, and electrical resistivity. For cores with soft, unconsolidated sediments, thermal conductivity was measured using a TeKa thermal conductivity meter with the VLQ full-space needle probe inserted in whole-round cores after MSCL-W measurements. Cores were then split into archive and working halves. For cores with lithified sediments, where a needle probe could not be inserted, thermal conductivity measurements were made on working halves using the TeKa thermal conductivity meter in half-space mode. Discrete samples were collected from the working halves for MAD measurements. Specimen mass was taken with a BAL-2 motion-compensated shipboard balance system. The volume of solids was measured with a Quantachrome penta-pycnometer. For soft sediments, undrained shear strength at discrete intervals from the working halves was determined from vane shear measurements made with a Wykeham Farrance WF23544 vane apparatus and penetrometer measurements made with a Geotest E-284B penetrometer. *P*-wave velocity and electrical resistivity were measured on discrete core samples in the *x*-, *y*-, and *z*-directions (Fig. F17) to evaluate anisotropy of velocity and resistivity. Archive halves were scanned for image and color measurements. Details and procedures for each physical property measurement are described below.

MSCL-W

GRA density

Bulk density can be used to evaluate pore volume in sediment, which is used to evaluate the consolidation state of sediment. GRA density is based on the detection of a gamma ray beam produced by a cesium source. The beam, produced by a ^{137}Cs gamma ray source at a radiation level of 370 MBq within a lead shield with a 5 mm collimator, is directed through whole-round cores. The gamma ray detector includes a scintillator and an integral photomultiplier tube to record the gamma rays that pass through the whole-round core. GRA bulk density (ρ_b) is defined by:

$$\rho_b = \ln(I_0/I)\mu d, \quad (20)$$

where

I_0 = gamma ray source intensity,

I = measured intensity of gamma rays passing through the sample,
μ = Compton attenuation coefficient, and
d = sample diameter.

The Compton attenuation coefficient (μ) and source intensity (I_0) are treated as constants, so ρ_b can be calculated from I. The gamma ray detector is calibrated with a sealed calibration core (a standard core liner filled with distilled water and aluminum cylinders of various diameters). To establish the calibration curves, gamma ray counts were taken through each aluminum cylinder for 60 s. Each aluminum cylinder has a density of 2.7 g/cm^3, and d is 1, 2, 3, 4, 5, or 6 cm. The relationship between I and μd is:

$$\ln(I) = A(\mu d)^2 + B(\mu d) + C, \quad (21)$$

where A, B, and C are coefficients determined from the calibration experiment. GRA density measurements on core samples were conducted every 4 cm for 4 s. The spatial resolution was 5 mm.

Magnetic susceptibility

Magnetic susceptibility is the degree to which a material can be magnetized by an external magnetic field. Therefore, magnetic susceptibility provides information on sediment composition. A Bartington loop sensor with an 8 cm diameter was used to measure magnetic susceptibility. An oscillator circuit in the sensor produces a low-intensity (~80 A/m RMS), nonsaturating, alternating magnetic field (0.565 kHz). This pulse frequency is converted into magnetic susceptibility. The spatial resolution of the loop sensor is 23–27 mm, and it is accurate to within 2%. Magnetic susceptibility data were collected every 4 cm along the core.

Natural gamma radiation

Natural gamma radiation measurements provide insights into sediment composition and thus can be used to identify lithology. Whole-round cores were monitored for natural gamma ray (NGR) emissions to obtain spatial variability in radioactivity and establish gamma ray logs of cores for correlation to downhole gamma ray logs. A lead-shielded counter, optically coupled to a photomultiplier tube and connected to a bias base that supplied high-voltage power and a signal preamplifier, is used. Two horizontal and two vertical sensors are mounted in a lead, cube-shaped housing. The NGR system records radioactive decay of long-period isotopes ^{40}K, ^{232}Th, and ^{238}U. NGR has a resolution of 120–170 mm and was measured every 16 cm with a count time of 30 s. Background radiation noise was determined by taking measurements on a water-filled calibration core.

P-wave velocity

P-wave data can be used to evaluate small-strain moduli, to correlate between log and core data, and to evaluate pore structure and cementation. *P*-wave (compressional) velocity (V_P) is defined by the time required for a compressional wave to travel a set distance:

$$V_P = d/t_{core}, \quad (22)$$

where

d = path length of the wave across the core and
t_{core} = traveltime through the core.

P-wave velocity transducers on the MSCL-W system measure total traveltime of the compressional wave between transducers. The wave travels horizontally across the whole core and core liner. The total traveltime observed is composed of

t_{delay} = time delay related to transducer faces and electronic circuitry,
t_{pulse} = delay related to the peak detection procedure,
t_{liner} = transit time through the core liner, and
t_{core} = traveltime through the sediment or rock.

The system is calibrated using a core liner filled with distilled water, which provides control for t_{delay}, t_{pulse}, and t_{liner}. With these calibrations, core velocity (V_P) can be calculated on whole-round specimens in core liners:

$$V_P = (d_{cl} - 2d_{liner})/(t_o - t_{pulse} - t_{delay} - 2t_{liner}), \quad (23)$$

where

d_{cl} = measured diameter of core and liner,
d_{liner} = liner wall thickness, and
t_o = measured total traveltime.

Equation 23 assumes that the core completely fills the core liner.

Electrical resistivity

Within limits, electrical resistivity may be useful for estimating other sediment physical properties, including porosity, tortuosity, permeability, and thermal conductivity. Bulk electrical resistivity is controlled by solid grain resistivity, interstitial water resistivity, pore space distribution, and pore connectivity. Electrical resistivity (ρ) is defined by the electrical resistance and geometry of the core measured:

$$\rho = R(A/L), \quad (24)$$

where

R = electrical resistance,
L = length of measurement, and
A = cross-sectional area of the core.

The noncontact resistivity sensor on the MSCL-W system induces a high-frequency magnetic field in the core with a transmitter coil. This generates an electrical current in the bulk sediment that is inversely proportional to its resistivity. The secondary magnetic field generated by this induced electrical current is measured by a receiver coil. To measure this smaller magnetic field accurately, a differencing technique has been developed that compares readings from the sample core to readings from an identical set of coils operating in air. Electrical resistivity data were obtained at 4 cm intervals on the MSCL-W.

MSCL-I: photo image logger

The photo image logger (MSCL-I) scans the surface of archive-half cores and creates a digital image. The line-scan camera equips three charge-coupled devices; each charge-coupled device has 1024 arrays. Light reflection from the sample surface passes through the lens and is split into three paths (red, green, and blue) by a beam splitter inside the line-scan camera. Then, each reflection is detected by the corresponding charge-coupled device. Finally, the signals are combined and the digital image is reproduced. Optical distortion downcore is avoided by precise movement of the camera. Spatial resolution is 100 pixels/cm.

For publication, a modified image was used in VCD tables. Image lightness was modified so that the values of the gray standard attached to the bottom of a section is somewhere near 100/100/100. This processing was done by using the image data of Core 322-C0011B-1R-1, then the same adjustments were automatically applied to all other sections through Expedition 322.

MSCL-C: color spectroscopy logger

A color spectrophotometer (Konica-Minolta, CM-2600d) is included on the color spectroscopy logger (MSCL-C) system. The xyz-type aluminum frame allows operators to set a maximum of seven core sections on the tray, and the sensor unit (including the spectrophotometer and small distance measuring system using a laser sensor) moves over each section and down at each measurement point to measure the split archive core surface.

Light reflected from the sample surface is collected in the color spectrophotometer's integration sphere. The instrument's structure allows for the specular component to be included (SCI setting) or excluded (SCE setting). The SCE setting is the recommended mode of operation, especially for sediments, to exclude glare. The light is then divided into wavelengths at a 10 nm pitch (400–700 nm), and the spectral sensors in the sphere convert the light to electrical currents proportional to the intensity of the light. Next, the color spectrum from the sample is normalized by the source light of the reflectance. The obtained spectrum is calibrated with the measurement of a pure white standard, which has a high reflectance true value at visible wavelengths and is measured by the vendor, and a black box (zero calibration). Measurements can be calculated based on the 2° or 10° standard observer and any of 11 illuminants.

Color reflectance is categorized as an IODP standard measurement, and the measured color spectrum is normally converted to L*, a*, and b* parameters. L*, a*, and b* provide relative changes in the composition of the bulk material and are widely used to correlate sections from core to core or hole to hole and to analyze the characteristics and cyclicity of lithologic changes.

Moisture and density measurements

Discrete samples from working-half cores are used for determination of index properties (e.g., bulk density, grain density, dry density, water content, porosity, and void ratio). Index properties are determined from phase relations, mass measurements on wet and dry specimens, volume measurements on dry specimens, and corrections for salinity. In general, two discrete samples of homogeneous lithology for index properties were collected from each core section. Where whole-round samples were taken (e.g., interstitial water sample, community whole round, or individual sample requests) a MAD sample was taken adjacent to the whole-round sample as part of a cluster sample. Sample intervals and frequency were occasionally shifted to select minimally disturbed, homogeneous samples. Lithology was noted as sand for discrete samples that contained mostly sand grains judging from visual inspection. All other samples were noted as mud. Each discrete MAD sample was ~5 cm^3.

Wet and dry masses were measured using a paired electronic balance system, which is designed to compensate for the ship's heave. The sample mass was counterbalanced with a precisely known mass (10 g) that was within 5 g of the sample mass. The sample mass was determined to a precision of ±0.01 g. The balance system was calibrated ~8 times each day (~3 h interval).

To minimize desiccation, MAD sample collection was followed immediately by measurement of wet sediment mass (M_{wet}). After M_{wet} measurements, samples were dried in a convection oven at 105° ± 5°C for 24 h. Dry samples were placed in a desiccator for at least 1 h to equilibrate to room temperature (~20°C),

and then dry sediment mass (M_{dry}) and volume (V_{dry}) were measured. A five-chamber Quantachrome penta-pycnometer was used to measure V_{dry} with a helium-displacement technique providing a precision of ±0.04 cm³. The five-chamber system allowed the measurement of four sample volumes and one calibration sphere. Each measured volume (V_{dry}) is the average of five volume measurements. The calibration sphere was rotated between all measurement chambers to monitor for errors in each chamber. The pycnometer was calibrated at least once per 24 h. In cases where pycnometer-derived grain density was deemed unreliable (<2.0 g/cm³ or >3.0 g/cm³), the sample grain density was recalculated after dry mass and dry volume were remeasured.

Standard ODP/IODP practices were used to determine interstitial water mass and volume, salt mass and volume, and solid grain mass and volume (Blum, 1997). From these data, bulk density, dry density, grain density, porosity, and void ratio were calculated (Blum, 1997). Standard seawater density (1.024 g/cm³), salinity (35‰), and constant salt density (2.22 g/cm³) were assumed for all calculations.

Water content

Water content (W_c) was determined following the American Society for Testing and Materials (ASTM) standard D2216 (ASTM International, 1990). Corrections are required for salt when measuring the water content of marine samples. In addition to the water content calculation in ASTM D2216 (i.e., the ratio of interstitial water mass to dry sediment mass) (W_c[dry]) we also calculated the ratio of interstitial water mass to total sample mass (W_c[wet]). The equations for water content are

$$W_c(\text{dry}) = (M_{wet} - M_{dry})/(M_{dry} - sM_{wet}), \quad (25)$$

and

$$W_c(\text{wet}) = (M_{wet} - M_{dry})/M_{wet}(1 - s), \quad (26)$$

where

M_{wet} = total mass of the discrete sample,
M_{dry} = mass of the dry sample, and,
s = salinity (assumed constant at 0.035).

Bulk density

Bulk density is the density of the discrete core sample ($\rho_b = M_{wet}/V_t$). Total wet sample mass (M_{wet}) was measured immediately after collecting each discrete sample using the dual-balance system. Total sample volume assuming 100% saturation ($V_t = V_g + V_{IW}$) was determined from the pycnometer measurement of grain volume (V_g) and calculated volume of interstitial water (V_{IW}). Solid grain and interstitial water volume are determined as

$$V_g = V_{dry} - (M_{wet} - M_{dry})s/\rho_{salt}(1 - s), \quad (27)$$

and

$$V_{IW} = (M_{wet} - M_{dry})/\rho_{IW}(1 - s), \quad (28)$$

where

V_{dry} = dry volume,
ρ_{salt} = salt density (assumed constant at 2.22 g/cm³), and
ρ_{IW} = standard seawater density (1.024 g/cm³).

Porosity and void ratio

Porosity (ϕ) relates the volume of the pores to the total sample volume; void ratio (e) relates the pore volume to the volume of the solid grains. They are calculated as

$$\phi = \rho_b V_{IW}/M_{wet}, \quad (29)$$

and

$$e = V_{IW}/V_g. \quad (30)$$

Grain density

Grain density (ρ_g) was determined from measurements of dry mass and dry volume made with the dual-balance system and the pycnometer, respectively. Mass and volume were corrected for salt, yielding

$$\rho_g = \frac{M_{dry} - M_{salt}}{V_{dry} - \dfrac{(M_{wet} - M_{dry})s}{\rho_{salt}(1 - s)}}, \quad (31)$$

where

M_{salt} = mass of salt.

Shear strength measurements

The undrained shear strength of soft sediments in the working half of the core was measured using an analog vane shear device (Wykeham Farrance, model WF23544) and a pocket penetrometer (Geotest E-284B). Measurements were made at discrete locations on the working halves above the depth where sediments behaved in a brittle manner; this corresponded to measureable shear strength <125 kPa. Where possible, the measurements were made near MAD samples. Care was taken to conduct tests within minimally disturbed, homogeneous sedi-

ments. Measurements were made on the working half of split cores with vane rotation axis and penetrometer penetration direction perpendicular to the *y*-*z* plane of the core (Fig. F17).

Vane shear strength ($S_{u[v]}$) can be determined by the torque required to cause failure (T) and a vane constant (K_v):

$$S_{u(v)} = T/K_v. \quad (32)$$

All vane shear strength measurements were obtained using a vane with a height of 12.7 mm and a blade length of 6.35 mm. Failure torque was determined by measuring the rotation of a torsional spring using a spring-specific relation between rotation angle and torque. Vane shear strength results were only reliable for samples with vane shear strength <125 kPa. When cracking or core separation occurred, measurements were discarded. Below the depth where strength exceeded 125 kPa, no measurements were made.

The pocket penetrometer provides a measure of unconfined compressive strength (q_u), which can be related to undrained shear strength ($S_{u[penet]}$):

$$S_{u(penet)} = q_u g/2, \quad (33)$$

where

g = acceleration due to gravity, and
q_u = mass per area.

Unconfined compressive strength is calculated from the penetration resistance generated by pushing a cylindrical probe 6.4 mm into the *y*-*z* plane of the core. The average of three adjacent penetrometer tests in intact, homogeneous sediment is the recorded unconfined compressive strength. Measurements were obtained using a flat surface probe with a diameter of 6.4 mm. After shear strength exceeded ~125 kPa, no penetrometer measurements were made.

Anisotropy of *P*-wave velocity and electrical resistivity

P-wave velocity and electrical resistivity measurements were performed on cubic samples cut from RCB cores with a diamond blade saw. Samples for *P*-wave velocity measurements were ~20 mm × 20 mm × 20 mm; samples for electrical resistivity measurements were ~10 mm × 10 mm × 10 mm. All cubes were cut with faces orthogonal to the *x*-, *y*-, and *z*-axes of the core reference (Fig. F17). Hard rock/basement cubes were saturated in a 3.5% NaCl solution for 24 h prior to *P*-wave analysis. All cubes used for electrical resistivity analysis were saturated in a 3.5% NaCl solution for 6 h prior to measurement. This sample preparation and three-component measurement plan enable first-order measurement of both *P*-wave velocity and electrical resistivity anisotropies.

To measure *P*-wave velocity in a given direction, a *P*-wave logger for discrete samples (PWL-D) was used. The PWL-D has two 230 kHz transducers, one used as a transmitter and one as a receiver, and a laser distance sensor. A sample was placed between the transducers and held in place with a vertical mass of 2.5 kg. The transmitter was connected to a pulse generator, and the receiver was connected to an oscilloscope synchronized with the pulse generator. The oscilloscope signal was digitally displayed; *P*-wave total traveltime (t) for the first arrival was picked and recorded. The laser distance sensor provided the sample length (L). The velocity in any direction (e.g., V_{Px}) was defined by the sample length (e.g., L_x), total traveltime (t_x), and system-calibrated delay time (t_{delay}):

$$V_{Px} = L_x/(t_x - t_{delay}). \quad (34)$$

Calibration of the traveltime delay and laser distance sensor was conducted daily. Traveltime delay was determined by placing the transmitter and receiver in direct contact and measuring traveltime. The laser distance sensor was calibrated by placing the transmitter and the receiver in direct contact and then spacing them using a 2.5 cm long reference specimen. Routine quality control measurements were made by measuring velocity on glass and acrylic standards with known lengths and velocities.

An Agilent 4294A component analyzer was used to measure electrical resistivity. The bridge method was used, and a two-terminal circuit was connected for measurement. Each specimen cube was placed between two stainless steel electrodes covered with seawater-saturated filter papers. The magnitude ($|Z|$) and phase (θ) of the complex impedance were measured at 25 kHz between opposite cube faces. The cube was rotated to measure impedance in the *x*-, *y*-, and *z*-directions (Fig. F17). Electrical resistivity for each direction (e.g., ρ_x) was computed from the complex impedance measured in each direction (e.g., x) and sample dimensions defined by face length (L):

$$\rho_x = |Z_x|\cos\theta_x\,(L_y L_z)/L_x). \quad (35)$$

With *P*-wave velocity and electrical resistivity measured in the *x*-, *y*-, and *z*-directions, the anisotropy is calculated following the approach of Carlson and Christensen (1977). Some sources for anisotropy include: (1) alignment of pores during consolidation, (2) fabric development, and (3) microstructures such as microfractures and microcracks. The anisotropy

calculation compares the horizontal (x, y) and vertical (z) components of P-wave velocity and electrical resistivity expressed as a percentage of the mean (e.g., Shipboard Scientific Party, 2001a):

$$a_{VPhor}\ (\%) = 200[(V_{Px} - V_{Py})/(V_{Px} + V_{Py})], \quad (36)$$

$$a_{VPvert}\ (\%) = 200[(V_{Px} + V_{Py})/2 - V_{Pz}] /[(V_{Px} + V_{Py})/2 + V_{Pz}], \quad (37)$$

$$a_{\rho hor}\ (\%) = 200[(\rho_x - \rho_y)/(\rho_x + \rho_y)], \quad (38)$$

and

$$a_{\rho vert}\ (\%) = 200[(\rho_x + \rho_y)/2 - \rho_z] /[(\rho_x + \rho_y)/2 + \rho_z]. \quad (39)$$

Thermal conductivity

Thermal conductivity was measured on sediment and rock samples using either the full-space needle probe (Von Herzen and Maxwell, 1959) or the half-space line source (Vacquier, 1985), which approximates an infinite line source. In soft sediments where a probe could be inserted into the core without fracturing the sediment, the full-space probe was inserted into whole-core sections through a hole drilled in the working-half side of the core liner. When sediment strength precluded use of the full-space probe or good contact between the probe and sediment was not possible, the half-space probe was used on the working half of the split core. For unconsolidated samples, the half-space probe was placed directly on the split core with seawater used to provide good contact. Lithified samples were placed in a seawater bath for at least 15 min before measurement with the half-space probe. Both full- and half-space measurements produce a scalar thermal conductivity value in the plane perpendicular to the orientation of the probe.

All measurements of thermal conductivity were made after the cores had equilibrated to room temperature. At the beginning of each measurement, temperature in the sediment was monitored to ensure that thermal drift was <0.4 mK/min (typically within 1–2 min). After it was established that the temperature was near equilibrium, a calibrated heat source was applied and the rise in temperature was recorded for ~80 s. Values of thermal conductivity were based on the observed rise in temperature for a given quantity of heat.

The full-space needle probe was calibrated at least once every 24 h. The calibration was performed on one of two Macor samples of known thermal conductivity (1.611 ± 2% W/[m·K], 1.623 ± 2% W/[m·K]). Calibration procedures for the half-space system are similar to those for the full-space needle probe. Half-space calibrations were made on a Macor sample of known thermal conductivity (1.652 ± 2% W/[m·K]).

Inorganic geochemistry

Interstitial water collection

Interstitial water samples were obtained from 19 to 57 cm long whole-round sections from cores with >1.4 m of recovery. Samples were collected at a frequency of one per core if recovery was sufficient. Core length ranged between 2.2 and 9.5 m and core recovery varied from 0% to 110%, as listed in the lithology section of each site chapter.

Whole-round samples were cut and capped as quickly as possible after the core arrived on deck and immediately taken from the core cutting area to be scanned by X-ray CT. A watchdog (a shipboard structural geologist) viewed the composite X-ray CT scan to determine if there were structures that might warrant description and sampling from a split core. Once approved, the sediment was taken to the quality assurance/quality control (QA/QC) laboratory and immediately extruded from the core liner into a nitrogen-flushed glove bag. The exterior of the whole-round sample was thoroughly cleaned with a spatula to remove drilling contamination, and the cleaned sediment was placed into a 9 cm diameter Manheim-type titanium squeezer (Manheim, 1966) on top of a reagent-grade water (18.2 MΩ Millipore water) rinsed filter paper that was placed on two to four 320 mesh stainless steel screens. Sediments were squeezed at ambient temperatures and pressures no higher than 25,000 psi to prevent the release of interlayer water of clay minerals during the squeezing process. The interstitial water was collected through a 0.2 µM disposable polytetrafluoroethylene (PTFE) filter into a 60 mL acid-washed plastic syringe that was attached to the bottom of the squeezer assembly.

Interstitial water aliquots were collected for both shipboard and shore-based analyses (Table **T12**). High-density polyethylene (HDPE) sample vials for minor and trace element analysis were cleaned by immersion in 55°C 10% trace metal grade 12N HCl for a minimum of 24 h and were subsequently rinsed in Milli-Q water and dried in a class 100 laminar flow clean hood. Samples for minor and trace element shipboard analysis were acidified with optima-grade 6N HCl at least 24 h before analysis by inductively coupled plasma–atomic emission spectroscopy (ICP-AES) or inductively coupled plasma–mass spectrometry (ICP-MS). A 0.5 mL sample was collected in acid-washed minicentrifuge tubes for onboard analyses of dissolved iron and sulfide. Aliquots for shore-based isotopic and transition metals analyses, as well as for

I and ^{129}I measurements, were stored in acid-washed HDPE bottles. Additional aliquots for analyses of oxygen, hydrogen, dissolved inorganic carbon (DIC), lithium, and chloride isotopes were placed in 2 mL septum screw-lid glass vials; samples for DIC were treated with 10 µL of a saturated $HgCl_2$ solution at room temperature. Aliquots for shore-based characterization of volatile fatty acids were collected in septum screw-lid glass vials and immediately frozen at –20°C. After interstitial water extraction was complete, sediment squeeze cakes were divided (15–180 cm^3) and sealed in plastic bags for archive and shore-based analyses (Table **T13**). Sediment samples for archive and shore-based organic geochemical analyses were stored in a –20°C freezer; all other squeeze cake samples were stored at room temperature.

Correction for drilling contamination

In many intervals, the sedimentary material was extensively fractured by drilling disturbance (see **"Inorganic geochemistry"** in the "Site C0011" chapter), making some interstitial water whole rounds extremely difficult to clean prior to processing. In these cases, even after thorough cleaning, the interstitial water samples were still contaminated with fluid that had circulated in the borehole during drilling operations. In continental margin sediments, the sulfate–methane transition (SMT) zone is generally reached at shallow depths in the sediment section, typically shallower than ~40 m. Below this depth, sulfate generally remains depleted. Thus, the presence of sulfate and methane in a sample collected below the SMT may be used as an indication of drilling-induced contamination. For these cases, the sulfate concentrations measured in the samples were used to estimate the amount of drilling fluid introduced to the sample by taking the ratio of the sulfate measured in the sample to the sulfate concentration of seawater (28.9 mM). Likewise, concentration of the other ionic species were corrected based on their concentration in surface seawater using the following equation

$$X_{corrected} = [X_{measured} - (f_{sw} \times X_{sw})]/f_{IW}, \quad (40)$$

where

$X_{corrected}$ = corrected or in situ concentration of the analyte,
$X_{measured}$ = measured concentration of the analyte,
X_{sw} = analyte concentration in surface seawater (used in drilling),
f_{sw} = fraction of seawater introduced into the sample during drilling, and
f_{IW} = fraction of in situ interstitial water in the sample.

The fraction of seawater introduced by drilling disturbance and the fraction of in situ interstitial water are computed using Equations **41** and **42:**

$$f_{sw} = SO_{4\ measured}/SO_{4\ sw}, \quad (41)$$

and

$$f_{IW} = 1 - f_{sw}. \quad (42)$$

Both the measured and corrected interstitial water chemical concentration data are presented in the site chapters.

Interstitial water analysis

Interstitial water samples were routinely analyzed for refractive index with a RX-5000α refractometer (Atago) immediately after interstitial water extraction. The refractive index was converted to salinity based on repeated analyses of International Association of Physical Sciences of the Oceans (IAPSO) standard seawater. Precision for salinity was <0.1‰. Also, immediately after interstitial water extraction, samples were analyzed for pH and alkalinity by Gran titration with a pH electrode and a Metrohm autotitrator. Alkalinity titrations had a precision of <2%, based on repeated analysis of IAPSO standard seawater.

Sulfate and bromide concentrations were analyzed by ion chromatography (IC) (Dionex ICS-1500) using subsamples that were diluted 1:100 with Milli-Q water. At the beginning and end of each run, several different dilutions of IAPSO standard seawater were analyzed for quality control and to determine accuracy. IAPSO standard seawater was analyzed after every seventh sample as a check for instrumental drift and to calculate analytical precision. Precision for the bromide and sulfate analyses was <3% and <0.8%, respectively. Average accuracy of bromide and sulfate was <2% and 1.5%, respectively.

Chlorinity was determined via titration with silver nitrate ($AgNO_3$). We use the convention "chlorinity" for the titration data because it yields not only dissolved chloride but also all of the other halide elements and bisulfide. The average precision of the chlorinity titrations, expressed as 1σ standard deviation of means of multiple determinations of IAPSO standard seawater, is ≤0.5%.

Dissolved ammonium concentration was measured within 24 h of collecting the interstitial water sample by colorimetry, using an ultraviolet-visible (UV-vis) spectrophotometer (Shimadzu UV-2550) at an absorbance of 640 nm. A 0.1 mL sample aliquot was diluted with 1 mL of Milli-Q water, to which 0.5 mL phenol ethanol, 0.5 mL sodium nitroprusside, and

1 mL oxidizing solution (trisodium citrate and sodium hydroxide) were added in a capped plastic tube (Gieskes et al., 1991). The solution was kept in the dark at room temperature for >3 h to develop color. Precision and accuracy of the ammonium analyses were <2.5% and 3%, respectively.

Dissolved phosphate concentration was also measured by a colorimetric method using the UV-vis spectrophotometer at an absorbance of 885 nm. Because the phosphate concentration in the analysis solution must be <10 µM, appropriate aliquots of sample or standard solution (100 or 600 µL) were diluted with 1.1 mL of Milli-Q water (1000 or 500 µL) in a plastic tube. The mixed solution (ammonium molybdate, sulfuric acid, ascorbic acid, and potassium antimonyl tartrate) was added to the tube (Gieskes et al., 1991), which was capped and kept at room temperature to develop color. Precision and accuracy of the phosphate analyses were <2% and 2%, respectively.

Analyses of bisulfide/acid volatile sulfide (AVS) and ferrous iron were conducted within ~12 h after a subsample of interstitial water (200–1500 µL) was collected and stored in an anaerobic chamber under 98.2% N_2:H_2. For bisulfide/AVS analysis, an aliquot of interstitial water (>100 µL) was treated with either Hach proprietary sulfide reagents or 1N zinc acetate (5 µL/100 µL sample or standard reference solution), depending on the length of expected delay (due to core processing workflow and limited personnel available to help with spectrophotometry) before analysis could be performed. Aliquots of interstitial water for ferrous iron analyses (≥100 µL/100 µL sample or standard reference solution) were treated with 100X Ferrozine reagent in HEPES (4-[2-hydroxyethyl]piperazine-1-ethanesulfonic acid) buffer (1 µL) at pH 7. Analyses of reference standards stored anaerobically demonstrated the relative stability of both bisulfide and ferrous iron with respect to oxidation over 1–2 days.

Modifications of well-established spectrophotometric assays (Cline, 1969; Stookey, 1970) were used with a BioRad SmartSpec Plus UV-vis spectrophotometer capable of detecting nanomolar to micromolar concentrations of the two species of interest. Colorimetric assays measured absorbance at 562 nm for Fe(II) and 665 nm for S(II–). Absorbance for bisulfide was calibrated against Milli-Q washed $Na_2S{\cdot}9H_2O$ (25 parts per million [ppm] bisulfide standard measured by titration with thiosulfate and iodine reaction). Ferrozine-complexed ferrous iron absorbance was calibrated against a standard of ferrous ammonium sulfate hexahydrate in hydrochloric acid solution (1000 ppm) reacted with Ferrozine-HEPES buffer as above. Analyses of these reference standards stored anaerobically demonstrated the relative stability of both bisulfide and ferrous ion with respect to oxidation over 1–2 days. Colorimetric analyses required ~6–8 min total per sample once the suite of reference standard calibrations was performed (generally once per complete analytical run).

Concentrations of major cations (sodium, potassium, magnesium, and calcium) were analyzed by IC (Dionex ICS-1500) on samples acidified with 0.4% 6M HCl. Samples were diluted by a factor of 200 with ultrapure water (18.2 MΩ·cm). Each measurement batch included an ultrapure water blank, seven standards for calibration prepared from a commercially available cation mixed standard (KANTO CHEMICAL Co., Inc., P/N: 07197-96), and IAPSO standard seawater (P-series) as a reference material, in addition to the interstitial water samples. The average precision estimated by repeated measurements of 1/200 IAPSO standard seawater were Na^+ < 1.1%, K^+ < 1.2%, Mg^{2+} < 1%, and Ca^{2+} < 1.1%, and the average accuracy of the analyses were Na^+ < 2.4%, K^+ < 0.5%, Mg^{2+} < 0.8%, and Ca^{2+} < 0.4%. Because of the poor precision and accuracy of the sodium determination, which is typical of Na analysis by IC, Na concentration was computed by charge balance, where

$$[Na]_{calc} = \Sigma_{anion} - \Sigma_{cation}. \quad (43)$$

Sodium concentration determined by charge balance and by IC is tabulated in each of the site chapters, but only sodium concentration calculated by charge balance is plotted in the figures.

The minor elements (B, Ba, Fe, Li, Mn, Si, and Sr) were analyzed by ICP-AES (Horiba Jobin Yvon Ultima2). The interstitial water sample aliquot was diluted by a factor of 20 (0.5 mL sample added to 9.5 mL of 1% ultrapure double-distilled nitric acid solution spiked with 10 ppm yttrium). Because of the high concentration of matrix salts in interstitial water samples at a 1:20 dilution, matrix matching of the calibration standards is necessary to achieve accurate results by ICP-AES. A matrix solution that approximated seawater major ion concentrations was prepared by dissolving the following salts in 1 L of Milli-Q water acidified with 4 mL of optima-grade 6N HCl: 27 g NaCl, 3.8 g MgCl, 1.0 g $CaCO_3$, and 0.75 g KCl. Sulfate was not added to the matrix-matching solution because we expected the interstitial water sulfate concentration to decrease rapidly in the upper 20 m CSF, based on prior drilling results on this margin (Shipboard Scientific Party, 2001b; Tobin et al., 2009). Because the matrix solution was not a true blank, the procedural blank used was a dilution of the 1% nitric acid solution in the Y solution, and only the slope of the calibration curve was

used for quantification. A stock standard solution was prepared from ultrapure primary standards (SPC Science PlasmaCAL) in the 1% nitric acid solution. The stock solution was then diluted in the same 1% ultrapure nitric acid solution to concentrations of 50%, 25%, 10%, 5%, and 1%. A 1.25 mL aliquot of each stock solution was added to 8.75 mL of matrix solution to produce a series of standards that could be diluted using the same method as the samples for consistency. The final matrix-matched 100% standard solution contained the following concentrations: B = 3000 µM, Li = 400 µM, Si = 1000 µM, Mn = 50 µM, Fe = 50 µM, Sr = 400 µM, and Ba = 200 µM. A standard prepared in the 10% matrix-matching solution was repeatedly analyzed to calculate the precision of the method. The average precision of the minor element analyses were B < 1%, Ba < 1%, Fe < 1.8%, Mn < 2%, Li < 1%, Si < 2%, and Sr < 1.5%, and the average accuracy of the analyses were B < 1.5%, Ba < 2%, Fe < 2%, Mn < 2%, Li < 2%, Si < 3%, and Sr < 4%.

Vanadium, copper, zinc, molybdenum, rubidium, cesium, lead, and uranium were analyzed by ICP-MS (Agilent 7500ce ICP-MS) equipped with an octopole reaction system to reduce polyatomic and double-charge interferences. To calibrate for interferences by the major ions Na, Cl, K, Ca, and S on some of the transition metals (ClO and SOH on V, Na and CaOH on Cu, and S on Zn), solutions were prepared containing these elements at concentrations similar to IAPSO standard seawater values. These solutions were analyzed at the beginning of each run, and an interference correction was applied based on the average counts per second (cps) measured on the standard solutions divided by the abundance of the interfering elements. This ratio was multiplied by the known concentration of the major ions in the samples based on previous analysis, and the result was subtracted from the measured cps of the sample. A 100 µL aliquot of 500 parts per billion (ppb) indium standard was added to the empty analysis vials before dilution. Sample aliquots were then diluted with the 1% nitric acid solution to 3% in these vials (150 µL sample with 4.85 mL of 1% HNO_3 solution) based on previous determination of the detection limits and the concentrations of the elements of interest. A primary standard solution that matched the maximum range of predicted concentrations was made based on published results of deep-sea interstitial water compositions in a variety of settings. The composition of the standard is as follows: V = 20 ppb; Cu, Mo, Pb, and U = 40 ppb; Zn = 140 ppb; Rb = 500 ppb; and Cs = 5 ppb. This primary standard was diluted in the 1% nitric acid solution to relative concentrations of 50%, 25%, 10%, 5%, and 1%. These standards were then diluted to 3%, similar to the standards, with the addition of 150 µL of a 560 mM NaCl solution and 4.7 mL of the 1% HNO_3 solution to account for matrix suppression of the plasma ionization efficiency. The 25% standard was diluted accordingly and analyzed every eight samples throughout every analysis series for precision and in order to compare the results from different analysis dates. Blanks were also analyzed every eight samples, and detection limits were determined as three times the standard deviation of a procedural blank of Milli-Q water acidified with 4 mL of optima-grade 6N HCl per liter. The average precision of multiple determinations of the 10% ICP-MS standard was V < 6%, Cu < 14%, Zn < 3%, Mo < 0.8%, Rb < 0.7%, Cs < 12%, Pb < 3%, and U < 0.8%.

Organic geochemistry

The shipboard organic geochemistry program during Expedition 322 comprised analyses of dissolved gases including volatile hydrocarbons (C_1–C_4) and hydrogen (H_2), as well as analysis of the sediment for total carbon, nitrogen, and sulfur content and inorganic and organic carbon content. In addition, the type and maturity of organic matter was characterized using Rock-Eval pyrolysis. Procedures used during Expedition 322 follow Pimmel and Claypool (2001) and Expedition 316 Scientists (2009). H_2 analyses were an addition to the routine shipboard analytical program and employed a third-party laboratory instrument that was provided by the Organic Geochemistry Group of the MARUM Center for Marine Environmental Sciences (University of Bremen, Germany).

Hydrocarbon gases

Concentrations and distributions of light hydrocarbon gases, mainly methane (C_1), ethane (C_2), and propane (C_3), were monitored for each core following standard headspace sampling protocols. A 5 cm^3 sediment sample was collected with a cut-off plastic syringe from the freshly exposed end of the first section that was cut open in each core. In general, this was the section adjacent to the whole-round core cut for interstitial water sampling. When the sediments were too lithified, a cork borer was used to take the sample. The sample was extruded into a 24 mL glass vial and immediately sealed with a PTFE coated septum and metal crimp cap. The exact bulk mass of the wet sample was determined after the gas analysis was finished. For analysis of C_1–C_4 hydrocarbon gases, the vial was placed in a headspace sampler (Agilent Technologies G1888 network headspace sampler), where it was heated at 70°C for 30 min before an aliquot of the headspace gas was automatically injected

into an Agilent 6890N gas chromatograph (GC) equipped with a packed column (GL HayeSep R) and flame ionization detector (FID). The carrier gas was helium. In the temperature program of the GC the initial temperature of 100°C was held for 5.5 min before the temperature was ramped up at a rate of 50°C/min to 140°C and held for 4 min. Chromatographic response of the GC was calibrated against five different authentic standards with variable quantities of low molecular weight hydrocarbons and checked on a daily basis.

Methane concentration in interstitial water was derived from the headspace concentration using the following mass balance approach:

$$CH_4 = [\chi_M \times P_{atm} \times V_H]/[R \times T \times V_{IW}], \quad (44)$$

where

χ_M = molar fraction of methane in the headspace gas (obtained from GC analysis),
P_{atm} = pressure in the vial headspace (assumed to be the measured atmospheric pressure when the vials were sealed),
V_H = volume of headspace in the sample vial,
V_{IW} = volume of interstitial water in the sediment sample,
R = universal gas constant, and
T = temperature of the vial headspace in Kelvin.

The interstitial water volume in the sediment sample was determined based on the bulk mass of the wet sample (M_b), the sediment's porosity (ϕ, which was extrapolated from shipboard MAD measurements in adjacent samples, grain density (ρ_g), and the density of interstitial water (ρ_{IW}) as:

$$V_{IW} = M_{IW}/\rho_{IW} = [\phi \times \rho_{IW}] /[(1 - \phi) \times \rho_g] \times M_b/\rho_{IW}, \quad (45)$$

where

M_{IW} = interstitial water mass,
ρ_{IW} = 1.024 g/cm³, and
ρ_g = 2.8 g/cm³.

Hydrogen gas

Dissolved H_2 concentration was monitored using two different headspace equilibration techniques. For the first method, hereafter called the incubation method, ~5 cm³ of sediment was collected from the freshly cut section ends of whole-round cores that were taken for deep biosphere research. Ideally, sampling was conducted immediately after core recovery, but in a few cases samples needed to be stored for a few hours in N_2 flushed bags at 4°C prior to sampling. Samples were taken using sterile, cut-off plastic syringes and placed in 17 mL headspace vials that were closed with thick butyl rubber stoppers, crimp capped, and thoroughly flushed with N_2 in order to establish an O_2- and H_2-free gas phase inside the vials. After analysis of the initial H_2 concentration, samples were incubated at estimated in situ temperatures and H_2 concentration in the gas phase was monitored as a time series. At each time point, 1 mL of gas was sampled with a gas-tight syringe. In order to maintain a constant pressure inside the vials, the withdrawn amount of gas was substituted through an injection of an equal volume of pure N_2 after each analysis (using the bypass gas of the Peak Performer 1, see below). In principle, the time series is supposed to continue until the H_2 concentration reaches a constant level that represents a steady state between H_2 production and consumption. The incubation method allows the determination of dissolved H_2 concentration based on two fundamental assumptions: (a) the analyzed gaseous H_2 in the headspace is in equilibrium with dissolved H_2 in the interstitial water, and (b) the incubation of samples in the laboratory allows the establishment of a steady state between production and consumption of H_2 that is representative of in situ equilibrium.

The incubation method was initially developed for studies of freshwater sediments and microbial cultures (e.g., Lovley and Goodwin, 1988; Hoehler et al., 1998). In contrast to these metabolically active systems, deep marine subsurface sediments host microorganisms that metabolize at very low rates (D'Hondt et al., 2002; Parkes et al., 2005). Therefore, it is questionable whether the required steady state can be reached within an acceptable time frame in the laboratory and if such a steady state would be representative of in situ conditions.

An alternative approach is the complete extraction of dissolved H_2 into a defined H_2-free gas volume, hereafter called the extraction method, as previously used by Novelli et al. (1987) and D'Hondt et al. (2009). In principle, this method is based on the assumption that the initially present H_2 exsolves from the liquid phase and can be captured in the defined headspace volume of a closed vial. Dissolved H_2 concentration is then calculated based on mass balance considerations (see below).

For the extraction method, ~5 cm³ of sediment was sampled immediately after core recovery from the freshly exposed end of a core section. In general, this was the same section that was used for hydrocarbon gas analysis. The sample was extruded into a 17 mL headspace vial, which was immediately filled to the top with a NaCl solution (3.5%), sealed with a soft butyl stopper, and crimp capped. Excess water was

allowed to escape through a hypodermic needle. Analysis was conducted as soon as possible after core recovery and sampling, but when analysis was delayed, samples were stored at 4°C. Prior to analysis, samples were allowed to equilibrate to room temperature. A headspace was created by displacing 5–10 mL of the aqueous phase with an equal volume of H_2-free N_2 (using the bypass gas of the Peak Performer 1, see below). The gas-in needle was removed first, and the liquid-out needle connected to a syringe was allowed to equilibrate the pressure in the vial headspace to atmospheric pressure. The volume offset in the liquid-out syringe was recorded. The vial was vortexed, and dissolved H_2 was allowed to diffuse out of the interstitial water and equilibrate with the headspace for 20 min before H_2 concentration was analyzed in the headspace gas.

Background control is essential for accurate H_2 analysis by the extraction method, and blanks (i.e., vials filled with NaCl solution but without sediment) were analyzed frequently. On average, the reagent blank of the NaCl solution was 0.006 ± 0.007 µM H_2. The reagent blank was subtracted from samples that were extracted with the NaCl solution.

In both methods, dissolved H_2 concentration is determined based on the H_2 concentration in the headspace gas, which was analyzed by gas chromatography with a reducing compound photometer (RCP) using a Peak Performer 1 (PP1) (Peak Laboratories LLC). Samples are injected into a flow of carrier gas and separated on a packed column before they react with a heated bed of mercuric oxide and form mercury vapor that is subsequently detected in a photometer cell. For H_2, the reaction is: $H_2 + HgO_{(solid)} \rightarrow H_2O + Hg_{(vapor)}$. The instrument detection limit, evaluated statistically by a serial dilution of the primary standard with N_2, is ~8 ppb. Here the instrument was operated using a column temperature of 105°C, an RCP bed temperature of 265°C and N_2 as a carrier gas, and calibrated with a 10 ppm H_2 primary standard on a daily basis. Typically, 1 mL of gas sample was injected to thoroughly flush the 0.1 mL sample loop and the tubing between the injection port and the loop.

The incubation and the extraction methods use different approaches to calculate the dissolved H_2 concentration from the analyzed headspace concentration, but for both methods, the first step is to convert the H_2 concentration in the headspace from molar fractions to molar concentration ($[H_2]_g$):

$$[H_2]_g = \chi_{H2} \times P \times R^{-1} \times T^{-1}, \quad (46)$$

where

$[H_2]_g$ = expressed as nmol/L,
χ_{H2} = molar fraction of H_2 in the headspace gas (in ppb, obtained from GC analysis),
P = total gas pressure (in atm) in the headspace, which was atmospheric pressure,
R = universal gas constant, and
T = temperature of the gas phase in Kelvin.

For the incubation method, the concentration of H_2 dissolved in the interstitial water ($[H_2]_{incub}$, expressed in nmol/L) is assumed to be in equilibrium with the gas phase and calculated as:

$$[H_2]_{incub} = \beta \times [H_2]_g, \quad (47)$$

where β is an experimentally determined solubility constant corrected for temperature and salinity (Crozier and Yamamoto, 1974). The value of β is 0.01555 for seawater (salinity = 33.7‰) at 19.3°C.

For the extraction method, the concentration of H_2 dissolved in the interstitial water ($[H_2]_{extract}$, expressed in nmol/L) is determined based on mass balance considerations:

$$[H_2]_{extract} = ([H_2]_g \times V_H + [H_2]_{aq} \times V_{aq}) \times V_s^{-1} \times \phi^{-1}, \quad (48)$$

where

$[H_2]_g$ = calculated using Equation 46,
$[H_2]_{aq}$ = H_2 concentration in the aqueous phase: obtained from Equation 47, substituting $[H_2]_{aq}$ with $[H_2]_{incub}$,
V_H = volume of the headspace,
V_{aq} = volume of the aqueous phase, including the interstitial water and the solution added,
V_s = volume of the sediment sample, and,
ϕ = sediment porosity.

Lithification of sediments hampered the accurate measurement of sampled sediment volumes. Therefore, V_s was obtained based on the individual weights of the dried sediment samples and corresponding data on grain density and porosity from shipboard analysis.

Total carbon, nitrogen, and sulfur contents of the solid phase

In general, solid phase samples for organic geochemistry were taken every 2–3 m downcore. In each core, one sample was associated with a cluster sample for a suite of solid phase analyses. This sample was taken from the whole-round core for interstitial water sampling and adjacent to the headspace samples for gas analysis. After freeze-drying and homogenizing the sample, total carbon, nitrogen, and sulfur concentra-

tions were determined by elemental analysis using a Thermo Finnigan Flash EA 1112 carbon-hydrogen-nitrogen-sulfur (CHNS) analyzer. Calibration was based on the synthetic standard sulfanilamide, which contains 41.81 wt% C, 16.27 wt% N, and 18.62 wt% S. About 20–50 mg of freeze-dried ground sediment was weighed and placed in a tin container for carbon and nitrogen analyses. For sulfur analysis, the same amount of freeze-dried sediment was weighed and put in a tin container with the same amount of a V_2O_5 catalyst. Sediment samples were combusted at 1000°C in a stream of oxygen. Nitrogen oxides were reduced to N_2, and the mixture of CO_2, N_2, and SO_2 was separated by gas chromatography and detected by a thermal conductivity detector (TCD). The standard deviation of carbon, nitrogen, and sulfur concentrations is less than ±0.1%. Accuracy for carbon and sulfur analysis was confirmed using two GSJ reference samples.

Inorganic carbon, organic carbon, and carbonate content of the solid phase

In the same set of samples that was used for the analysis of total carbon, nitrogen, and sulfur contents of the solid phase, inorganic carbon concentration was determined using a Coulometrics 5012 CO_2 coulometer. About 10–20 mg of freeze-dried ground sediment was weighed and reacted with 2M HCl. The liberated CO_2 was titrated, and the change in light transmittance was monitored with a photodetection cell. The weight percentage of calcium carbonate was calculated from the inorganic carbon content, assuming that all the evolved CO_2 was derived from dissolution of calcium carbonate, by the following equation:

$$\mathrm{CaCO_3\ (wt\%)} = \text{inorganic carbon (wt\%)} \times 100/12. \quad (49)$$

No correction was made for the presence of other carbonate minerals. National Institute of Standards and Technology–Standard Reference Material 88b was used to confirm accuracy, which was ±0.2 wt% from the certified value (12–64 wt%) of inorganic carbon content. Total organic carbon (TOC) contents were calculated by subtraction of inorganic carbon from total carbon contents as determined by elemental analysis.

Characterization of the type and maturity of organic matter by Rock-Eval pyrolysis

Rock-Eval pyrolysis was used to characterize the type and maturity of the organic matter in the sediments and to identify its hydrocarbon potential. In principle, Rock-Eval pyrolysis consists of sequentially heating a sample in an inert atmosphere (helium) within a pyrolysis oven. It allows us to quantitatively and selectively determine (1) the free hydrocarbons contained in the sample and (2) the hydrocarbon- and oxygen-containing compounds (CO_2) that are volatilized during the cracking of unextractable organic matter (kerogen) in the sample. In addition, the shipboard instrument, a Rock-Eval6 Standard, can also be used to oxidize and quantify the residual organic carbon (i.e., organic matter remaining after pyrolysis).

Rock-Eval pyrolysis yields the following basic parameters (Pimmel and Claypool, 2001). S_1 is the amount of free hydrocarbons (gas and oil) in the sample (in milligrams of hydrocarbon per gram of sediment). S_2 is the amount of hydrocarbons generated through volatilization of very heavy hydrocarbons compounds ($>C_{40}$) and thermal cracking of nonvolatile organic matter (in milligrams of hydrocarbon per gram of sediment); it is an indication of the quantity of hydrocarbons that the sediment can potentially produce should burial and maturation continue. S_3 is the amount of CO_2 (in milligrams CO_2 per gram of sediment) produced during pyrolysis of kerogen. S_3 is an indication of the amount of oxygen in the kerogen. T_{max} is the temperature at which the maximum release of hydrocarbons from cracking of kerogen occurs during pyrolysis. T_{max} is an indication of the stage of maturation of the organic matter. HI is the hydrogen index (HI = [100 × S_2]/TOC; in milligrams of hydrocarbon per gram of TOC). HI correlates with the ratio of H to C, which is high for lipid- and protein-rich organic matter of marine algae. OI is the oxygen index (OI = [100 × S_3]/TOC; in milligrams CO_2 per gram of TOC). OI is a parameter that correlates with the ratio of O to C, which is high for polysacharride-rich remains of land plants and inert organic material (residual organic matter). PI is the production index (PI = $S_1/[S_1 + S_2]$). PI is used to characterize the evolution level of the organic matter. PC is the pyrolyzable carbon (PC = 0.083 × [S_1 + S_2]). PC corresponds to carbon content of hydrocarbons volatilized and pyrolyzed during the analysis. RC is the residual organic carbon.

During Expedition 322, Rock-Eval analysis was conducted on samples from depth intervals that had been sampled for hydrocarbon gases and dissolved H_2. For analysis, subsamples of ~60 mg dry sediment were obtained from the same freeze-dried and homogenized bulk sample that had been used to determine total carbon, nitrogen, and sulfur contents of the sediment's solid phase. The pyrolysis oven temperature program used the following procedures. For

3 min, the oven was kept at 300°C and the volatilized free hydrocarbons were measured as the S_1 peak (detected by FID). The temperature was then increased from 300° to 550°C (at 25°C/min). The hydrocarbons released from this thermal cracking were measured as the S_2 peak (by FID), and the temperature at which S_2 reached its maximum was recorded as T_{max}. The CO_2 released from kerogen cracking was trapped in the 300°–390°C range. The trap was heated and the released CO_2 was detected as S_3 peak (by TCD). The residual organic matter was oxidized in an oxidation oven kept at 600°C.

Microbiology

Upon extraction from the seafloor, sediment cores begin to equilibrate to surface environmental conditions. Microbes sensitive to changes in temperature, pressure, redox potential, and other environmental parameters can be significantly impacted in their activity, growth, cell structure, and/or cellular composition (cf. Ehrlich and Newman, 2009). Intra- and extracellular biomolecules such as deoxyribonucleic acid, ribonucleic acid (RNA), intact polar lipids, and various enzymes can be altered or damaged such that an accurate assessment of in situ microbial community structure and/or activity is impeded. Furthermore, there exists the potential for introducing nonindigenous microbial and/or biomolecular contamination from the surface environment, an issue of possibly greater relevance for sediments with lower biomass. Thus, careful attention must be paid when possible to time-sensitive and aseptic shipboard handling, processing, and storage of microbiology samples.

Whole-round core sampling and handling

Multiple studies using microbiological, molecular biological, and biogeochemical approaches will be performed on shore using whole-round cores and subsampled sediments. Shipboard protocols were limited to the appropriate sampling, processing, and storage of subseafloor sediment whole-round cores and basalt core fragments. Sample processing was usually completed within 30 min from the time of core recovery on deck, and samples were held at 2°–8°C during most of this period.

Upon receiving sediment cores from the drilling rig to the core cutting area, an interval was selected for adjacently located whole-round core sampling for interstitial water (variable in length depending on expected interstitial water volume recovery), microbiology (15 cm), and organic geochemistry (10 cm) analyses. The sample collocation maximizes the contextual data from adjacent specimens. From Hole C0011B, microbiology whole-round cores were obtained at roughly 50 m intervals. Sampling at higher spatial resolutions (every 10–30 m) was possible for Hole C0012A.

After removal from the core cutting area, the whole-round core (still containing the microbiology whole-round core at this stage) was sent directly to the X-ray CT imaging laboratory where it was either accepted or rejected for interstitial water microbiology/organic geochemistry whole-round core sampling, based on the presence or absence of features important to structural and sedimentological studies. If accepted, this composite whole-round core was taken to the QA/QC laboratory, where 10 and 5 cm long whole-round cores were cut for onshore biomolecular extractions and cultivation/staining/cell counting analyses, respectively. All sediment cores were cut with sterilized cutting tools, and microbiology whole-round cores were quickly covered with end caps that were irradiated for >45 min (at ~60 cm distance) with UV-C light and sealed with plastic tape.

Sealed 10 cm whole-round cores were placed into zip freezer bags for immediate transfer to the shipboard –80°C freezer for the duration of Expedition 322, at which time they were transferred on dry ice to KCC. The 5 cm whole-round cores were brought directly from the QA/QC laboratory into an anaerobic chamber (Coy Laboratory Products) in the adjacent microbiology laboratory and sampled for roughly 5–10 min at 2°–8°C under a 98:2 N_2:H_2 atmosphere for fluorescence in situ hybridization (FISH) studies (see **"Sample processing for cell detection by epifluorescence microscopy"**). The samples were then sealed in their core liners as described above and placed into oxygen-impermeable vinyl bags with inserted AnaeroPack oxygen-removing CO_2-generating paper sachets (Mitsubishi Gas Chemical Co., Inc.). Sealed anaerobic whole-round cores were transferred into storage at 3°–4°C for the duration of Expedition 322 until they could be transferred at 2°–8°C to KCC and/or Expedition 322 microbiology science party home institutions. These whole-round cores will be used for multiple biological studies (e.g., cultivation, activity measurements using stable and radiogenic isotopes, and extracellular enzymes).

When the core was heavily fragmented or the ratio of core recovery to advance was low (<0.3), microbiology whole-round cores were not possible to obtain. For most of these cases, however, small "chips" (≥2 cm^3 in diameter) were obtained from interstitial water whole-round cores that were trimmed of drilling mud contamination in an N_2-flushed glove bag. These chips were washed with sterile RNA-ase (RNA Later) and frozen at –80°C.

Sample processing for cell detection by epifluorescence microscopy

Epifluorescent cell staining and enumeration (Morono et al., 2009), FISH (Amann and Fuchs, 2008), and catalyzed reporter deposition–fluorescence in situ hybridization (CARD-FISH) (Schippers et al., 2005) staining are the primary tools used for species-specific visualization of living microbes. Because intracellular RNA is easily degraded by enzymatic reaction after cell death, it is necessary to fix the cells as soon as possible after core recovery. The 5 cm whole-round core for cultivation and FISH work was placed into a gel ice pack mold preformed to wrap snugly around its circumference and held in place by rubber bands (Fig. **F18**). Whole-round cores were subsampled in their centers using an autoclaved metal coring device tapped gently into the sediment with a small hammer inside the anaerobic chamber. Sediment subcores were ejected into small polypropylene tubes, homogenized manually with a sterile metal spatula, fixed with sterile 2% paraformaldehyde in PBS solution (Invitrogen, pH adjusted to 7.6) for 8–12 h at 3°–4°C, washed by centrifugation/decanting/resuspension 2–3 times with sterile PBS, and finally stored at –20°C in a 10 mL 1:1 mixture of cold PBS:ethanol (99.9% purity). Centrifuge conditions for these washing steps were 9000 × g at 4°C for 10 min.

Routine microbiology samples

As per the STP recommendation 0908-09, Expedition 322 attempted the implementation of routine microbiological sampling for community archival purposes. However, significant inconsistencies in both core recovery and core quality rendered it necessary to relocate multiple planned whole-round core samples for both science party and archival purposes. Prioritization was given to shipboard and shore-based Expedition 322 science party members, and only two dedicated whole-round cores for the IODP community archive could be obtained. Subsamples from these whole-round cores will be deposited at KCC (Masui et al., 2009) into the community archive for postexpedition science requests.

Where dedicated archival whole-round cores could be taken from recovered cores, they were taken adjacent to interstitial water whole-round cores. Although the STP recommendation mentions only the shipboard storage of archival whole-round cores at –80°C, we attempted to expediently subsample these for future FISH-based studies. The purpose of this implementation was to review the feasibility of sample processing as a routine task for the onboard microbiologist and investigate the temporal change in the quality of preserved samples. FISH subsamples from archival whole-round cores were taken as described above.

Evaluation of potential contamination

As a control sample for contamination, freshly prepared drilling mud (seawater gel) was obtained during Expedition 322. Seawater gel is a seawater-base bentonite mud (pH 12.3) used for drilling and coring throughout the entire section and contains 0.5 m^3 seawater, 0.5 m^3 drill water, 60.0 kg bentonite, 2.0 kg caustic soda, and 2.0 kg lime. The density of this drilling mud is 1.05 g/cm^3. Subsamples of the seawater gel were stored at 4° and –80°C for culturing and molecular analysis, respectively. Also, natural chemical tracers such as sulfate in interstitial water were measured (see **"Inorganic geochemistry"**). Because of drilling constraints, we were not able to perform other conventional tracer tests such as monitoring the infiltration of micrometer-sized fluorescent spheres or perfluorocarbon tracer (Smith et al., 2000).

Downhole measurements

Direct measurements of in situ pressure and temperature are critical to defining transport, diagenesis, and microbial activity in marine sediments. These data can be used to evaluate heat flux, fluid flow, and chemical transport through the system. Additionally, the data are valuable for validating shipboard and shore-based estimates of pressure and stress from consolidation experiments or interpreting porosity-depth data. The pressure and temperature fields also impact the strength behavior of sediments and therefore can be used to evaluate conditions that promote or impede fault slip.

In situ pressure and temperature measurements

During Expedition 322, a test deployment of the sediment temperature-pressure (SET-P) tool was used to evaluate deployment procedures and sensor calibrations. No in situ temperature and pressure measurements were made in the formation because of difficulties locating suitable target intervals of unlithified sand at Site C0011 (see **"Downhole measurements"** in the "Site C0011" chapter).

The SET-P tool incorporates a single thermistor in an oil-filled tip and ports that allow hydraulic transmission of formation pressure to an internal pressure gauge. A standard data logger records the pressure and temperature data. The temperature sensor in the SET-P tool operates over a range of 0°–85°C with a resolution of 0.001°C. The pressure sensor has a sen-

sitivity of 70 Pa over a range of 0–70 MPa. All pressures and temperatures are recorded at 1 Hz. The SET-P tool also includes a three-component accelerometer. All accelerometer data are recorded at 10 Hz.

A typical SET-P deployment consists of connecting the SET-P tool to the colleted delivery system (CDS), lowering the tool string by wireline ~1000 m, and then taking a 30 s calibration measurement. The tool is lowered another 1000 m and a second 30 s calibration point is measured. The tool is then lowered to the seafloor for a 5 min calibration point. The drill bit is then raised ~2 m off the bottom of the hole. Subsequently, the tool string is lowered until the CDS engages in the bottom-hole assembly (BHA), with the tip of the tool extending 1.1 m below the drill bit. The SET-P tool is pushed into the sediment by lowering the drill bit to the bottom of the hole. Pressure and temperature are recorded for >30 min. No fluids are circulated during data collection at the calibration points or when the tool is in the sediment. The tool string is then recovered via wireline. During the Expedition 322 test run, only the 30 s calibration tests in the water column were completed; the SET-P tool was not advanced into the formation.

Logging and core-log-seismic integration

Logging tools are used to determine physical, chemical, and structural properties of formations penetrated by drilling. Data are collected rapidly, continuously with depth, and, most importantly, measured in situ. Logs may be interpreted in terms of the stratigraphy, lithology, mineralogy, and geochemical composition of the penetrated formation. Where core recovery is good, logging and core data are complementary and should be integrated and interpreted jointly, with logging data providing the in situ ground truth for core data. Where core recovery is incomplete or disturbed, logging data may provide a reliable means to characterize the borehole section.

Downhole logs record formation properties on a scale that is intermediate between those obtained from core samples and from geophysical surveys. Logging data are therefore complementary to centimeter-scale core studies, as well as seismic reflection images with a resolution of tens of meters scale. Logs provide measurements of in situ properties at a depth of investigation into the formation that varies depending on the tool. The logs are critical for calibrating geophysical survey data (e.g., through synthetic seismograms), providing the necessary link for integration between the core depth domain and the seismic time domain.

Two types of logging methods were attempted in support of Expedition 322: LWD and wireline logging. LWD data were acquired in Hole C0011A during Expedition 319, whereas wireline logging was planned for Expedition 322 at primary Site C0011 and contingency Site C0012. For the core-log-seismic integration (CLSI), we used VCDs, discrete sample measurements (e.g., *P*-wave velocity and density; see **"Physical properties"**), continuous multisensor core logger (MSCL) measurements, logging data, and prestack depth–migrated seismic data.

Logging while drilling

During Expedition 319, LWD and measurement while drilling (MWD) were conducted in riserless Hole C0011A (Expedition 319 Scientists, 2010). Figure **F19A** shows the configuration of the LWD/MWD BHA. MWD and selected LWD real-time measurements were transmitted through the drilling fluid by means of a modulated pressure wave (mud pulsing or fluid pulse telemetry) at a rate of 6 bits per second and monitored in real time. All LWD data were recorded into downhole memory and retrieved when the tools reached the surface. MWD measurements included ROP, downhole torque, inclination/orientation, weight on bit (WOB), NGR emissions, and annular pressure while drilling. During drilling operations, these measurements were combined with surface rig floor parameters for drilling monitoring (e.g., WOB, torque, etc.) and quality control.

LWD logging tool: geoVISION

During LWD operations, Schlumberger's geoVISION tool (Fig. **F19B**) was run, with the mud pulse system transmitting a limited set of data to the surface in real time. The geoVISION resistivity tool is based on resistivity-at-the-bit (RAB) technology. It provides resistivity measurements and electrical images of the borehole wall similar to the wireline Formation MicroScanner (FMS) but with complete coverage of the borehole wall and lower vertical/horizontal resolution. In addition, the RAB tool contains a scintillation counter that provides a total gamma ray measurement. The geoVISION tool is connected directly above the drill bit and uses the lower portion of the tool and the bit as a measuring electrode. A 1.5 inch (3.8 cm) electrode located 136 cm from the bottom of the tool provides a focused lateral resistivity measurement (ring resistivity) with a vertical resolution of 2–3 inches (5–7.6 cm) and a depth of investigation of ~7 inches (17.8 cm). In addition, button electrodes provide shallow-, medium-, and deep-focused resistivity measurements, as well as azimuthally orientated images. The azimuthal resistivity measurements are acquired with a ~7° resolution

as the geoVISION tool rotates. The button electrodes are ~1 inch (2.5 cm) in diameter and reside on a clamp-on sleeve. The buttons are longitudinally spaced along the geoVISION tool to render staggered depths of investigation of ~1, 3, and 5 inches (2.5, 7.6, and 12.7 cm). This spacing provides multiple depths of investigation for quantifying invasion profiles and fracture identification (drilling induced versus natural). Resolution and depth of investigation for each resistivity measurement are shown in Table **T14.** For environmental correction of the resistivity measurements, drilling fluid resistivity and temperature were also measured (Schlumberger, 1989).

The tool's orientation system uses Earth's magnetic field as a reference to determine the tool position with respect to the borehole as the drill string rotates, thus allowing both azimuthal resistivity and natural gamma radiation measurements. The gamma ray sensor has a range of operability of 0–250 gAPI, an accuracy of ±7%, and a statistical resolution of ±3 gAPI at 100 gAPI and an ROP of 30 m/h. Its vertical resolution is 1.5 inches.

Once obtained, resistivity and gamma ray data were processed onboard *Chikyu*, using Schlumberger's software GeoFrame, GeoMechanics International, Inc.'s GMI Imager, and Paradigm, Ltd.'s software Geolog for further analysis and interpretation.

Wireline logging

During Expedition 322, wireline logging was planned for Sites C0011 and C0012. Our initial wireline logging plan consisted of four primary tool strings:

1. High-Resolution Laterolog Array (HRLA) tool for laterolog resistivity; NGR tool; and dummy tools with dimensions and weight that match the tools in the following runs to ensure the safety of operation with radioactive sources;
2. Hostile Environment Litho-Density Sonde (HLDS) for density, photoelectric factor (PEF), and caliper; Highly Integrated Gamma Ray Neutron Sonde (HGNS) for neutron porosity and NGR; and Hostile Environment Natural Gamma Ray Sonde (HNGS) for spectroscopy gamma ray;
3. FMS for resistivity imaging, Sonic Scanner for sonic velocity (*P*- and *S*-wave velocities), and NGR tool; and
4. Versatile Seismic Imager (VSI) for seismic velocity by check shot.

Vertical resolution and depth of investigation for each tool are shown in Table **T15.** However, slow ROP and degradation of the drill bit at Hole C0011B resulted in the postponement of the logging plan until Site C0012. Unfortunately, because of difficult hole conditions and expiration of time-on-site in advance of a typhoon evacuation at Hole C0012A, we were limited to one attempt at logging with a single tool string, composed of HRLA and FMS. After several unsuccessful attempts to pass a difficult spot just 10 m below pipe depth, all logging operations were canceled, with no usable data.

Wireline logging tools

Wireline logging data are typically recorded and stored digitally and monitored in real time using Schlumberger's Multitask Acquisition Imaging System (MAXIS) 500 (Fig. **F20**). Onboard logging processing includes (1) depth shifting all logs relative to a common datum (e.g., the seafloor), (2) corrections specific to individual tools, and (3) quality control. FMS image data are usually processed onboard *Chikyu* using Schlumberger's GeoFrame (version 4.3) software package and imported into GMI Imager software for further analysis. The processing steps include conversion of data format, inclinometry quality check, equalization, resistivity calibration, and normalization.

High-Resolution Laterolog Array tool

The HRLA tool combines various electrodes to provide five independent, actively focused, depth- and resolution-matched measurements to resolve true formation resistivity (R_t) in thinly bedded and deeply invaded formations in addition to a shallowest mode (Mode 0) for mud resistivity. Modes 1 to 5 have increasing depths of investigation. The supplementary mode helps improve the mud invasion profile and correct the raw resistivity data to retrieve the true formation resistivity. It is less affected by shoulder beds than traditional laterolog measurements because of the active focusing and multifrequency operation, together with the symmetric tool design. In addition, the tool employs software focusing to improve the accuracy of true resistivity estimates through advanced 2-D inversion processing.

Highly Integrated Gamma Ray Neutron Sonde

Neutrons interact differently with matter depending on their energy. Fast neutrons (E > 10 keV) are scattered elastically, primarily by H atoms. They can also induce inelastic scattering, in which case the excited atoms release gamma rays. If the neutron energy becomes small enough (thermal neutron, E < 0.1 eV), they can be absorbed by the medium by thermal capture. The most efficient absorbers are Cl, B, and H. Thermal capture also releases gamma rays. The HGNS tool contains an Am-Be radioactive source that bombards the formation with fast neutrons (>10 keV). These neutrons are slowed by scattering

and then captured. Epithermal neutron detectors quantify elastic scattering, and thus the H index and a porosity estimate are generated. Gamma ray detectors and thermal neutron detectors document the thermal capture. The measurement by the HGNS sensor is dependent on hydrogen content, and hence water content. We note that most clay-rich rocks contain some intracrystalline water. The measured value is also affected by water-based mud; therefore, the data are corrected with mud properties.

Hostile Environment Natural Gamma Ray Sonde

^{40}K and isotopes of the decay chains of radioactive isotopes of Th and U emit photons at different energies. The HNGS tool uses spectroscopic analysis to determine the concentration of radioactive ^{40}K (in weight percent), Th (in ppm), and U (in ppm). The HNGS tool also measures U-free gamma ray emissions (in gAPI, also called computed gamma ray emissions). The HNGS uses two bismuth germanate scintillators for gamma ray detection. The tool response is affected by the tool standoff (distance between the sensor and the borehole wall) and the weight and concentration of bentonite or KCl in the drilling mud (KCl may be added to the drilling mud to prevent hydrous clays from swelling and obstructing the well). Spectral analysis filters out gamma ray energy below 500 keV to reduce sensitivity to bentonite and KCl in the drilling mud and to improve measurement accuracy. Environmental corrections are usually made during data processing. This tool has a 24 cm depth of investigation.

Hostile Environment Litho-Density Sonde

The HLDS measures formation density using a radioactive ^{137}Cs gamma ray source (662 keV) and far and near gamma ray detectors mounted on a shielded skid that is pressed against the borehole wall. Gamma rays emitted by the source experience both Compton scattering and photoelectric absorption. Compton scattering involves the ricochet of gamma rays off electrons in the formation via elastic collision, transferring energy to the electron in the process. The number of scattered gamma rays that reach the detectors is related to the number of electrons in the formation, which is a function of the bulk density. Porosity can also be derived from this bulk density if the matrix (grain) density is known from MAD measurements on cores. The HLDS also measures photoelectric absorption of the gamma rays (PEF), which occurs when they drop to <150 keV after being repeatedly scattered by electrons in the formation. PEF varies according to the chemical composition of the formation (Gardener and Dumanoir, 1980). Some examples of PEF values are pure pyrite = 16.97 b/e$^-$, calcite = 5.08 b/e$^-$, illite = 3.03 b/e$^-$, quartz = 1.81 b/e$^-$, and kaolinite = 1.49 b/e$^-$. Good contact between the tool and borehole wall is essential for acquisition of high-quality HLDS logs. Poor contact results in an underestimation of density values. Both density correction and caliper measurement of the hole are used to check the contact quality.

Formation MicroScanner

The FMS provides high-resolution resistivity images of the borehole wall (~25% of a 25 cm diameter borehole can be imaged on each pass). The tool has four orthogonal arms with pads, each containing 16 button electrodes that are pressed against the borehole wall during recording. The electrodes are arranged in two diagonally offset rows of eight electrodes. A focused current is emitted from the button electrodes into the formation with a return electrode located near the top of the tool. The intensity of the current passing through the button electrodes is measured. The maximum extension of the caliper arms is 15 inches; therefore, in holes or sections of holes with a larger diameter, pad contact will be inconsistent and the FMS images may appear out of focus and too conductive. Irregular borehole walls will also adversely affect the image quality if they lead to poor pad/wall contact. Processing transforms these measurements, which reflect the microresistivity variations of the formation, into continuous, spatially oriented, high-resolution images that map the geologic structures of the borehole wall. The depth of investigation is ~2.5 cm, and the electrode buttons produce images with a vertical resolution of 5 mm. The quality of the image enables assessment of rock composition and texture, detailed structure (e.g., bedding and fracturing), and fluid content. Local contrasts in FMS images were improved by applying a dynamic normalization to the FMS data. The General Purpose Inclinometry Tool (GPIT) accompanies the FMS and integrates both a three-axis accelerometer and a three-axis magnetometer to determine the orientation and inclination of the tool string during logging. This provides a means of correcting the FMS images for rotation and irregular vertical tool motion, allowing the true dip and direction (azimuth) of structures to be determined. It can also provide the geometry of the borehole path. We planned to use a slim FMS during Expedition 322.

Sonic Scanner

The Sonic Scanner is a new generation acoustic measurement tool and is a successor of the Dipole Sonic Imager (DSI). In addition to axial and azimuthal measurements, the Sonic Scanner makes a radial measurement to probe the formation for near- and far-

field slowness. The depth sensitivity is equal to two to three times the borehole diameter. Other attributes of the Sonic Scanner include: (1) a wide-frequency spectrum ranging from 300 Hz to 9 kHz, (2) a longer azimuthal array (five more receiver stations, 2 ft longer than the DSI), (3) a borehole-compensated monopole with long (11–17 ft) and short (1–7 ft) spacing, and (4) cross-dipole acquisition. The Sonic Scanner provides accurate radial and axial measurements of stress-dependent properties near the borehole. These data are converted into: (1) *P*- and *S*-wave velocities, (2) anisotropy of propagation, (3) Stoneley wave velocity, and (4) cement bond quality.

The Sonic Scanner receiver configuration produces a long azimuthal array (i.e., 8 azimuthal receivers at each of the 13 stations). With the two near-monopole transmitters straddling this array and a third transmitter beyond, the short- to long-monopole transmitter-to-receiver spacing combination provides a radial monopole profile.

Versatile Seismic Imager

The VSI is an array of seismometers clamped to the borehole wall to receive seismic waves from an air gun. The VSI produces data that can be interpreted as a check shot survey, a low-resolution velocity-depth function, and a vertical seismic profile. The VSI records seismograms using a three-component geophone in the tool and a surface source and hydrophone. The source was a trio of 250 in^3 G-guns to be suspended from Crane 1 ~60 m horizontally from the rotary table and fired at 1700–2000 psi at 6 meters below sea level (mbsl) (e.g., Expedition 314 Scientists, 2009). Time correlations of the shots are ensured with high-precision clocks at both the surface hydrophone and the downhole hydrophones. The surface hydrophone was to be suspended 5 m below the air guns (total of 11 m below mean sea level), and the zero times of the waveforms corrected to mean sea level. At each data acquisition level, a number of shots were to be fired by the surface source. The tool records the acceleration seismograms obtained for each shot.

Logging data quality

Logging data quality may be seriously degraded by changes in hole diameter in sections where the borehole diameter greatly decreases or is washed out. Nuclear measurements (density and neutron porosity) are more sensitive to borehole conditions because of their shallower depths of investigation and the effect of drilling fluid volume on neutron and gamma ray attenuation. Corrections can be applied to the original data to reduce some of these effects, but for very large washouts, data cannot be corrected.

Azimuthal measurements and associated images (RAB and FMS images) are of low quality when the measuring tool is not rotating ("stick") or when its rotation exceeds 250 rotations per minute (rpm) ("slip"). In zones of high stick-slip, tool rotation can vary greatly locally, resulting in images of lower quality. As all measurements by the same tool are not necessarily sampled at the same time, improper heave compensation and irregular movement of the BHA can result in local depth shifts between measurements by several tens of centimeters.

LWD/MWD data quality is mostly assessed by cross-correlating available logs of two types: drilling control parameters (e.g., ROP and stick-slip indicator) and geophysical control logs (e.g., gamma ray). Time-depth relationships are considered, to identify the sequence of drilling events and to further assess their possible impact on data quality. Then operational surface data and downhole data are compared for a detailed assessment of drilling conditions on log quality.

Natural gamma ray logs from the Enhanced Digital Telemetry Cartridge (EDTC), HGNS, and HNGS provide a means of depth correlation between logging runs. Logs from different tool strings may, however, still have minor depth mismatches caused either by cable stretch or ship heave during recording.

Log characterization and interpretation

LWD and wireline measurements provide in situ petrophysical information on sediments, rocks, and interstitial water while the hole is being drilled, or shortly thereafter in the case of wireline logging. These measurements are sensitive to changes in composition (changing curve magnitudes), textures, and structures (log shape, peak amplitude, and frequency, as well as information from log images). Changes in the log response (values and/or frequency of the signal) are commonly associated with lithologic unit boundaries.

The characterization of logging data, including LWD and wireline logging measurements, as well as imaging tool response, allows the borehole to be zoned into distinct logging units. Once representative petrophysical properties for the logging units were defined, they were incorporated into the log-based lithologic units. For Site C0011, the aim was to provide a preliminary assessment of expected lithologies from LWD data prior to coring and to provide more detailed properties from wireline logging after coring. At Site C0012, where logging was to follow coring operations, the goal was to refine unit boundaries (where core recovery or quality was lacking) and to provide a basis for comparison with Site C0011. However, since wireline logging data were not col-

lected during this expedition, we will not address the details of wireline data analysis here.

LWD data analysis

During Expedition 322, initial log-based lithologies at Site C0011 were interpreted using only the LWD logs obtained during Expedition 319. Following log characterization and classification, logs were lithologically and geologically interpreted using a combination of log characteristics and borehole images.

Compositionally influenced logs, such as gamma ray logs from the geoVISION tool, were used to predict lithology from unit scale (hundreds of meters) to bed scale (centimeters to meters). In particular, the identification of probable sand-rich intervals, clay-rich intervals, and alternating beds of sand and clay was a primary element of the interpretation. Borehole images provided useful information on mesoscopic features such as sedimentary structures (e.g., slumps), bed boundaries, angular unconformities, fractures, and faults. The orientation of breakouts, or borehole enlargements, was also mapped, as the direction of enlargement can be related to the direction of maximum horizontal stress within the formation. Additionally, lithologic descriptions from ODP Legs 131, 190, and 196, in the Nankai Trough off Shikoku Island, were an important aid in interpreting lithology (Taira, Hill, Firth, et al., 1991; Moore, Taira, Klaus, et al., 2001; Mikada, Becker, Moore, Klaus, et al., 2002).

Electrical resistivity images

Structural analysis from logging data was performed on the geoVISION images using GMI Imager (GeoMechanics International, Inc.) and GeoFrame (Schlumberger) software. These software packages present resistivity image data of the borehole wall as planar "unwrapped" 360° images with depth. The software also allows visualization of the data in a 3-D borehole view.

Resistivity image data were displayed as both statically and dynamically normalized images. Static normalization displays the image with a color range covering all resistivity values for the entire logged interval; this highlights relative changes in resistivity throughout the borehole and is useful for identifying lithologic or facies changes. Dynamic normalization scales the color range for resistivity values over a constant depth interval (1 m) and is commonly used for detailed identification of fractures and structures that are more subtle changes.

In unwrapped resistivity images, sinusoidal lines are planar surfaces, while curved lines are nonplanar surfaces. Features were classified according to type, to distinguish between fractures, bedding planes, faults, and borehole breakouts. We compared initial image interpretations from the logging data with structural data from cores and seismic reflection data as a check on the validity of our interpretations.

Core-Log-Seismic integration

During Expedition 322, we used LWD data to establish ties between data from cores (continuous and discrete samples) and the seismic data set (Park et al., 2008). Table **T16** shows planned measurements and observations for CLSI during Expedition 322.

Log-seismic integration

Using the available density and *P*-wave velocity data from discrete core samples, we were able to create a reflection coefficient series for Site C0011. This series was then convolved with the extracted source wavelet to generate a synthetic seismogram. Displaying the synthetic seismogram beside the seismic data in the vicinity of the borehole provides information about specific boundaries of interest and provides a quality check on velocity and density logs.

Core-log integration

Integration of cores with log data relies primarily on NGR data from the MSCL, as well as lithologic characteristics identified in photos, X-ray CT scans, smear slides, discrete sample measurements, VCDs, and so on. NGR data were used for correlation between the cores and the logs and to conduct necessary depth-shifting to correctly place sections of core or account for core expansion. In particular, LWD data (NGR, resistivity, and resistivity images) were useful for core-log integration at Site C0011.

Core-log-seismic integration

In order to correlate log-seismic integration results with core-log integration results, we used seismic reflection traces at Site C0011 and a synthetic seismogram as key inputs. Detailed CLSI enables us to infer lateral variations of physical properties along the seismic reflection profile and to interpret the seismic data in terms of the measured formation properties. Before expanding those physical properties into 2-D or 3-D, careful identification of continuous, high-amplitude reflectors on seismic profiles, which are key packages of beds or horizons, is essential.

References

Aguirre, E., and Pasini, G., 1985. The Pliocene–Pleistocene boundary. *Episodes,* 8:11–120.

Amann, R.I., and Fuchs, B.M., 2008. Single-cell identification in microbial communities by improved fluores-

cence in situ hybridization techniques. *Nat. Rev. Microbiol.,* 6(5):339–348. **doi:10.1038/nrmicro1888**

ASTM International, 1990. Standard method for laboratory determination of water (moisture) content of soil and rock (Standard D2216–90). In *Annual Book of ASTM Standards for Soil and Rock* (Vol. 04.08): Philadelphia (Am. Soc. Testing and Mater.). [revision of D2216-63, D2216-80]

Blow, W.H., 1969. Late middle Eocene to Recent planktonic foraminiferal biostratigraphy. *Proc. Int. Conf. Planktonic Microfossils,* 1:199–422.

Blum, P., 1997. Physical properties handbook: a guide to the shipboard measurement of physical properties of deep-sea cores. *ODP Tech. Note,* 26. **doi:10.2973/odp.tn.26.1997**

Carlson, R.L., and Christensen, N.I., 1977. Velocity anisotropy and physical properties of deep-sea sediments from the western South Atlantic. *In* Supko, P.R., Perch-Nielsen, K., et al., *Init. Repts. DSDP,* 39: Washington, DC (U.S. Govt. Printing Office), 555–559. **doi:10.2973/dsdp.proc.39.124.1977**

Cline, J.D., 1969. Sectrophotometric determination of hydrogen sulfide in natural waters. *Limnol. Oceanogr.,* 14(3):454–458. **doi:10.4319/lo.1969.14.3.0454**

Crozier, T.E., and Yamamoto, S., 1974. Solubility of hydrogen in water, sea water, and sodium chloride solutions. *J. Chem. Eng. Data,* 19(3):242–244. **doi:10.1021/je60062a007**

D'Hondt, S., Rutherford, S., and Spivack., A.J., 2002. Metabolic activity of the subsurface life in deep-sea sediments. *Science,* 295(5562):2067–2070. **doi:10.1126/science.1064878**

D'Hondt, S., Spivack, A.J., Pockalny, R., Ferdelman, T.G., Fischer, J.P., Kallmeyer, J., Abrams, L.J., Smith, D.C., Graham, D., Hasiuk, F., Schrum, H., and Stancine, A.M., 2009. Subseafloor sedimentary life in the South Pacific Gyre. *Proc. Natl. Acad. Sci. U. S. A.*, 106(28):11651–11656. **doi:10.1073/pnas.0811793106**

Droser, M.L., and Bottjer, D.J., 1986. A semiquantitative field classification of ichnofabric. *J. Sediment. Petrol.,* 56:558–559.

Droser, M.L., and Bottjer, D.J., 1991. Trace fossils and ichnofabric in Leg 119 cores. *In* Barron, J., Larsen, B., et al., *Proc. ODP, Sci. Results,* 119: College Station, TX (Ocean Drilling Program), 635–641. **doi:10.2973/odp.proc.sr.119.206.1991**

Dunham, R.J., 1962. Classification of carbonate rocks according to depositional texture. *In* Ham, W.E. (Ed.), *Classification of Carbonate Rocks.* AAPG Mem., 1:108–121.

Ehrlich, H.L., and Newman, D.K., 2009. *Geomicrobiology, Fifth Edition:* Boca Raton (CRC Press).

Embry, A.F., III, and Klovan, J.E., 1972. Absolute water depth limits of late Devonian paleoecological zones. *Geol. Rundsch.,* 61(2):672–686. **doi:10.1007/BF01896340**

Expedition 314 Scientists, 2009. Expedition 314 methods. *In* Kinoshita, M., Tobin, H., Ashi, J., Kimura, G., Lallemant, S., Screaton, E.J., Curewitz, D., Masago, H., Moe, K.T., and the Expedition 314/315/316 Scientists, *Proc. IODP,* 314/315/316: Washington, DC (Integrated Ocean Drilling Program Management International, Inc.). **doi:10.2204/iodp.proc.314315316.112.2009**

Expedition 315 Scientists, 2009. Expedition 315 methods. *In* Kinoshita, M., Tobin, H., Ashi, J., Kimura, G., Lallemant, S., Screaton, E.J., Curewitz, D., Masago, H., Moe, K.T., and the Expedition 314/315/316 Scientists, *Proc. IODP,* 314/315/316: Washington, DC (Integrated Ocean Drilling Program Management International, Inc.). **doi:10.2204/iodp.proc.314315316.122.2009**

Expedition 316 Scientists, 2009. Expedition 316 methods. *In* Kinoshita, M., Tobin, H., Ashi, J., Kimura, G., Lallemant, S., Screaton, E.J., Curewitz, D., Masago, H., Moe, K.T., and the Expedition 314/315/316 Scientists, *Proc. IODP,* 314/315/316: Washington, DC (Integrated Ocean Drilling Program Management International, Inc.). **doi:10.2204/iodp.proc.314315316.132.2009**

Expedition 319 Scientists, 2010. Methods. *In* Saffer, D., McNeill, L., Byrne, T., Araki, E., Toczko, S., Eguchi, N., Takahashi, K., and the Expedition 319 Scientists, *Proc. IODP,* 319: Tokyo (Integrated Ocean Drilling Program Management International, Inc.). **doi:10.2204/iodp.proc.319.102.2010**

Fisher, A.T., and Underwood, M.B., 1995. Calibration of an X-ray diffraction method to determine relative mineral abundances in bulk powders using matrix singular value decomposition: a test from the Barbados accretionary complex. *In* Shipley, T.H., Ogawa, Y., Blum, P., et al., *Proc. ODP, Init. Repts.,* 156: College Station, TX (Ocean Drilling Program), 29–37. **doi:10.2973/odp.proc.ir.156.103.1995**

Fisher, R.V., and Schmincke, H.-U., 1984. *Pyroclastic Rocks:* New York (Springer-Verlag).

Fuller, M., 1969. Magnetic orientation of borehole cores. *Geophysics,* 34(5):772–774.

Gardener, J.S., and Dumanoir, J.L., 1980. Litho-density log interpretation. *Trans. SPWLA Annu. Logging Symp.,* 21:1–23.

GE Healthcare, 2006. *LightSpeed Series Learning and Reference Guide-Multi Slice CT:* Waukesha, Wisconsin (GE Healthcare), 936.

Gieskes, J.M., Gamo, T., and Brumsack, H., 1991. Chemical methods for interstitial water analysis aboard *JOIDES Resolution. ODP Tech. Note,* 15. **doi:10.2973/odp.tn.15.1991**

Hanken, N.-M., 1979. The use of sodium tetraphenylborate and sodium chloride in the extraction of fossils from shales. *J. Paleontol.,* 53(3):738–741.

Heard, T.G., and Pickering, K.T., 2008. Trace fossils as diagnostic indicators of deep-marine environments, middle Eocene Ainsa-Jaca Basin, Spanish Pyrenees. *Sedimentology,* 55(4):809–844. **doi:10.1111/j.1365-3091.2007.00922.x**

Hilgen, F.J., 2008, Recent progress in the standardization and calibration of the Cenozoic time scale. *Newsl.*

Stratigr., 43(1):15–22. **doi:10.1127/0078-0421/2008/0043-0015**

Hoehler, T.M., Alperin, M.J., Albert, D.B., and Martens, C.S., 1998. Thermodynamic control on hydrogen concentrations in anoxic sediments. *Geochim. Cosmochim. Acta,* 62(10):1745–1756. **doi:10.1016/S0016-7037(98)00106-9**

Kimura, G., Silver, E.A., Blum, P., et al., 1997. *Proc. ODP, Init. Repts.,* 170: College Station, TX (Ocean Drilling Program). **doi:10.2973/odp.proc.ir.170.1997**

Kirschvink, J.L., 1980. The least-squares line and plane and the analysis of palaeomagnetic data. *Geophys. J. R. Astron. Soc.,* 62(3):699–718. **doi:10.1111/j.1365-246X.1980.tb02601.x**

Kodama, K.P., 1984. Palaeomagnetism of granitic intrusives from the Precambrian basement under eastern Kansas: orienting drill cores using secondary magnetization components. *Geophys. J. R. Astron. Soc.,* 76(2):273–287. **doi:10.1111/j.1365-246X.1984.tb05045.x**

Li, B., Jian, Z., Li, Q., Tian, J., and Wang, P., 2005. Paleoceanography of the South China Sea since the middle Miocene: evidence from planktonic foraminifera. *In* Wang, P., and Lipps, J. (Eds.), *Marine Micropaleontology of the South China Sea*. Mar. Micropaleontol., 54(1–2):49–62. **doi:10.1016/j.marmicro.2004.09.003**

Lourens, L.J., Hilgen, F.J., Shackleton, N.J., Laskar, J., and Wilson, D., 2004. The Neogene period. *In* Gradstein, F.M., Ogg, J.G., and Smith, A.G. (Eds.), *A Geological Time Scale 2004*. Cambridge (Cambridge Univ. Press), 409–440.

Lovley, D.R., and Goodwin, S., 1988. Hydrogen concentrations as an indicator of the predominant terminal electron-accepting reactions in aquatic sediments. *Geochim. Cosmochim. Acta,* 52(12):2992–3003. **doi:10.1016/0016-7037(88)90163-9**

Manheim, F.T., 1966. A hydraulic squeezer for obtaining interstitial waters from consolidated and unconsolidated sediments. *Geol. Surv. Prof. Pap. (U.S.),* 550-C:256–261.

Martini, E., 1971. Standard Tertiary and Quaternary calcareous nannoplankton zonation. *Proc. Int. Conf. Planktonic Microfossils,* 2:739–785.

Masui, N., Morono, Y., and Inagaki, F., 2009. Bio-archive core storage and subsampling procedure for subseafloor molecular biological research. *Sci. Drill.,* 8:35–37. **doi:10.2204/iodp.sd.8.05.2009**

Mazzullo, J., and Graham, A.G. (Eds.), 1988. Handbook for shipboard sedimentologists. *ODP Tech. Note,* 8. **doi:10.2973/odp.tn.8.1988**

Mazzullo, J.M., Meyer, A., and Kidd, R.B., 1988. New sediment classification scheme for the Ocean Drilling Program. *In* Mazzullo, J.M., and Graham, A.G. (Eds.), *Handbook for shipboard sedimentologists*. ODP Tech. Note, 8:45–67. **doi:10.2973/odp.tn.8.1988**

McKenzie, W.S., Donaldson, C.H., and Guilford, C., 1982. *Atlas of Igneous Rocks and Their Textures:* New York (Wiley.)

Mees, F., Swennen, R., Van Geet, M., and Jacobs, P., 2003. Applications of X-ray computed tomography in the geosciences. *Geol. Soc. Spec. Publ.,* 215(1):1–6. **doi:10.1144/GSL.SP.2003.215.01.01**

Mikada, H., Becker, K., Moore, J.C., Klaus, A., et al., 2002. *Proc. ODP, Init. Repts.,* 196: College Station, TX (Ocean Drilling Program). **doi:10.2973/odp.proc.ir.196.2002**

Mizutani, S., Saito, Y., and Kanmera, K. (Eds.), 1987. *Sedimentary Rocks in Japan:* Tokyo (Iwanami Shoten). (in Japanese)

Moore, G.F., Taira, A., Klaus, A., et al., 2001. *Proc. ODP, Init. Repts.,* 190: College Station, TX (Ocean Drilling Program). **doi:10.2973/odp.proc.ir.190.2001**

Morono, Y., Terada, T., Masui, N., and Inagaki, F., 2009. Discriminative detection and enumeration of microbial life in marine subsurface sediments. *ISME J.,* 3(5):503–511. **doi:10.1038/ismej.2009.1**

Motoyama, I., Niitsuma, N., Maruyama, T., Hayashi, H., Kamikuri, S., Shiono, M., Kanamatsu, T., Aoki, K., Morishita, C., Hagino, K., Nishi, H., and Oda, M., 2004. Middle Miocene to Pleistocene magneto-biostratigraphy of ODP Sites 1150 and 1151, northwest Pacific: sedimentation rate and updated regional geological timescale. *Isl. Arc,* 13(1):289–305. **doi:10.1111/j.1440-1738.2003.00426.x**

Nakano, T., Nakashima, Y., Nakamura, K., and Ikeda, S., 2000. Observation and analysis of internal structure of rock using X-ray CT. *Chishitsugaku Zasshi,* 106(5):363–378.

Novelli, P.C., Scranton, M.I., and Michener, R.H., 1987. Hydrogen distributions in marine sediments. *Limnol. Oceanogr.,* 32(3):565–576. **doi:10.4319/lo.1987.32.3.0565**

Okada, H., and Bukry, D., 1980. Supplementary modification and introduction of code numbers to the low-latitude coccolith biostratigraphic zonation (Bukry, 1973; 1975). *Mar. Micropaleontol.,* 5:321–325. **doi:10.1016/0377-8398(80)90016-X**

Park, J.-O., Tsuru, T., No, T., Takizawa, K., Sato, S., and Kaneda, Y., 2008. High-resolution 3D seismic reflection survey and prestack depth imaging in the Nankai Trough off southeast Kii Peninsula. *Butsuri Tansa,* 61:231–241. (in Japanese, with abstract in English)

Parkes, R.J., Webster, G., Cragg, B.A., Weightman, A.J., Newberry, C.J., Ferdelman, T.G., Kallmeyer, J., Jørgensen, B.B., Aiello, I.W., and Fry, J.C., 2005. Deep sub-seafloor prokaryotes stimulated at interfaces over geological time. *Nature (London, U. K.),* 436(7049):390–394. **doi:10.1038/nature03796**

Perch-Nielsen, K., 1985. Cenozoic calcareous nannofossils. *In* Bolli, H.M., Saunders, J.B., and Perch-Nielsen, K. (Eds.), *Plankton Stratigraphy:* Cambridge (Cambridge Univ. Press), 427–554.

Pimmel, A., and Claypool, G., 2001. Introduction to shipboard organic geochemistry on the *JOIDES Resolution*. *ODP Tech. Note,* 30. **doi:10.2973/odp.tn.30.2001**

Raffi, I., Backman, J., Fornaciari, E., Pälike, H., Rio, D., Lourens, L., and Hilgen, F., 2006. A review of calcareous nannofossil astrobiochronology encompassing the past 25 million years. *Quat. Sci. Rev.,* 25(23–24):3113–3137. **doi:10.1016/j.quascirev.2006.07.007**

Richter, T.O., van der Gaast, S., Koster, B., Vaars, A., Gieles, R., de Stigter, H.C., De Haas, H., and van Weering, T.C.E., 2006. The Avaatech XRF Core Scanner: technical description and applications to NE Atlantic sediments. *In* Rothwell, R.G. (Ed.), *New Techniques in Sediment Core Analysis*. Geol. Soc. Spec. Publ., 267(1):39–50. **doi:10.1144/GSL.SP.2006.267.01.03**

Rothwell, R.G., 1989. *Minerals and Mineraloids in Marine Sediments: An Optical Identification Guide:* London (Elsevier).

Sakamoto, T., Kuroki, K., Sugawara, T., Aoike, K., Iijima, K., and Sugisaki, S., 2006. Non-destructive X-ray fluorescence (XRF) core-imaging scanner, TATSCAN-F2. *Sci. Drill.*, 2:37–39. **http://www.iodp.org/iodp_journals/9_Non_Destructive_X_Ray_SD2.pdf**

Sato, T., and Takayama, T., 1992. A stratigraphically significant new species, *Reticulofenestra asanoi* (calcareous nannofossil). *In* Ishizaki, K., and Saito, T. (Eds.), *Centenary of Japanese Micropaleontology:* Tokyo (Terra Sci. Publ.), 457–460. **http://www.terrapub.co.jp/e-library/cjm/pdf/0457.pdf**

Schippers, A., Neretin, L.N., Kallmeyer, J., Ferdelman, T.G., Cragg, B.A., Parkes R.J., and Jørgensen, B.B., 2005. Prokaryotic cells of the deep sub-seafloor biosphere identified as living bacteria. *Nature (London, U. K.),* 433(7028):861–864. **doi:10.1038/nature03302**

Schlumberger, 1989. *Log Interpretation Principles/Applications:* Houston (Schlumberger Educ. Services), SMP–7017.

Shepard, F.P., 1954. Nomenclature based on sand-silt-clay ratios. *J. Sediment. Petrol.,* 24(3):151–158.

Shibuya, H., Merrill, D.L., Hsu, V., and Leg 124 Shipboard Scientific Party, 1991. Paleogene counterclockwise rotation of the Celebes Sea—orientation of ODP cores utilizing the secondary magnetization. *In* Silver, E.A., Rangin, C., von Breymann, M.T., et al., *Proc. ODP, Sci. Results,* 124: College Station, TX (Ocean Drilling Program), 519–523. **doi:10.2973/odp.proc.sr.124.169.1991**

Shipboard Scientific Party, 1993. Explanatory notes. *In* Gillis, K., Mével, C, Allan, J., et al., *Proc. ODP, Init. Repts.,* 147: College Station, TX (Ocean Drilling Program), 15–42. **doi:10.2973/odp.proc.ir.147.102.1993**

Shipboard Scientific Party, 2001a. Explanatory notes. *In* Moore, G.F., Taira, A., Klaus, A., et al., *Proc. ODP, Init. Repts.,* 190: College Station, TX (Ocean Drilling Program), 1–51. **doi:10.2973/odp.proc.ir.190.103.2001**

Shipboard Scientific Party, 2001b. Site 1177. *In* Moore, G.F., Taira, A., Klaus, A., et al., *Proc. ODP, Init. Repts.,* 190: College Station, TX (Ocean Drilling Program), 1–91. **doi:10.2973/odp.proc.ir.190.108.2001**

Shipley, T.H., Ogawa, Y., Blum, P., et al., 1995. *Proc. ODP, Init. Repts.,* 156: College Station, TX (Ocean Drilling Program). **doi:10.2973/odp.proc.ir.156.1995**

Smith, D.C., Spivack, A.J., Fisk, M.R., Haveman, S.A., Staudigel, H., and the Leg 185 Shipboard Scientific Party, 2000. Methods for quantifying potential microbial contamination during deep ocean coring. *ODP Tech. Note,* 28. **doi:10.2973/odp.tn.28.2000**

Stookey, L.L., 1970. Ferrozine—a new spectrophotometric reagent for iron. *Anal. Chem. (Washington, DC, U. S.),* 42(7):779–781. **doi:10.1021/ac60289a016**

Taira, A., Hill, I., Firth, J.V., et al., 1991. *Proc. ODP, Init. Repts.,* 131: College Station, TX (Ocean Drilling Program). **doi:10.2973/odp.proc.ir.131.1991**

Takayama, T., and Sato, T., 1987. Coccolith biostratigraphy of the North Atlantic Ocean, Deep Sea Drilling Project Leg 94. *In* Ruddiman, W.F., Kidd, R.B., Thomas, E., et al., *Init. Repts. DSDP,* 94: Washington, DC (U.S. Govt. Printing Office), 651–702. **doi:10.2973/dsdp.proc.94.113.1987**

Takayama, T., and Sato, T., 1993–1995. Coccolith biostratigraphy of the Pliocene/Pleistocene boundary stratotype. *Ann. Geol. Pays Hell.,* 36:143–150.

Thompson, P.R., Bé, A.W.H., Duplessy, J.-C., and Shackleton, N.J., 1979. Disappearance of pink-pigmented *Globigerinoides ruber* at 120,000 yr BP in the Indian and Pacific oceans. *Nature (London, U. K.),* 280(5723):554–558. **doi:10.1038/280554a0**

Tobin, H., Kinoshita, M., Ashi, J., Lallemant, S., Kimura, G., Screaton, E.J., Moe, K.T., Masago, H., Curewitz, D., and the Expedition 314/315/316 Scientists, 2009. NanTroSEIZE Stage 1 expeditions: introduction and synthesis of key results. *In* Kinoshita, M., Tobin, H., Ashi, J., Kimura, G., Lallemant, S., Screaton, E.J., Curewitz, D., Masago, H., Moe, K.T., and the Expedition 314/315/316 Scientists, *Proc. IODP,* 314/315/316: Washington, DC (Integrated Ocean Drilling Program Management International, Inc.). **doi:10.2204/iodp.proc.314315316.101.2009**

Underwood, M.B., Basu, N., Steurer, J., and Udas, S., 2003. Data report: normalization factors for semiquantitative X-ray diffraction analysis, with application to DSDP Site 297, Shikoku Basin. *In* Mikada, H., Moore, G.F., Taira, A., Becker, K., Moore, J.C., and Klaus, A. (Eds.), *Proc. ODP, Sci. Results,* 190/196: College Station, TX (Ocean Drilling Program), 1–28. **doi:10.2973/odp.proc.sr.190196.203.2003**

Vacquier, V., 1985. The measurement of thermal conductivity of solids with a transient linear heat source on the plane surface of a poorly conducting body. *Earth Planet. Sci. Lett.,* 74(2–3):275–279. **doi:10.1016/0012-821X(85)90027-5**

van der Plas, L., and Tobi, A.C., 1965. A chart for judging the reliability of point counting results. *Am. J. Sci.,* 263(1):87–90.

Von Herzen, R.P., and Maxwell, A.E., 1959. The measurement of thermal conductivity of deep-sea sediments by a needle-probe method. *J. Geophys. Res.,* 64(10):1557–1563. **doi:10.1029/JZ064i010p01557**

Young, J.R., 1998. Neogene. *In* Bown, P.R. (Ed.), *Calcareous Nannofossil Biostratigraphy*: Dordrecht (Kluwer Academic Publ.), 225–265.

Publication: 10 October 2010
MS 322-102

Figure F1. IODP conventions for naming sites, holes, cores, and samples. mbsl = meters below sea level, mbsf = meters below seafloor.

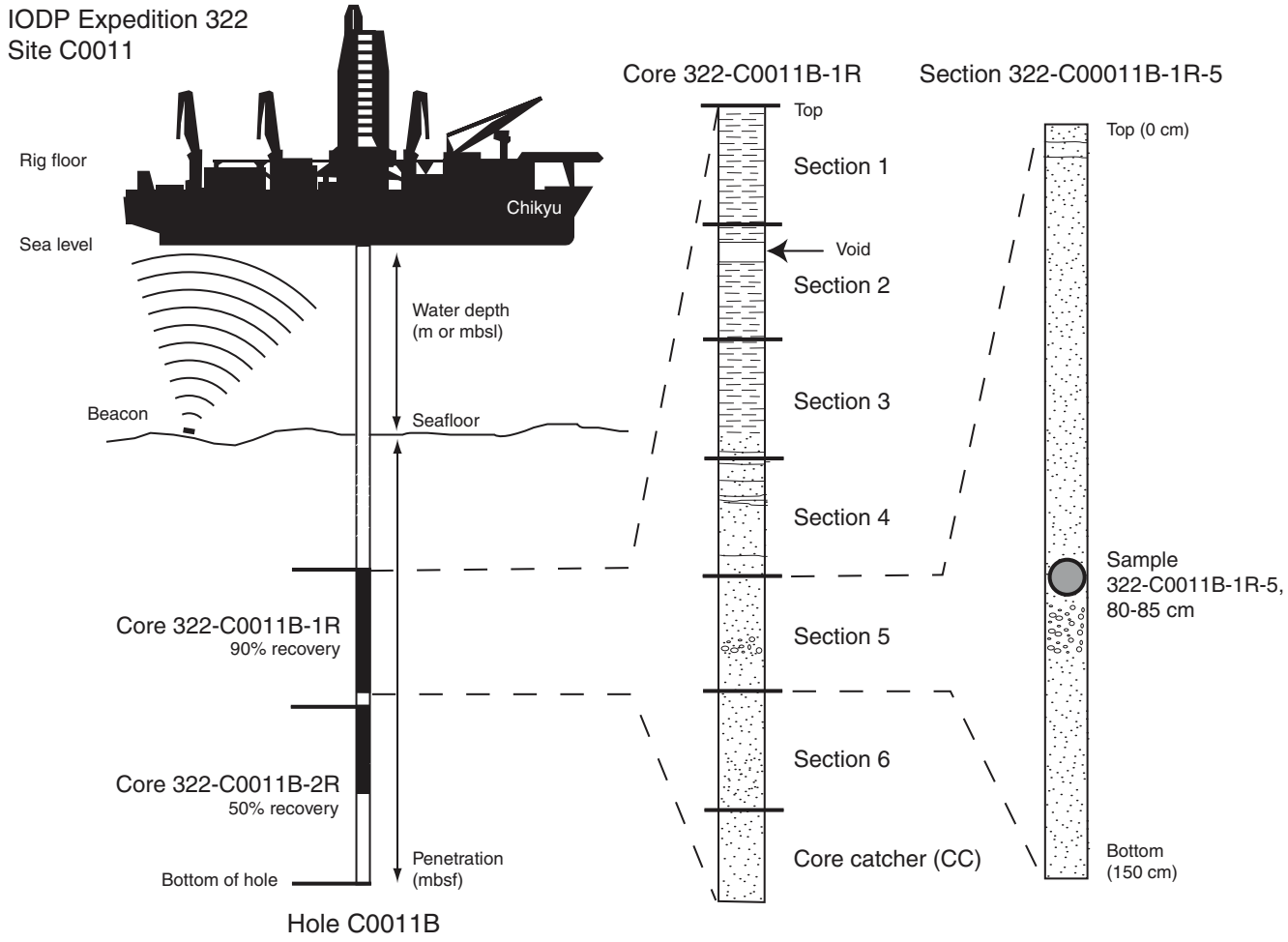

Figure F2. Overview of standard core flow from rig floor, through core cutting, core processing, description, sampling, and storage area. CT = computed tomography, MSCL-W = whole-round multisensor core logger, VCD = visual core description, MSCL-C = color spectroscopy logger, MSCL-I = photo image logger, MAD = moisture and density, XRD = X-ray diffraction, XRF = X-ray fluorescence, PWV = *P*-wave velocity, ER = electrical resistivity, GC = gas chromatograph, FID = flame ionization detector, UV = ultraviolet, ICP-AES = inductively coupled plasma–atomic emission spectroscopy, ICP-MS = inductively coupled plasma–mass spectrometry, CHNS = carbon-hydrogen-nitrogen-sulfur analyzer, SEM = scanning electron microscope, EDS = energy dispersive spectrometry, XRF-CL = X-ray fluorescence-cathodoluminescence.

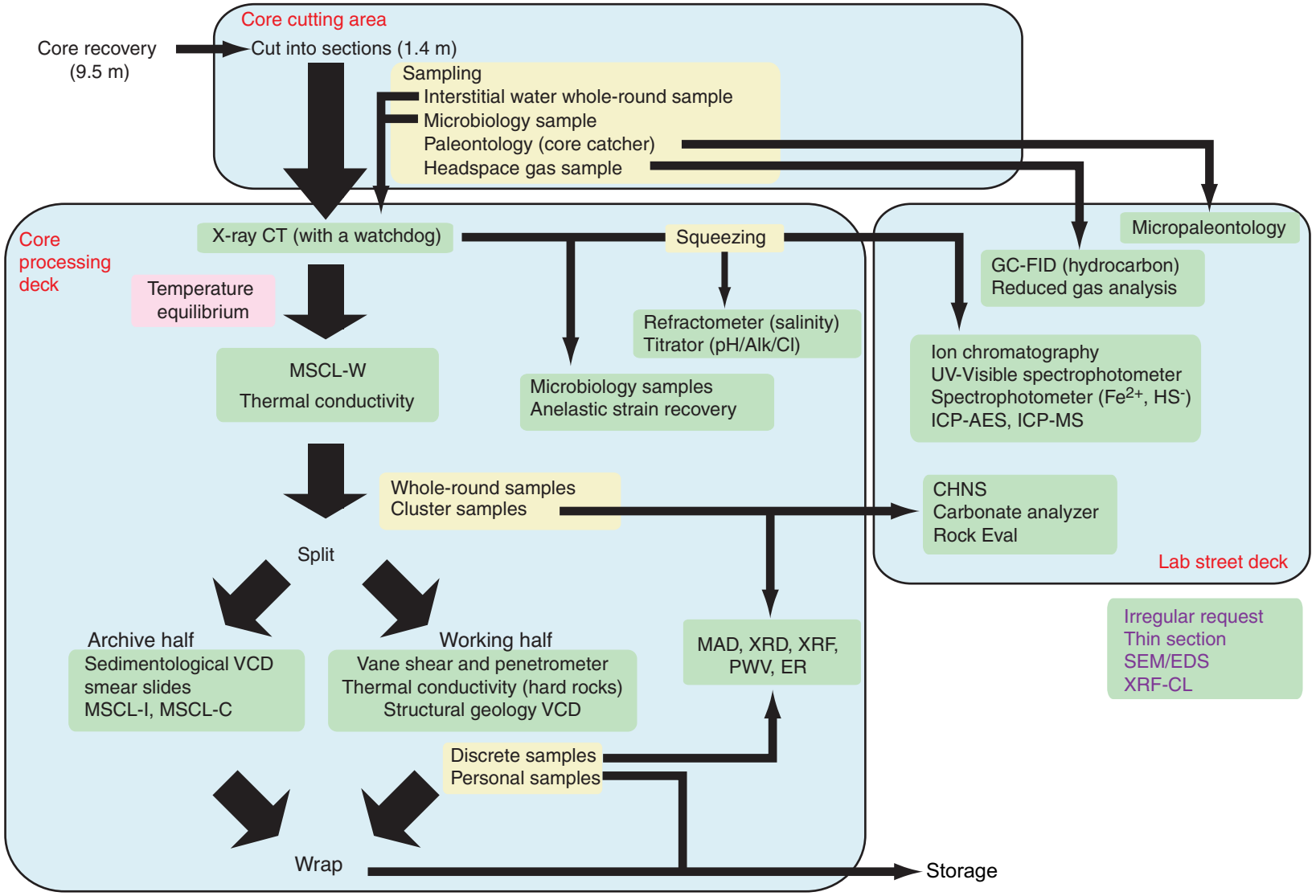

Figure F3. Graphic patterns for sedimentary lithologies encountered during Expedition 322.

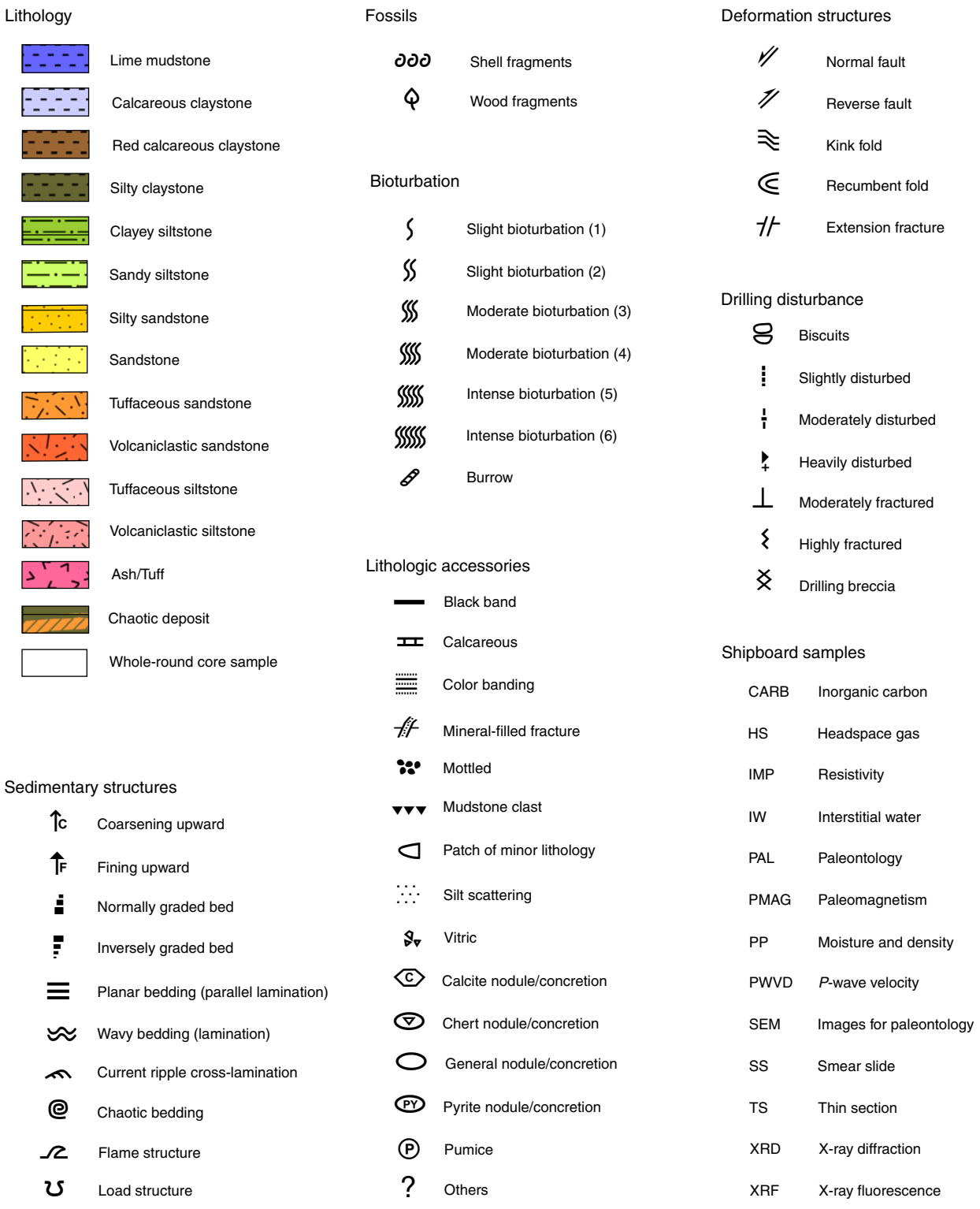

Figure F4. Diffractograms of standard mineral mixtures showing positions of diagnostic X-ray diffraction peaks used to calculate relative mineral abundances. Cl = total clay minerals, Q = quartz, P = plagioclase, Cc = calcite.

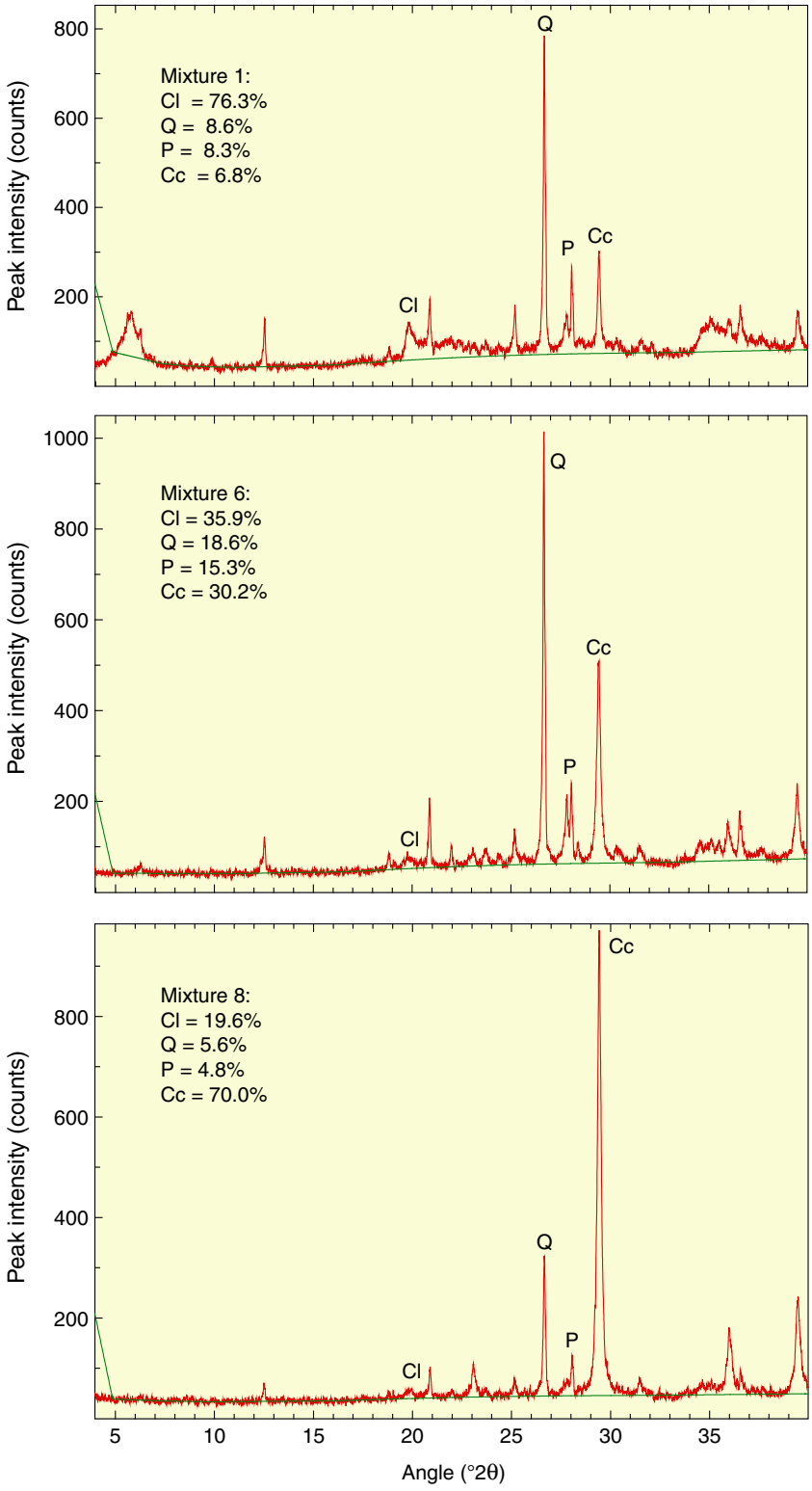

Figure F5. Graphic patterns for basement lithologies encountered during Expedition 322.

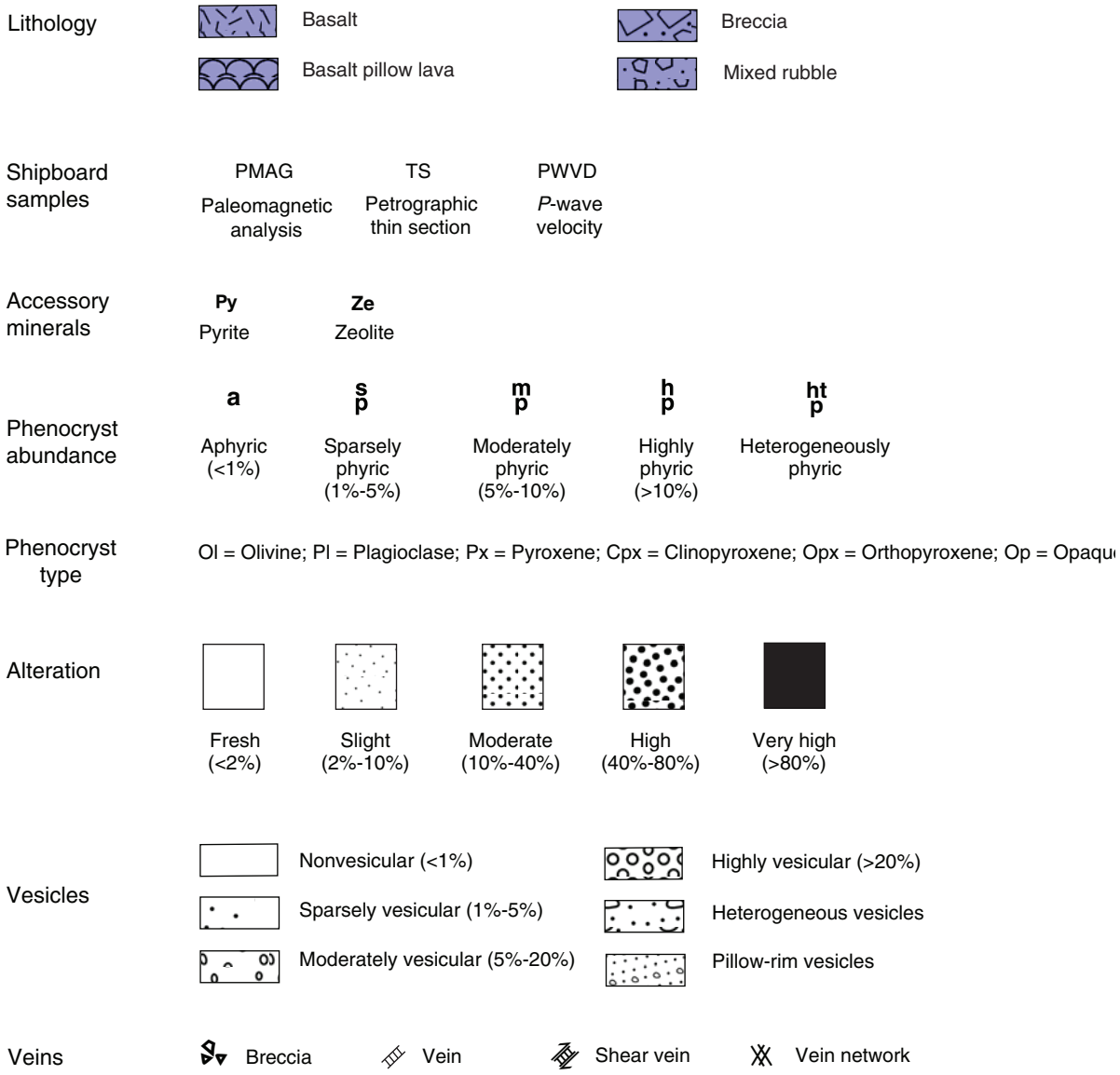

Figure F6. Log sheet used to record structural data and observations from working half of split core.

CHIKYU Operation

Last Update 5/Sep/2009

Structural Geology Observation Sheet

Exp. : Site : Core : Observer : Summary:

Section No.	Structure ID	Top of Struct	Bottom of Struct	ave, depth	Core face app. Dip		2nd app. Dip		Striation on surface		Coherent interval (for P-mag)		P-mag pole		notes
					az.	dip	az.	dip	rake	from	top	bottom	az./trend	dip	

Figure F7. Modified protractor used to measure apparent dips, trends, plunges, and rakes on planar and linear features in a split core.

Figure F8. Core coordinate system with *x*-, *y*-, *z*-axes used in orientation data calculations.

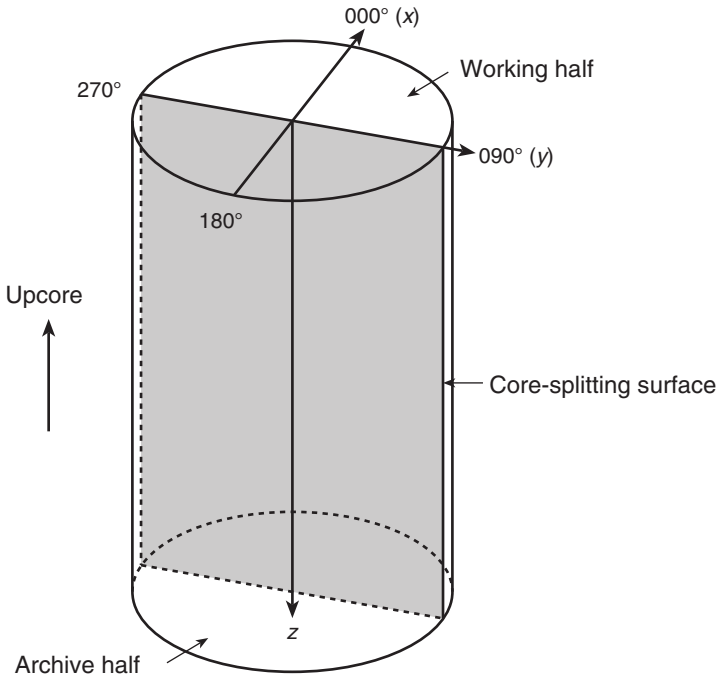

Figure F9. Spreadsheet used for recording and calculating orientation data. (**Continued on next page.**)

Site	hole	core	sect	structure ID	top of struct	bottom of struct	average depth	thickness (cm)	core face app. dip az	core face app. dip	2nd app. dip az	2nd app. dip	striation on surface rake	striation on surface from	cohoerent interval (for P-mag) top	cohoerent interval (for P-mag) bottom	P-mag pole Dec	P-mag pole Inc
C0011	B	1	1	Cleavage	16.0	20.0	18.0		90	0	0	77			16	40		
C0011	B	1	1	Striation	16.0	20.0	18.0		90	70	0	0	65	-20	16	40		
C0011	B	1	1	Vein	80.0	84.0	82.0		270	32	0	37			77	85		
C0011	B	1	2	Bedding	92.0	92.0	92.0		90	0	0	0			87	93		
C0011	B	3	3	fault	10.5	17.0	13.8		90	48	48	0			13	28		
C0011	B	3	3	Bedding	25.5	26.0	25.8		270	13	180	6			6	28		
C0011	B	4	1	fault	108.0	109.0	108.5		270	6	0	7			117	110		
C0011	B	6	1	Bedding	83.0	84.0	83.5		90	9	0	6			0	140	116.5	48.8
C0011	B	6	8	Bedding	122.0	125.0	123.5		90	10	0	2			108	133	77.2	47.4
C0011	B	7	5	Bedding	40.0	40.0	40.0		90	1	0	1			13	43		
C0011	B	7	7	Sand dike?	24.0	30.0	27.0		90	33	0	8			23	37		
C0011	B	8	1	Sand dike?	34.0	39.0	36.5		270	37	0	20			25	40		
C0011	B	8	3	Bedding	42.0	46.0	44.0		270	28	0	22			33	59		
C0011	B	8	3	fault?	52.0	58.0	55.0		270	34	0	27			33	59		
C0011	B	8	4	Bedding	99.0	105.0	102.0		270	40	0	31			62	105		
C0011	B	8	5	Bedding	6.0	14.0	10.0		270	42	0	3			0	31		
C0011	B	8	5	Sand dike?	89.0	96.0	92.5		270	54	280	0			84	105		
C0011	B	8	6	Bedding	118.0	119.0	118.5		270	6	180	35			110	124		
C0011	B	8	7	fault	8.0	22.0	15.0		90	62	328	0			10	46		
C0011	B	9	5	fault	6.0	7.0	6.5		90	3	0	15			0	9		
C0011	B	10	1	fault	103.0	105.0	104.0		270	19	0	5			102	106		
C0011	B	11	2	Sand lends top	12.0	12.0	12.0		90	3	180	9			8	18		
C0011	B	11	2	Sand lends bottom	15.0	15.0	15.0		270	11	180	3			8	18		
C0011	B	11	2	fault	40.0	41.0	40.5		270	4	180	2			34	70		
C0011	B	11	2	Bedding	92.0	93.0	92.5		270	3	180	7			87	96		
C0011	B	11	3	fault	12.0	13.0	12.5		90	2	0	6			11	12		
C0011	B	11	3	Bedding	18.0	19.0	18.5		90	2	0	5			11	12		
C0011	B	11	3	Bedding	25.0	26.0	25.5		90	1	0	6			21	33		

≤90

±1, 90 or 270
top->"1"
bottom->"-1"

Red indicates less reliable pmag data (MAD>20)

Figure F9 (continued).

depth (mbsf)	plane-normal orientation					plane orientation (RHR)			fault			corrected orientation (RHR)			fault		
	l	m	n	az	dip	dip dir	strike	dip	csf rake	str rake	slip sense	dip dir	srtike	dip	str rake	slip sense	notes
340.180	0.97	0.00	-0.22	360	-13	360	270	77				360	270	77			
340.180	0.00	0.94	-0.34	90	-20	90	0	70				90	0	70			mirror surface
340.820	-0.51	0.42	0.68	140	46	320	230	44				320	230	44			Carbonate vein
341.795	0.00	0.00	-1.00	90	-90	90	0	0				90	0	0			Chlorite
360.308	-0.55	0.50	-0.45	138	-31	138	48	59				138	48	59			
360.428	-0.10	-0.22	-0.97	246	-76	246	156	14				246	156	14			measured on CT image
366.085	-0.12	0.10	0.99	139	81	319	229	9				319	229	9			layer parallel fault
384.835	0.10	0.16	-0.98	56	-79	56	326	11				300	210	11			lamination, sharp boundary
393.005	0.03	0.17	-0.98	79	-80	79	349	10				2	272	10			with thin black layer , homogeneous
397.235	0.02	0.02	-1.00	45	-89	45	315	1				45	315	1			clay above, bioturbated clay below
399.935	0.03	0.54	-0.84	87	-57	87	357	33				87	3[illegible]	[illegible]			black clast -> thin section
403.365	-0.27	0.57	0.75	116	50	296	206	40				[illegible]	2[illegible]	40			
405.025	-0.33	0.44	0.82	127	56	307	217	34				30[illegible]	217	[illegible]			Base chaotic
405.135	-0.50	0.45	0.66	138	45	318	228	45				318	228	45			
407.015	-0.39	0.55	0.66	126	44	306	216	46				306	216	46			Base sand
407.505	-0.04	0.67	0.74	93	48	273	183	42				273	183	42			Sand base
408.330	0.80	0.14	0.10	10	7	190	100	83				190	100	83			
410.000	-0.57	-0.09	-0.81	189	-55	189	99	35				189	99	35			Sand base
410.375	0.47	0.75	-0.40	58	-24	58	328	66				58	328	66			
416.925	0.26	0.05	-0.96	11	-75	11	281	15				11	281	15			highly disturbed core
423.040	-0.08	0.32	0.94	104	70	284	194	20				284	194	20			highly disturbed core
433.020	0.16	-0.05	0.99	342	81	162	72	9				162	72	9			
433.050	-0.05	-0.19	-0.98	255	-79	255	165	11				255	165	11			
433.305	-0.03	-0.07	-1.00	243	-86	243	153	4				243	153	4			
433.825	-0.12	-0.05	-0.99	203	-82	203	113	8				203	113	8			
434.430	0.10	0.03	-0.99	18	-84	18	288	6				18	288	6			layer parallel fault
434.490	0.09	0.03	-1.00	22	-85	22	292	5				22	292	5			lamina
434.560	0.10	0.02	-0.99	9	-84	9	279	6				9	279	6			lamina

Red indicates less reliable pmag data (MAD>20)

Figure F10. Calculation of plane orientation (shaded) from two apparent dips. Intersections of split core surface and section perpendicular to split core surface and parallel to core direction with plane of interest are shown. (α_1, β_1) and (α_2, β_2) = azimuths and dips of traces of the plane on two sections, v_1 and v_2 = unit vectors parallel to traces of the plane on two sections, v_n = unit vector normal to plane.

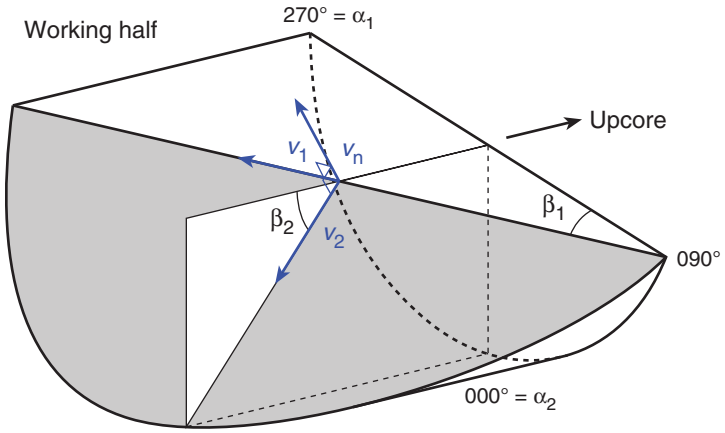

Figure F11. Dip direction (α_d), right-hand rule strike (α_s), and dip (β) of a plane deduced from its normal azimuth (α_n) and dip (β_n). **A.** $\beta_n < 0°$. **B.** $\beta_n \geq 0°$. v_n = unit vector normal to plane.

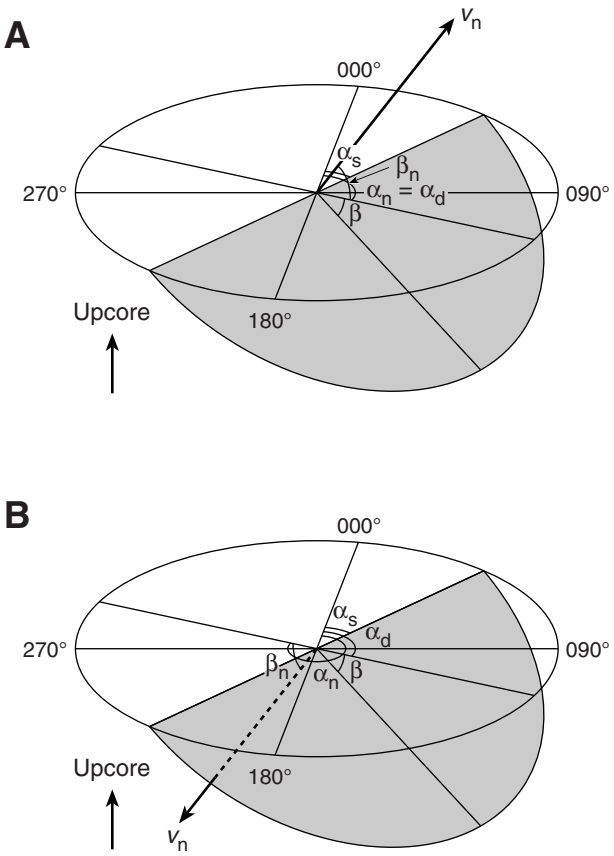

Figure F12. Apparent rake measurement of slickenlines on a fault surface from 270° direction of split core surface trace. ϕ_a = apparent rake, v_n = unit vector normal to fault plane, v_c = unit vector normal to split core surface, v_i = unit vector parallel to the intersection line between fault plane and split core surface.

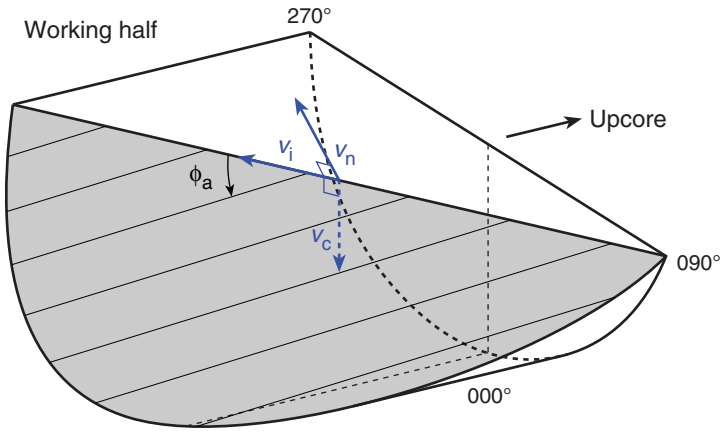

Figure F13. Rake of slickenlines (ϕ) deduced from the rake of intersection line between fault plane and split core surface (ϕ_i) and apparent rake measured (ϕ_a). **A.** ϕ_a from top or 090° direction where fault plane dips westward. **B.** ϕ_a from bottom or 090° direction where fault plane dips eastward. **C.** ϕ_a from top or 270° direction where fault plane dips eastward. **D.** ϕ_a from bottom or 270° direction where fault plane dips westward. α_s = right-hand rule strike of fault plane, v_n = unit vector normal to fault plane, v_c = unit vector normal to split core surface, v_i = unit vector parallel to intersection line between fault plane and split core surface. v_s = horizontal unit vector in the right-hand rule strike direction of fault plane.

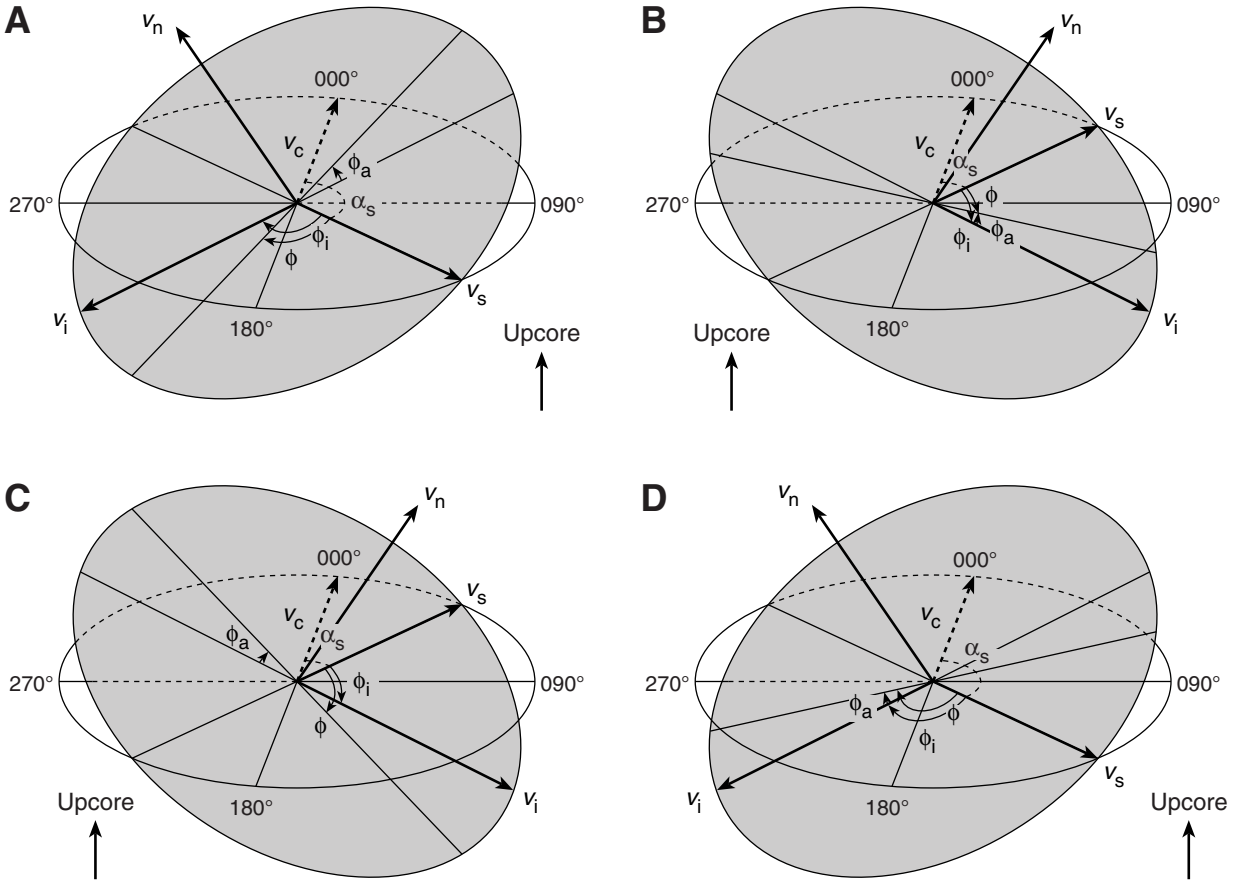

Figure F14. Azimuth correction based on paleomagnetic data. **A.** Paleomagnetic inclination $\beta_p \geq 0°$. **B.** Paleomagnetic inclination $\beta_p < 0°$. α_p = paleomagnetic declination, α_d and α_s = dip direction and right-hand rule strike of a plane.

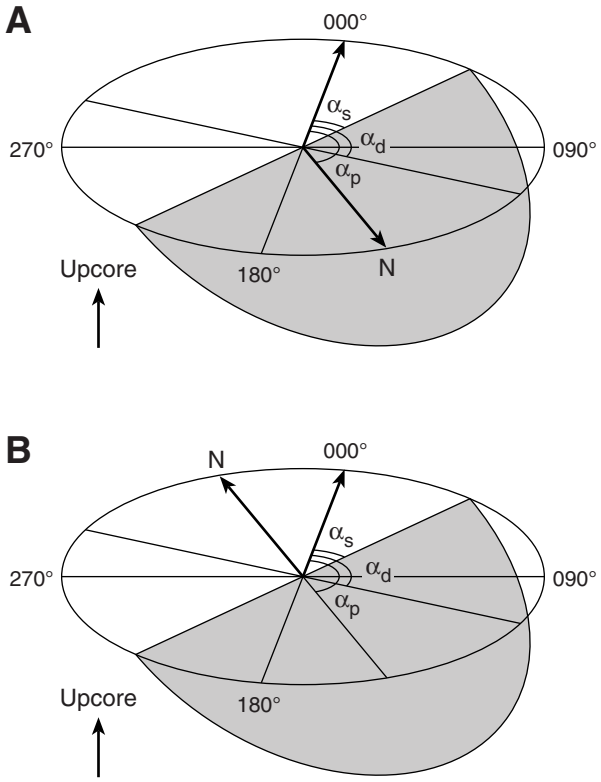

Figure F15. Correlation of geomagnetic polarity timescale (Lourens et al., 2004), biostratigraphic zonation, and biohorizons used during Expedition 322. FO = first occurrence, LO = last occurrence, LCO = last consistent occurrence, FCO = first consistent occurrence, PE = paracme end, PB = paracme beginning, SD = sinistral coiling direction.

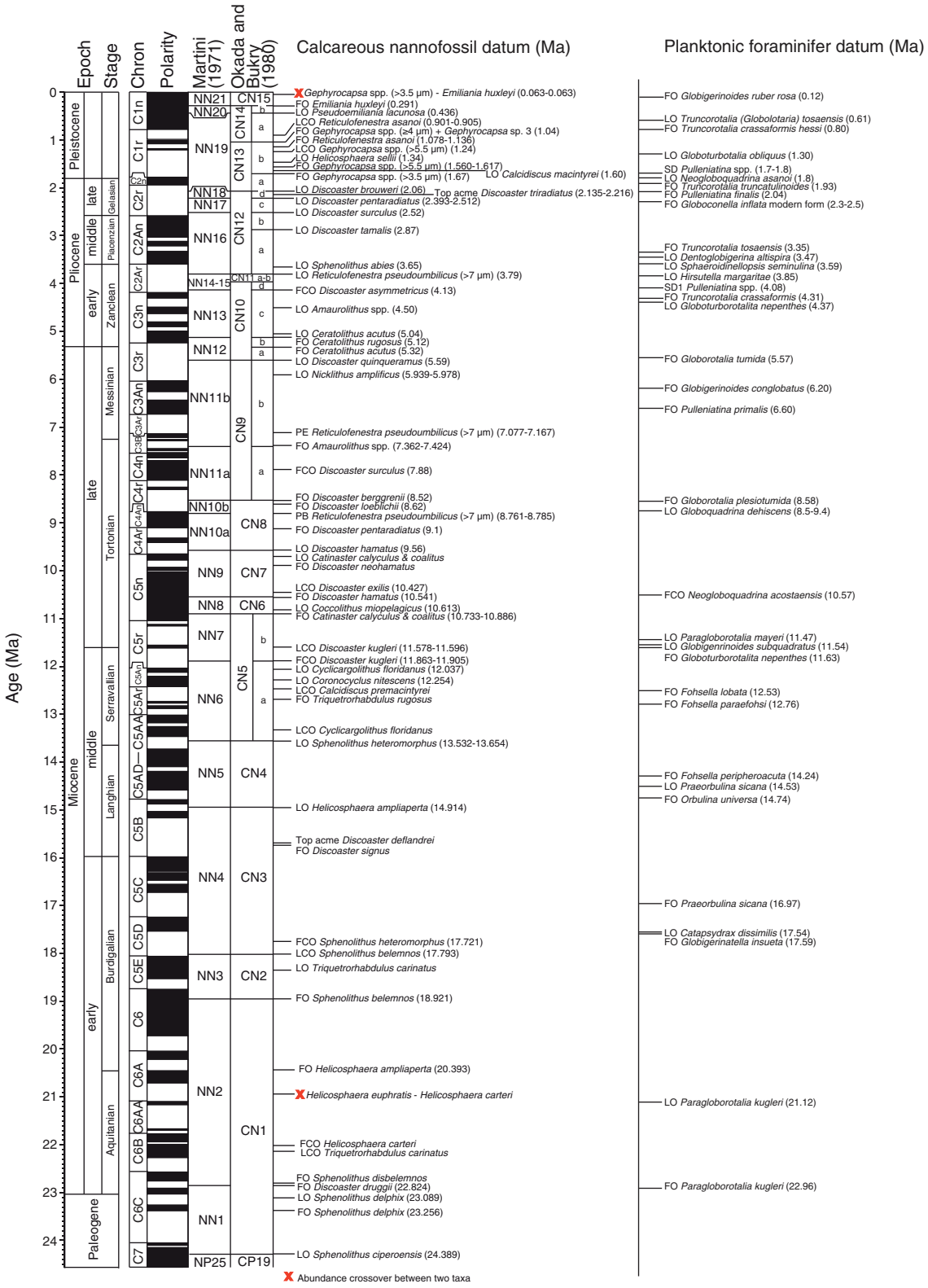

Figure F16. Orientation system of cores, discrete samples, and superconducting rock magnetometer used during Expedition 322. SQUID = superconducting quantum interference device.

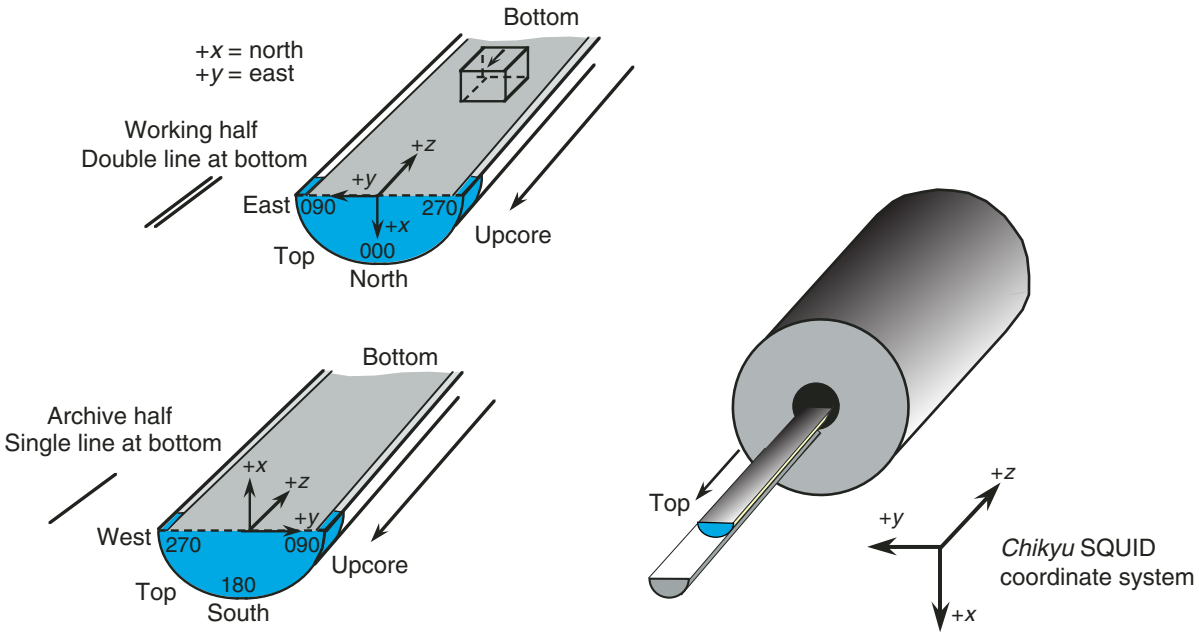

Figure F17. Definition of axis orientation on working-half sections. The z-axis is positive in the downhole direction of the core.

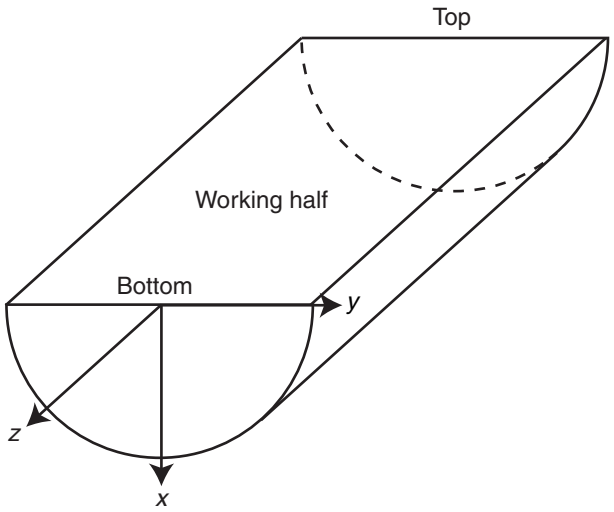

Figure F18. Subsampling equipment and procedure for 5 cm whole-round cores used for cell counting, cell cultivation, and FISH studies. **A.** Autoclaved stainless steel subcoring tool in scientist's hand used to (**B**) subcore the whole-round core, which is kept chilled (in autoclavable pan) by premolded gel ice packs. **C.** Small 2–3 cm^3 sediment subsamples are placed into sterile plastic tubes (stored in an autoclavable plastic rack) and fixed with chilled sterile 2% paraformaldehyde in phosphate buffered saline ("PFA") solution. FISH samples are homogenized, incubated, washed, and stored for use (see above).

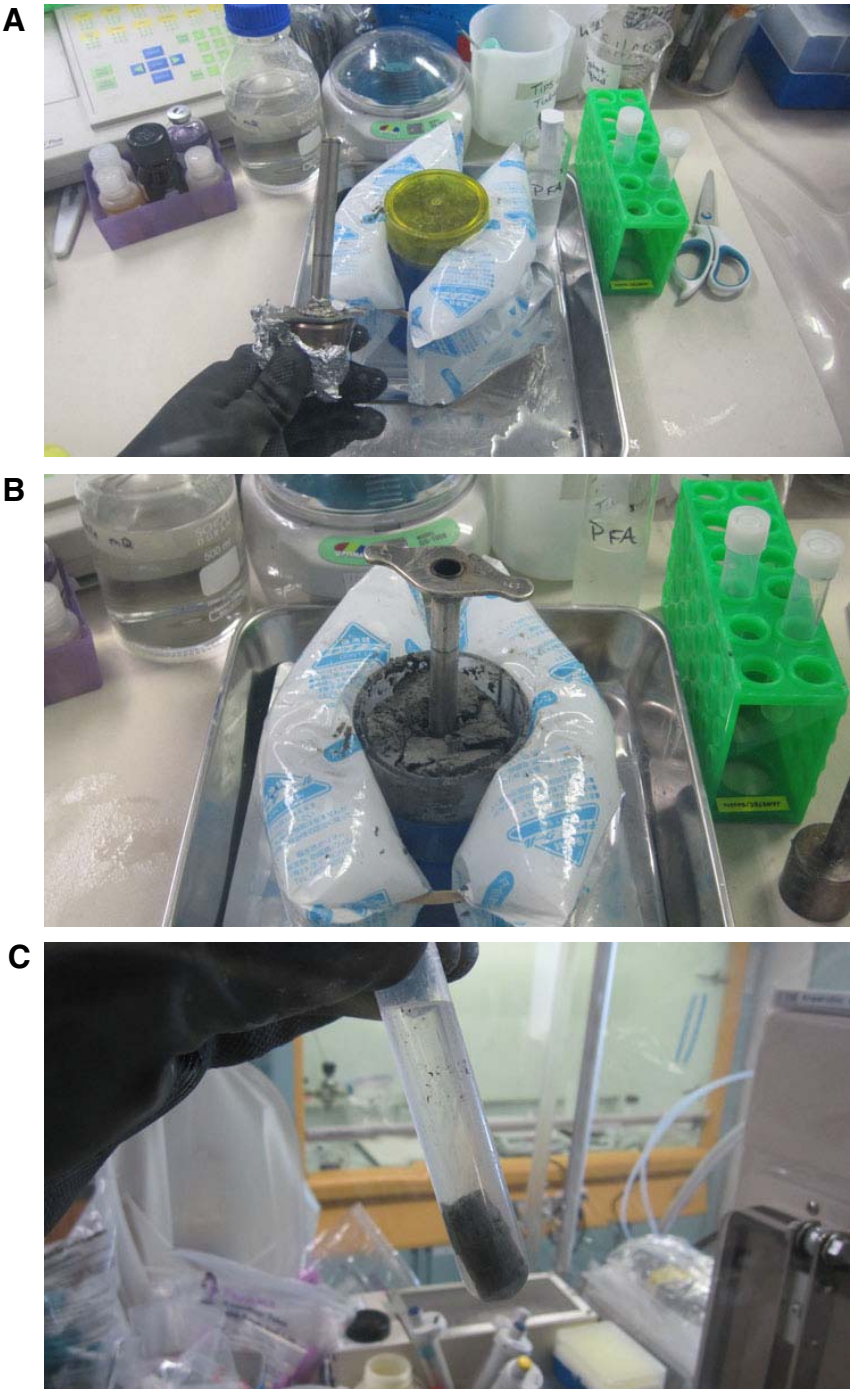

Figure F19. A. LWD/MWD tool string used during Expedition 319. **B.** Position and components of geoVISION tool.

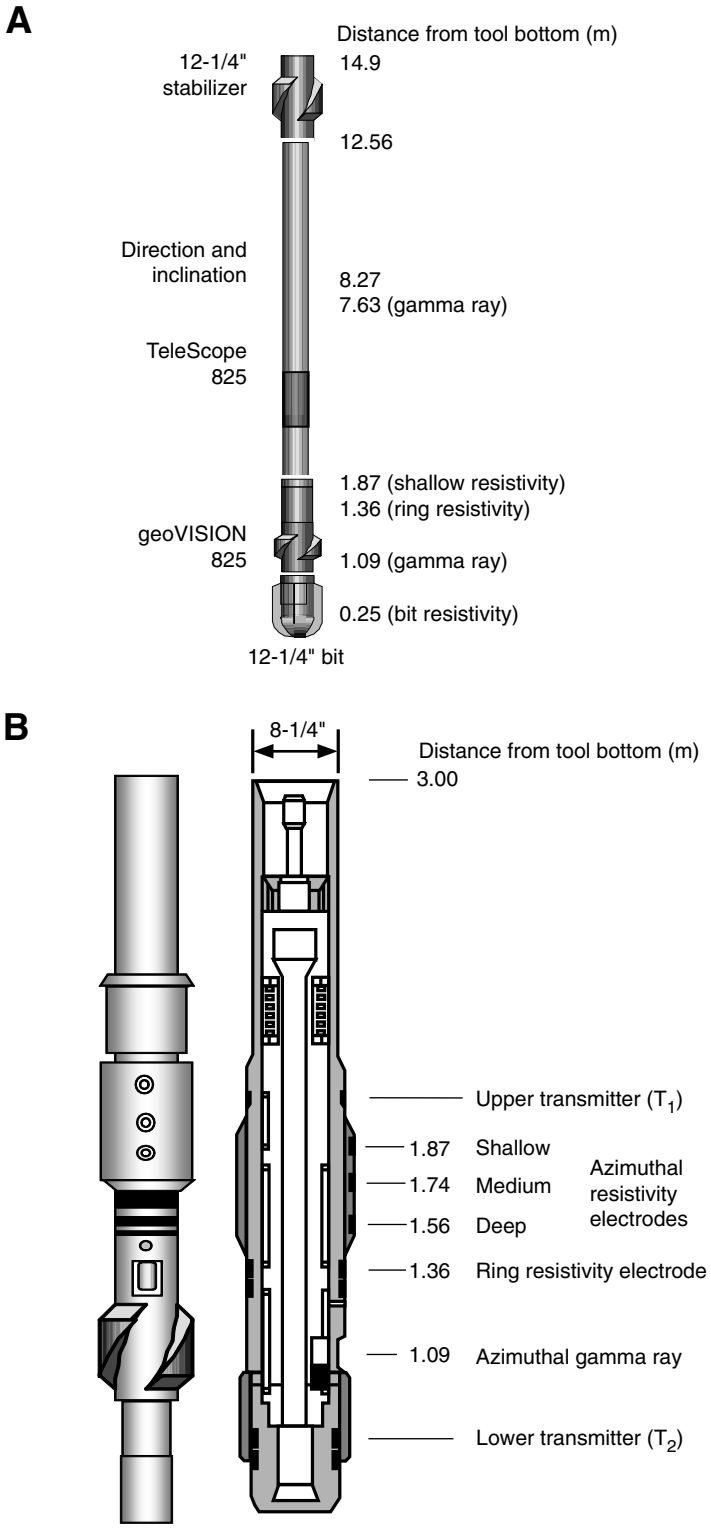

Figure F20. Shipboard structure and data flow. MWD = measurement while drilling, LWD = logging while drilling, IDEAL = integrated drilling evaluation and logging, MAXIS = Multitask Acquisition Imaging System, CDEX = Center for Deep Earth Exploration, LAS = log ASCII standard, DLIS = digital logging interchange standard, SEGY = Society of Exploration Geophysicists standard Y.

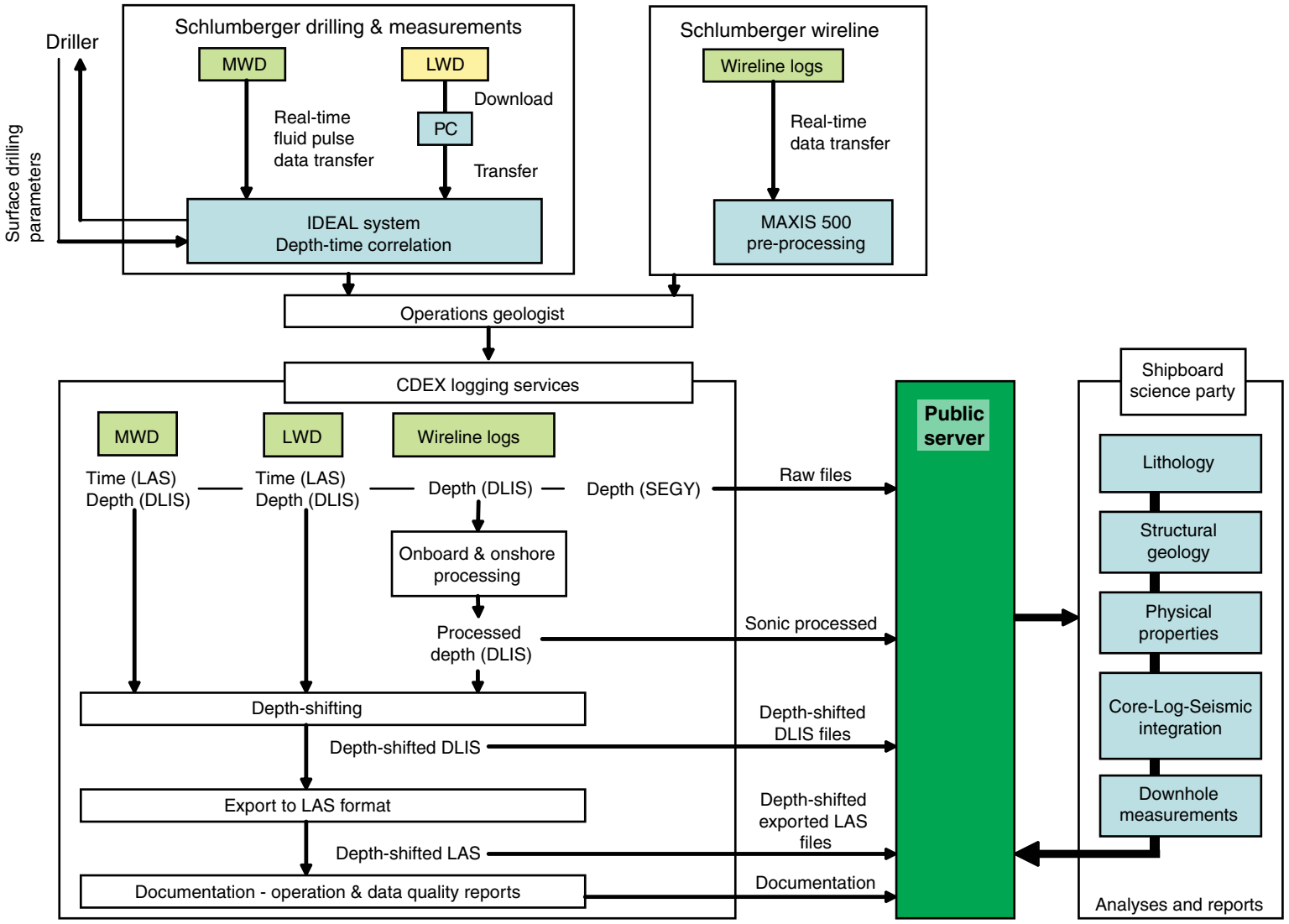

Table T1. Scan settings for X-ray CT scanner. (See table notes.)

Parameter	Setting
Scan type	Helical-full-0.5 s
Interval (mm)	0.625
Gantry tilt	S0.0
SFOV	Small
Tube voltage (kV)	120
Tube current (mA)	100
Detector rows	16
Helical thickness (mm)	0.625
Pitch	0.562:1
Speed (mm/rot)	5.62
DFOV (cm)	9.6
R/L center (mm)	R0.0
A/P center (mm)	A0.0
Recon type	Detail
Matrix size (pixel)	512 × 512
Recon option	Full
Direct vis	Off

Notes: Protocol name: 090624_Exp319 9.1 071210_Aluminum Piece. SFOV = scan field of view, DFOV = dual field of view. R/L center = distance right or left of the center line, A/P center = distance anterior or posterior of the center line.

Table T2. Classification of volcanic lithologies. (See table notes.)

	Mixture		
	Tephras	Volcaniclastic deposits	Epiclastic deposits
>64 mm	Pyroclastic breccia	Volcaniclastic breccia/conglomerate	Breccia/Conglomerate
2–64 mm	Lapilistone/Lapili tuff	Volcaniclastic gravel	Gravel
64 µm–2 mm	Coarse ash/tuff	Volcaniclastic sandstone	Sandstone
2–64 µm	Fine ash/tuff	Volcaniclastic siltstone	Siltstone
<2 µm	Volcanic dust	Volcaniclastic volcanic dust	Claystone
Amount of pyroclasts	≥75%	<75% to >25%	≤25%

Notes: Modified after Fisher and Schmincke (1984). If >25% of volcaniclasts are vitric pyroclasts, then material is tuffaceous.

Table T3. Smear slide component categories.

Monomineralic grains														Lithic grains					Pelagic grains						Other	
Quartz	Feldspar	Pyroxene	Amphibole	FeOOH	Glauconite	Zircon	Pyrite	Chlorite	Opaque grains	Apatite	Barite	Olivine	Garnet	Biotite/Mica	Carbonate minerals	Volcanic glass	Volc. lithic	Sed. lithic	Chert	Meta. lithic	Nannofossils	Foraminifers	Diatoms	Radiolarians	Silicoflagellates	Sponge spicules	Clay minerals	Zeolite

Table T4. Characteristic X-ray diffraction peaks for semiquantitative area analysis.

Mineral	Reflection	d-Value (Å)	Peak position (°2θ)
Composite clay	Multiple	4.478	19.4–20.4
Quartz	101	3.342	26.3–27.0
Plagioclase	002	3.192	27.4–28.2
Calcite	104	3.035	29.1–29.7

Table T5. Normalization factors for calculation of relative mineral abundance using bulk powder X-ray diffraction analysis. (See table note.)

Affected mineral in standard mixture:	Normalization factor			
	Total clay	Quartz	Plagioclase	Calcite
Influencing mineral:				
Total clay	9.8956702E–03	–1.5889532E–04	–2.8855808E–04	–7.3842803E–04
Quartz	–4.7221169E–05	5.8782392E–04	–4.7869325E–05	–3.1098843E–05
Plagioclase	7.2794763E–04	–4.2840613E–05	1.3719777E–03	–3.6005495E–05
Calcite	4.2042411E–05	3.3021188E–06	–4.1329499E–06	1.3071455E–03

Note: Singular value decomposition was used to compute factors, following Fisher and Underwood (1995).

Table T6. Quantitative conditions for XRF analyses. (See table note.)

Oxide (wt%)	Line	Voltage (kV)	Intensity (mA)	Crystal	Detector	Peak angle (°2θ)	Count time (s)	
							Peak	Background
Na_2O	K-alpha	50	4.00	RX25	PC	47.138	40	20
MgO	K-alpha	50	4.00	RX25	PC	38.828	40	20
Al_2O_3	K-alpha	50	4.00	PET	PC	144.644	40	20
SiO_2	K-alpha	50	4.00	PET	PC	108.992	40	10
P_2O_5	K-alpha	50	4.00	PET	PC	89.429	40	20
K_2O	K-alpha	50	4.00	PET	PC	50.684	40	10
CaO	K-alpha	50	4.00	PET	PC	45.191	40	10
TiO_2	K-alpha	50	4.00	LiF1	SC	86.143	20	
MnO	K-alpha	50	4.00	LiF1	SC	62.999	20	20
Fe_2O_3	K-alpha	50	4.00	LiF1	SC	57.532	20	10

Note: PC = flow-proportioned counter, SC = scintillation counter.

Table T7. Continuous measurement results for check samples (30 repetitions). (See table note.)

Reference material	Na_2O	MgO	Al_2O_3	SiO_2	P_2O_5	K_2O	CaO	TiO_2	MnO	Fe_2O_3
JA-1:										
Average (wt%)	3.86	1.52	15.15	64.27	0.16	0.78	5.66	0.85	0.16	7.08
SD (wt%)	0.04	0.02	0.03	0.06	0.004	0.009	0.008	0.008	0.002	0.01
RSD (%)	1.1	1.5	0.2	0.1	2.3	1.1	0.1	0.9	1.3	0.2
3σ (wt%)	0.13	0.07	0.08	0.17	0.01	0.03	0.02	0.02	0.006	0.04
JB-3:										
Average (wt%)	2.83	5.19	17.23	50.83	0.29	0.78	9.67	1.43	0.18	11.86
SD (wt%)	0.06	0.03	0.03	0.07	0.004	0.01	0.01	0.01	0.002	0.02
RSD (%)	2.0	0.6	0.2	0.1	1.4	1.3	0.1	0.9	1.3	0.2
3σ (wt%)	0.17	0.09	0.08	0.21	0.01	0.03	0.03	0.04	0.007	0.05

Note: SD = standard deviation, RSD = relative standard deviation, 3σ = control limit.

Table T8. Classification of volcanic basement lithologies. (See table note.)

Phenocryst abundance
Aphanitic rocks:
Aphyric: <1%
Sparsely phyric: 1%–2%
Moderately phyric: 2%–10%
Highly phyric: >10%
Degree of crystallinity
Holohyaline: 100% glass
Hypohyaline: ≥50% glass
Hypocrystalline: ≥50% crystals
Holocrystalline: 100% crystals
Grain size
Aphanitic rocks:
Cryptocrystalline: very fine crystals visible, but not identifiable with a petrographic microscope
Microcrystalline: small crystals (≤0.01 mm) identifiable with a petrographic microscope
Microlitic: partially crystalline rock containing small euhedral crystals, identifiable with a petrographic microscope
Phaneritic rocks*:
Fine grained: <1 mm
Medium grained: 1–5 mm
Coarse grained: >5 mm

Note: * = average grain size.

Table T9. Astronomically calibrated age estimates of calcareous nannofossil datums used as biostratigraphic tie points, Expedition 322. (See table notes.) (Continued on next page.)

Nannofossil event	Zone (base)	Degree of reliability	Age (Ma)
X medium *Gephyrocapsa* (>3.5 µm)–*Emiliania huxleyi*			0.082–0.063
FO *Emiliania huxleyi*	NN21	B	0.291
LO *Pseudoemiliania lacunosa*	NN20	A	0.436
LCO *Reticulofenestra asanoi*		A	0.905–0.901*
RE medium *Gephyrocapsa* (≥4 µm) + FO *Gephyrocapsa* sp. 3 *(G. parallela)*		A	1.04
FCO *Reticulofenestra asanoi*		D	1.136–1.078*
LO large *Gephyrocapsa* (>5.5 µm)		A	1.24
LO *Helicosphaera sellii*		C	1.34
FCO large *Gephyrocapsa* (>5.5 µm)			1.46
FO large *Gephyrocapsa* (>5.5 µm)		B	1.560–1.617*
LO *Calcidiscus macintyrei* (≥11 µm)		C	1.60
FO medium *Gephyrocapsa* (>3.5 µm)		A	1.67
LO *Discoaster brouweri*	NN19	A	2.06
AB *Discoaster triradiatus*		A	2.135–2.216*
LO *Discoaster pentaradiatus*	NN18	C	2.393–2.512*
LO *Discoaster surculus*	NN17	C	2.52
LO *Discoaster tamalis*		C	2.87
LO *Sphenolithus* spp.		C	3.65
LO *Reticulofenestra pseudoumbilicus* (>7 µm)	NN16	A	3.79
FCO *Discoaster asymmetricus*	NN15–NN14	B	4.13
LO *Amaurolithus primus*			4.50
LO *Ceratolithus acutus*		B	5.04
FO *Ceratolithus rugosus*	NN13	D	5.12
LO *Triquetrorhabdulus rugosus*			5.279*
FO *Ceratolithus acutus*		B	5.32
LO *Discoaster quinqueramus*	NN12	A	5.59
LO *Nicklithus amplificus*		A	5.978–5.939*
FO *Nicklithus amplificus*		C	6.909–6.684*
PE *Reticulofenestra pseudoumbilicus* (>7 µm)		D	7.077–7.167*
FO *Amaurolithus* spp./*Amaurolithus primus*	NN11b	A	7.362–7.424*
FCO *Discoaster surculus*		B	7.88
LCO *Minylitha convallis*		D	7.78–8.3
FO *Discoaster berggrenii*	NN11a	D	8.52
PB *Reticulofenestra pseudoumbilicus* (>7 µm)	NN10b	A	8.785–8.761*
FO *Discoaster pentaradiatus*			9.1
FO *Minylitha convallis*		D	9.416
LO *Discoaster hamatus*	NN10a	C	9.560
LO *Catinaster calyculus*		D	9.674*
LO *Catinaster coalitus*		D	9.687*
X *Discoaster hamatus–D. neohamatus*			9.762*
FO *Discoaster neohamatus*		C	9.867–10.521*
LCO *Discoaster exilis*			10.427
FO *Discoaster hamatus*	NN9	C	10.541
LO *Coccolithus miopelagicus*		C	10.613
FO *Discoaster calcaris*			10.676
FO *Discoaster bellus* gr.		C	10.72
FO *Discoaster brouweri*		A	10.734–10.764*
FO *Catinaster calyculus*		D	10.785*
FO *Catinaster coalitus*	NN8	D	10.886–10.733*
LCO *Discoaster kugleri*		A	11.578–11.596*
FCO *Discoaster kugleri*	NN7	B	11.863–11.905*
LO *Cyclicargolithus floridanus*		D	12.037
LO *Coronocyclus nitescens*			12.254
LCO *Calcidiscus premacintyrei*		A	12.447
FCO *Triquetrorhabdulus rugosus*			12.671
LCO *Cyclicargolithus floridanus*		A	13.294
LO *Sphenolithus heteromorphus*	NN6	C	13.532–13.654*
LO *Helicosphaera ampliaperta*	NN5		14.914*
AE *Discoaster deflandrei*			15.663*
FO *Discoaster signus*			15.702*
FCO *Sphenolithus heteromorphus*			17.721*
LCO *Sphenolithus belemnos*	NN4		17.973*
LO *Triquetrorhabdulus carinatus*		D	18.315*
FO *Sphenolithus belemnos*	NN3		18.921*
FO *Helicosphaera ampliaperta*			20.393*
X *Helicosphaera euphratis–Helicosphaera carteri*			20.894*
FCO *Helicosphaera carteri*			21.985*

Table T9 (continued).

Nannofossil event	Zone (base)	Degree of reliability	Age (Ma)
LCO *Triquetrorhabdulus carinatus*			22.092
FO *Sphenolithus disbelemnos*		C	22.413
FO *Discoaster druggii*	NN2	D	22.824*
LO *Sphenolithus delphix*		A	23.089
FO *Sphenolithus delphix*		A	23.356
LO *Sphenolithus ciperoensis*	NN1	C	24.389

Notes: Datums are based on Pacific records if not otherwise stated. * = datums based on Atlantic or Mediterranean records. Age estimates adopted from Raffi et al. (2006). X = abundance crossover, FO = first occurrence, LO = last occurrence, LCO = last consistent occurrence, RE = reentrance, FCO = first consistent occurrence, AB = acme beginning, AE = acme end, PE = paracme end, PB = paracme beginning. Degree of reliability: A = distinct, well defined, and isochronous worldwide; B = indistinct and less well defined but reasonably isochronous; C = distinct and well defined but diachronous; D = indistinct, poorly defined, and diachronous. See Raffi et al. (2006) for detailed explanation.

Table T10. Astronomically calibrated age estimates of planktonic foraminifer datums used as biostratigraphic tie points, Expedition 322. (**See table notes.**)

Planktonic foraminiferal event	Zone (base)	Age (Ma)
LO *Globigerinoides ruber rosa*		0.12
LO *Truncorotalia tosaensis*		0.61
FO *Truncorotalia crassaformis hessi*		0.8
SD2 *Pulleniatina* spp.		1.7–1.8
LO *Neogloboquadrina asanoi*		1.8
FO *Truncorotalia truncatulinoides*	N22	1.93
FO *Globoconella inflata* modern form		2.3–2.5
FO *Truncorotolia tosaensis*	N21	3.35
LO *Dentoglobigerina altispira*		3.47
LO *Sphaeroidinellopsis seminulina*		3.59
LO *Hirsutella margaritae*		3.85
SD1 *Pulleniatina* spp.		4.08
FO *Truncorotalia crassaformis*		4.31
LO *Globoturborotalita nepenthes*	N19	4.37
FO *Globorotalita tumida*	N18	5.57
FO *Globigerinoides conglobatus*		6.2
FO *Pulleniatina primalis*	N17b	6.6
FO *Globorotalita plesiotumida*	N17a	8.58
LO *Globoquadrina dehiscens*		8.5–9.4
FCO *Neogloboquadrina acostaensis*	N16	10.57
LO *Paragloborotalia mayeri*	N15	11.47
LO *Globigeriniodes subquadratus*		11.54
FO *Globoturborotalita nepenthes*	N14	11.63
FO *Fohsella lobata*	N12	12.53
FO *Fohsella praefohsi*	N11	12.76
FO *Fohsella peripheroacuta*	N10	14.24
FO *Orbulina universa*	N9	14.74
FO *Praeorbulina sicana*	N8	16.97
LO *Catapsydrax dissimilis*	N7	17.54
FO *Globigerinatella insueta*	N6	17.59
LO *Paragloborotalia kugleri*	N5	21.12
FO *Paragloborotalia kugleri*	N4	22.96

Notes: Zonation and datums taken from tropical area of the Pacific. Astronomical age estimation from Lourens et al. (2004). FO = first occurrence, LO = last occurrence, SD = change in coiling direction, FCO = first consistent occurrence.

Table T11. Ages used for geomagnetic polarity timescale. (See table note.)

Interval (Ma)		Chron/ subchron
Top	Bottom	
0.000	0.781	C1n
0.988	1.072	C1r.1n
1.173	1.185	C1r.2n
1.778	1.945	C2n
2.581	3.032	C2An.1n
3.116	3.207	C2An.2n
3.330	3.596	C2An.3n
4.187	4.300	C3n.1n
4.493	4.631	C3n.2n
4.799	4.896	C3n.3n
4.997	5.235	C3n.4n
6.033	6.252	C3An.1n
6.436	6.733	C3An.2n
7.140	7.212	C3Bn
7.251	7.285	C3Br.1n
7.454	7.489	C3Br.2n
7.528	7.642	C4n.1n
7.695	8.108	C4n.2n
8.254	8.300	C4r.1n
8.769	9.098	C4An
9.321	9.409	C4Ar.1n
9.656	9.717	C4Ar.2n
9.779	9.934	C5n.1n
9.987	11.040	C5n.2n
11.118	11.154	C5r.1n
11.554	11.614	C5r.2n
12.041	12.116	C5An.1n
12.207	12.415	C5An.2n
12.730	12.765	C5Ar.1n
12.820	12.878	C5Ar.2n
13.015	13.183	C5AAn
13.369	13.605	C5ABn
13.734	14.095	C5ACn
14.194	14.581	C5ADn
14.784	14.877	C5Bn.1n
15.032	15.160	C5Bn.2n
15.974	16.268	C5Cn.1n
16.303	16.472	C5Cn.2n
16.543	16.721	C5Cn.3n
17.235	17.533	C5Dn
18.056	18.524	C5En
18.748	19.722	C6n
20.040	20.213	C6An.1n
20.439	20.709	C6An.2n
21.083	21.159	C6AAn
21.659	21.688	C6AAr.2n
21.767	21.936	C6Bn.1n
21.992	22.268	C6Bn.2n
22.564	22.758	C6Cn.1n
22.902	23.030	C6Cn.2n

Note: Data from Lourens et al., 2004.

Table T12. Shipboard and shore-based chemical analyses for samples collected during Expedition 322 including sample codes, sample volumes, and investigators. (**See table notes.**)

Sample code:	IWIC	IWICP	322CDIW2	322MTIW1	322VHIW	322JMIW	322MTIW3	322HTIW1	322HTIW2	322CDIW3	322VHIW50	
Type of analysis:	Shipboard Alk, pH, Cl, IC	Shipboard ICP-AES/MS, phosphate	Isotopes O, D, Cl (Destrigneville)	Isotope ^{13}C (Torres)	Volatile fatty acids (Heuer)	Dissolved iron (Moreau)	Sr/REE (Torres)	I conc. (Tomaru)	Isotopes I (Tomaru)	Isotopes Li (Destrigneville)	DOM* (Heuer)	
Volume and container:	4 mL HDPE	4 mL HDPE add 16 mL 6N HCl	2 mL septum screw-lid glass vials	2 mL septum screw-lid glass vials add 100 µL $HgCl_2$	2 mL septum screw-lid glass vials frozen	0.5 mL micro-centrifuge HDPE tubes	8 mL Nalgene HDPE bottle	2 mL HDPE bottle	8 mL HDPE bottle	3 mL HDPE bottle	50 mL septum screw-lid glass vials frozen	Total
>35 mL	4	4	2	2	2	0.5	8	2	8	3		35.5
30 mL	4	4	2	2	2	0.5	8	2		3		27.5
25 mL	4	4	2	2	2*	0.5	8**	2	8**	3*		24.5
20 mL	4	4	2	1*	1*	0.5	4**/7***	2		3**/0***		20
15 mL	4	4	2	1	0.5	0.5	3					15
<10 mL	0.5	2	1	0.5	0.5	0.5						5
Dedicated interstitial water section											50	50

Notes: Samples with asterisks indicate that they were taken in alternate cores depending on interstitial water recovery. Names in parentheses are shore-based investigators. Alk = alkalinity, ICP-AES/MS = inductively coupled plasma–atomic emission spectroscopy/mass spectroscopy, REE = rare earth elements, HDPE = high-density polyethylene, DOM = dissolved organic matter.

Table T13. Expedition 322 interstitial water squeeze cake distribution for archive and shore-based analyses.

Investigator	Sample code	Volume (cm^3)	Type of analyses	Comments
Archive	IWS	40–180		
Conin	322MCIWS	15–60	Water distribution	
Destrigneville	322CDIWS	16–60	Mineralogy, clay mineralogy	
Torres	322MTIWS	17–60	Geochemistry	
Heuer	322VHIWS	18–60	Volatile fatty acids and amino acids	Keep sample frozen
Tomaru	322HTIWS	19–60	Geochemistry	
Scudder	322RSIWS	20–60	Tephra	

Table T14. Measurement performance specifications of the geoVISION tool. (**See table notes.**)

Measurements		Vertical resolution (inch)	Depth of investigation (inch)	Diameter of investigation		Horizontal resolution		Midpoints of extremes
				R_t/R_{xo} = 10	R_t/R_{xo} = 0.1	[(R_t/R_{xo} = 10) * π]/56	[(R_t/R_{xo} = 0.1) * π]/56	
Resistivity at the bit		12–24*	12	32	32			
Ring resistivity		2–3	7	22	25			
Button resistivity	Shallow focused	2–3	1	19	24	1.07	1.35	1.2
	Medium focused	2–3	3	15	21	0.84	1.18	1
	Deep focused	2–3	5	11	16	0.62	0.9	0.75

Notes: * = depends on bit subs. R_t = true resistivity of formation. R_{xo} = resistivity of zone invaded by drilling fluid. Horizontal resolution for each of tools intermediate between extremes of R_t/R_{xo} in table above. Imaging tools record 56 times with each revolution of tool. Accuracy of segment location is ±1°.

Table T15. Measurements and specifications for wireline logging tools. (**See table notes.**)

Tool string	Tool*	Measurement	Sampling interval (cm)	Approximate vertical resolution (cm)	Depth of investigation (cm)
Laterolog	HRLA	Laterolog resistivity	5.1	31	127
	EDTC	Gamma ray		31	61
Radioactive combination	HLDS	Bulk density, PEF, caliper		38	15
	HGNS	Porosity, natural gamma ray	~23	31	61
	HNGS	Spectral gamma ray	15	20–30	24
FMS-sonic combination	EDTC	Gamma ray		31	61
	Sonic Scanner	Sonic	15.24	<182	
	FMS	Microresistivity	0.25	0.5	2.5
VSI	EDTC	Gamma ray		31	61
	VSI	Seismic velocity	Variable	NA	

Notes: * = all tool names are trademarks of Schlumberger. For additional information about tool physics and use, see Chikyu Logging Service Information, at **www.jamstec.go.jp/chikyu/eng/Expedition/logging.html.** HRLA = High-Resolution Laterolog Array, EDTC = Enhanced Digital Telemetry Cartridge, HLDS = Hostile Environment Litho-Density Sonde, HGNS = Highly Integrated Gamma Ray Neutron Sonde, HNGS = Hostile Environment Natural Gamma Ray Sonde, FMS = Formation MicroScanner, VSI = Versatile Seismic Imager. PEF = photoelectric effect. NA = not applicable.

Table T16. Measurements or observations used for core-log-seismic integration. (See table notes.)

Tool:	Core (MSCL)	Core (discrete)	LWD	Wireline	Zero-offset VSP	Surface seismic
Vertical resolution (m):	0.04–0.16	0.5–1	0.05–0.6	0.005–0.38	5–10	10–30
Measurement or observation:	Gamma ray		Gamma ray	Gamma ray		
	Resistivity	Resistivity	Resistivity	Resistivity		
	Density	Density		Density		
		Porosity		Porosity		
				PEF		
	V_P	V_P		V_P, V_S	Check shot, V_P	V_P
	Photo, 2-D/3-D X-ray CT		RAB	FMS		
					Synthetic seismogram	Key reflector

Notes: MSCL = multisensor core logger, LWD = logging while drilling, VSP = vertical seismic profile. CT = computed tomography, RAB = resistivity-at-the-bit, PEF = photoelectric effect, FMS = Formation MicroScanner.